UNIVERSITÀ DEGLI STUDI *DI NAPOLI*
FEDERICO II

DOTTORATO DI RICERCA IN
INGEGNERIA GEOTECNICA
XXVII CICLO

EXPERIMENTAL AND NUMERICAL ASSESSMENT OF DYNAMIC SOIL-PILE-STRUCTURE INTERACTION

Ph.D. Candidate:

Maria Giovanna Durante

Thesis co-advisors:

Prof. Armando Lucio Simonelli
Dipartimento di Ingegneria
Università degli Studi del Sannio, Italy

Prof. Luigi Di Sarno Ph.D.
Dipartimento di Ingegneria
Università degli Studi del Sannio, Italy

Coordinator:

Prof. Claudio Mancuso
Dipartimento di Ingegneria Civile, Edile e Ambientale
Università degli Studi di Napoli Federico II, Italy

Napoli, March 2015

“Dona a chi ami ali per volare, radici per tornare e motivi per rimanere”

Grazie alla mia famiglia per avermelo insegnato.

ABSTRACT

A reliable approach for studying the seismic soil-pile-structure interaction is the physical modelling of scaled models in 1-g or n-g devices. A comprehensive laboratory test campaign, performed on the 6-degree-of-freedom 1-g shaking table of the Bristol Laboratory for Advanced Dynamics Engineering (BLADE) of the University of Bristol (UK), is illustrated and discussed in the present thesis. The experimental campaign was carried out within the framework of the Seismic Engineering Research Infrastructures for European Synergies (SERIES).

The physical model comprises a group of five piles embedded in a bi-layer deposit with several pile-head configurations and equivalent cantilever systems (single-degree of freedom, SDOF). To investigate the seismic soil-pile-structure interaction, the model was subjected to both dynamic and seismic input motions. The physical model was densely instrumented with accelerometers, Linear Variable Displacement Transformers (LVDTs), strain-gauges (along piles) and a contactless displacement transducer (Indikon) for the evaluation of the settlements. Typical results of free-filed, pile and system response analyses are discussed hereafter.

In order to account for the inhomogeneous shear wave velocity profile in the bi-layer deposit, an analytical close-form solution has also been devoleped and validated using the experimental data.

The outcomes of the experimental campaign were used to calibrate an advanced two-dimensions difference element model, which has been implemented in the computer program FLAC2D. The comparisons between the experimental and numerical results are satisfactory for case studies, i.e. considering different input motions (static, dynamic and seismic) and for a wide range of input accelerations.

The research leading to these results has received funding from the European Union Seventh Framework Programme (FP7/2007-2013) under grant agreement n° 227887, SERIES.

The financial support provided by the project ReLUIS (Task MT2) funded by the Italian Civil Protection is also appreciated.

ACKNOWLEDGEMENTS

I would like to thank my tutor Prof. Armando Lucio Simonelli, for giving me the opportunity to approach to the research even before the beginning of my PhD.

A special thank goes also to my co-tutor Prof Luigi Di Sarno, for his constant presence during these years and for his important advices since I was a student.

I want to say thank you to Prof. George Mylonakis and Prof. Colin Taylor for hosting me at the University of Bristol for part of my second year of PhD. Their assistance in the scientific field helped me to improve my knowledge every time that we discussed.

A particular thanks goes also to Dr. Dimitris Karamitros for his assistance and support during my period in Bristol.

Thank you to Prof. Jonathan P Stewart for the fruitful discussions and suggestions about the soil structure interaction basics during his "Italian week".

A special thank you to Dr. Augusto Penna for his kind support during these intense years of work.

Thanks to Prof. Stefania Sica for the useful technical discussions.

Thanks to all the members of the SERIES TA4 project, each one of them contributes to improve the quality of my research.

A very special thanks goes to Maria Grazia, she is a constant presence in my life, a strong woman always smiling!

Finally…Paolo. Of course you are the person who better knows me and my fears and, without saying a word, take my hand and drive me step by step through the hard moments.

LIST OF CONTENTS

LIST OF FIGURES

LIST OF TABLES

LIST OF ABBREVIATIONS

CF: Calibration Factor;

ES: Earthquake Simulator;

ESB: Equivalent Shear Beam;

FFT: Fast Fourier Transform;

FHP: Free Head Pile;

FIM: Foundation Input Motion;

FRF: Frequency Response Function

GUI: Graphical User Interface;

LB: Leighton Buzzard;

LC: Long Cap;

LVDT: Linear Variable Displacement Transducer;

SC: Short Cap;

SDOF: Single Degree of Freedom;

SPSI: Soil Pile Structure Interaction;

SSI: Soil Structure Interaction;

UDM: User Defined Model.

1. INTRODUCTION

Most of the civil engineering structures involve some type of structural element with direct contact with ground. When the external forces, such as earthquakes, act on these systems, the structural and the ground displacements are compliant. The process in which the response of the soil influences the motion of the structure and the motion of the structure influences the response of the soil is termed as soil-structure interaction (SSI). The interaction could be kinematic and/or inertial (Ciampoli and Pinto, 1995; Kramer, 1996; Stewart et al., 1999-a). The inertial interaction is the phenomenon in which inertial forces developed in the structure by its own vibrations generate primarily base shears, bending moments and axial loads, which in turn cause deformations in the soil surrounding the foundation system. These deformations add up to those existing in the free field. Consequently, they modify translational components of ground motions and may lead to rocking and/or torsional excitations. Effects of inertial interaction can be the more important for foundations without large, rigid base slabs and deep embedments. The kinematic interaction results from the propagating nature of seismic disturbances in the form of waves, which makes the soil motion at any given instant generally different from point to point. This interaction is significantly dependent on the ratio between foundation dimensions and strong motion wavelengths. Thus, the presence of stiff foundation elements, either on or embedded, in soil causes vibrations at the structure base, which deviate from free-field motions. This effect becomes relevant only for foundation dimensions, which are of the same order of magnitude as the wavelengths of the ground strong motion. It takes place even if the foundation is virtually massless and may induce different modes of vibration in a structure, such as rocking and torsion.

The kinematic bending moments may be significant especially for piles in soft soils with high stiffness contrasts between consecutive layers. Kinematic and inertial bending moments constitute complementary aspects of the same phenomenon known as Soil-Pile-Structure Interaction (SPSI).

Numerous post-earthquake reconnaissance reports (e.g. Mexico City, Mexico 1985, Kobe; Japan 1995, Kocaeli, Turkey, 1999 Bhuj, India 2001 and Santiago, Chile 2010, earthquakes among many others) showed that a large number of pile-supported buildings in layered soils suffered significant settlements and rotations. Widespread pile damage was observed close to interfaces separating soil layers with significantly different shear moduli.

1.1. SCOPE OF RESEARCH

The scope of the present thesis is to examine the complex soil-pile-structure interaction phenomenon using the results of a comprehensive laboratory tests carried out on 1-g device. Such tests were performed on the 6-degree-of-freedom 1-g shaking table of the Bristol Laboratory for Advanced Dynamics Engineering (BLADE) of the University of Bristol (UK). The experimental tests were carried out within the framework of the Seismic Engineering Research Infrastructures for European Synergies (SERIES - www.series.upatras.gr).

The physical model comprises a group of five piles embedded in a bi-layer deposit of soil with several pile-head configurations and equivalent cantilever systems (single-degree of freedom, SDOF). To investigate the seismic soil-pile-structure interaction, the model was subjected to both dynamic and seismic input motions. The physical model was densely instrumented with accelerometers, Linear Variable Displacement Transformers (LVDTs), strain-gauges (along piles) and a contactless displacement transducer (Indikon) for the evaluation of the settlements. Typical results of free-field, pile and system response analyses are discussed in the thesis. To account for the inhomogeneous shear wave velocity profile in the bi-layer deposit, an analytical close-form solution has also been devoleped and validated using the experimental data.

The outcomes of the experimental campaign were used to calibrate an advanced two-dimensions difference element model, which has been implemented in the difference method code FLAC2D (Itasca, 2005). The comparisons between the experimental and

numerical results are satisfactory for the case studies, i.e. considering different input motions (static, dynamic and seismic) and for a variety of input accelerations.

1.2. LAYOUT OF THE THESIS

The present thesis illustrates the experimental test results and discusses typical results of comprehensive numerical simulations; it consists of six chapters.

Chapter 1 presents the introduction to the thesis, the scope of the work and its framework.

Chapter 2 includes a theoretical background on the seismic pile-structure interaction and the description of the main references used in this work.

Chapter 3 presents all the details of the undertaken experimental campaign. The physical model details, the scaling laws, the principal laboratory devices and the main characteristics of the input motion adopted are described.

Chapter 4 focuses on the analysis of the experimental results. Due to the huge amount of the available data (around 600 tests), only typical results are reported. The chapter includes three sub-sections: free-field, piles and soil-pile-structure responses. In each part typical results referred to the main input motion used in the experimental campaign are illustrated (i.e. white-noise, harmonic and earthquake inputs).

Chapter 5 illustrates the numerical modelling. After a brief introduction to the difference element code used (FLAC Itasca, 2005), the first part of the chapter is voted to the description of all the details regarding the numerical model, that reproduced the physical model tested in the experimental campaign. In the second part the main results of the numerical simulation are compared with typical experimental results, referring to the complete soil-pile-interaction with and without the pile connection among piles.

Chapter 6 summarizes the main outcomes and provides a proposal for further works.

2. THEORETICAL BACKGROUND

Deep foundations are adopted when the shallow soils could not carry the loads transferred by the superstructure. The response of the whole system under both static and seismic condition should always take into account the interaction among the structure, the foundation and the soil. This complex phenomenon of interaction is called soil-pile-structure interaction (SPSI). An extensive historical review of the soil-structure interaction is reported in Kausel (2010). Despite extensive analytical and experimental research over than 30 years, on SSI, there is still controversy regarding its role in the seismic performance of structures (i.e. Jennings and Bielak, 1973; Veletsos and Meek, 1974; Bielak, 1975; Roesset, 1980; Luco, 1982; Wolf, 1985; Gazetas and Mylonakis, 1998; Stewart et al., 1999-a). SSI was traditionally considered beneficial for seismic response; however, it can become detrimental under specific geotechnical and seismological conditions (Mylonakis and Gazetas, 2000).

The main effects of this phenomenon on deep foundation include: *(i)* the variation between the free-field ground motion and the motion at the base of the superstructure, *(ii)* kinematic bending, axial and shear stresses applied along the piles, even in the absence of a superstructure. Examples of kinematic interaction with free-field motions are shown in Figure 2.1 (from Kramer, 1996). Wave amplitudes of the vertical component of free-field motion are restrained and damped because of the flexural rigidity of mat foundation (often considered massless); similarly, for embedded blocks. Shallow foundations can also prevent underlying soil from deforming incoherently through their axial stiffness. The wavelength-to-foundation dimension ratio is of primary importance in kinematic interaction. For wavelengths much longer than the largest dimension of the foundation there is a small or a negligible variation in the ground motion with respect to the free-field. By contrast,

shorter wavelengths or motions varying along the foundation can generate amplitudes or directions of the vibration different from point to point. The reason of such response is twofold. Seismic waves can be out-of-phase while impinging upon different locations of the foundation (incoherence). Additionally, the foundation rests on soil with different physical properties, thus travelling waves are altered in their propagation.

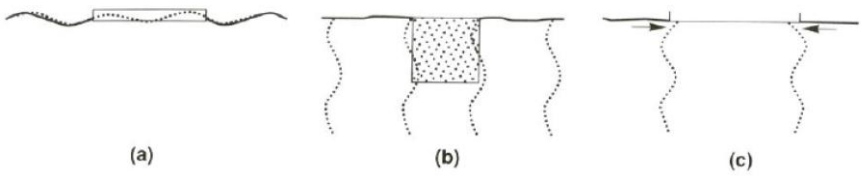

Figure 2.1. Kinematic interaction with free-field motion indicated by dashed line: (a) flexural stiffness of surface foundation prevents it from following vertical component of free-field displacement; (b) rigidity of block foundation prevents it from following horizontal component of free-field displacement; (c) axial stiffness of surface foundation prevents immediately underlying soil from deforming incoherently (from Kramer, 1996)

Rocking modes may be generated in foundation systems subjected to vertically propagating S-waves (Figure 2.2, from Kramer, 1996). At wavelengths equal to the depth of the embedment, unbalanced overturning moments cause the foundation to rock and translate, albeit under purely translational waves. In other cases, different wavelengths and frequencies, rocking can be inhibited. Torsional vibrations of the foundation can also be generated in a similar fashion.

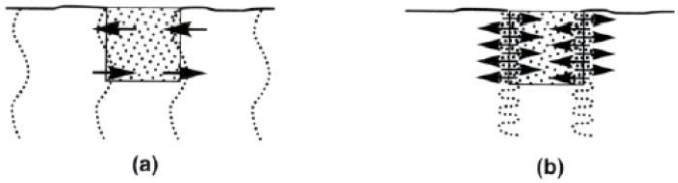

Figure 2.2. Excitation of rocking vibrations in an embedded foundation by vertically propagating s-waves: (a) at certain frequencies, the wavelength is such that unbalanced overturning moments cause rocking; (b) at other frequencies (and wavelengths), rocking may be suppressed (from Kramer, 1996)

Kinematic interaction can be conveniently separated into effects caused by vertical and horizontal extent of foundation systems respectively (Reiter, 1991). The effects of vertical interaction are relevant for embedded foundations with depth of embedment not less than their horizontal extent (Luco, 1985). Several factors influence variations of ground motion with depth; the most important are: *(i)* decrease in amplitude of surface waves with depth; *(ii)* out-of-phase of body waves with wave-fronts not parallel to the side of foundation; *(iii)* rapid variation of seismic properties, e.g. amplitude and velocity

of waves and impedance, in the crust near the Earth surface. Horizontal kinematic interaction should be considered when incoherence and inhomogeneities in the properties of the soil horizontally underlying the foundation are present. Kinematic interaction is often considered a second-order effect for many structures, especially buildings employing foundations of ordinary size (Stewart et al., 1999b); incoherence is however of paramount importance for long span structures, such as bridges, large dams, stadium and lifelines, e.g. highways, railways, gas and electric power, water and waste systems, communication networks. The kinematic bending moments may be significant especially for piles embedded in soft soils with high stiffness contrasts between consecutive layers. On the other hand, inertial interactions can be the more important effects for foundations without large, rigid base slabs and deep embedments. The presence of deformable soil and/or flexible foundation systems affects the seismic response of structures primarily in the following two ways (Figure 2.3): *(i)* increasing the fundamental period of vibration of the structure; *(ii)* increasing the total damping of the structure.

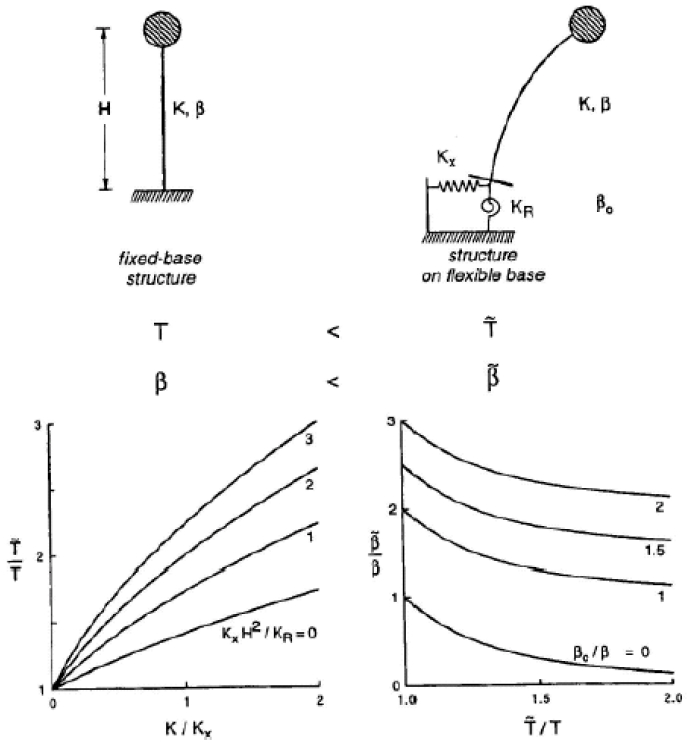

Figure 2.3. Effect of SSI on structural response: period lengthening (left) and increasing in damping (right) (from Mylonakis and Gazetas, 2000)

An extensive literature review is present in several previous studies based on similar (Moccia, 2009) and same experimental campaigns (Chidichimo, 2014).

In the next paragraph the most common literature procedures for the evaluation of kinematic interaction referring to soil layer interface and pile head are reported. The evaluation of the complete soil-structure interaction according to the literature is also shown.

2.1. KINEMATIC INTERACTION

The kinematic interaction is significant at the pile head if rotations are prevented and close by the interface between soil layers with different stiffness.

The available methods present in the literature for the evaluation of the kinematic interaction at soil layer interface can be divided into three groups: *(i)* continuum approaches using numerical analyses based on finite difference method, finite element (i.e. Blaney et al., 1976; Wolf et al., 1981) or boundary element method (i.e. Kaynia and Kausel, 1982; Mamoon e Banerjee, 1990); *(ii)* simplified methods with Winkler-like approach (i.e. Fan et al., 1991; Kavvadas and Gazetas, 1993); *(iii)* analytical closed form solutions (i.e. Dobry and O'Rourke, 1983; Nikolaou and Gazetas, 1997; Nikolaou et al., 2001; Mylonakis, 2001). The continuum approach allows to satisfactory taking into account the soil response, even if it is not easy to account for the non-linearity. The Winkler-like approach accounts for the soil response by means of springs and dashpots along the pile. The soil non-linearity can be considered using *p-y* curves. The closed form solutions are obtained starting from Winkler model results (Dobry and O'Rourke, 1983; Nikolaou et al., 2001) or from the mechanical response of the pile embedded in a by-layer deposit (Mylonakis, 2001). The simplified solution given by Mylonakis (2001) allows to account for the dynamic effect in the pile response. Cairo and Dente (2007) propose a method to perform the kinematic interaction analysis based on the stiffness method (Samuelsson and Zienkiewicz, 2006), using the discrete dynamic stiffness matrices derived by Foinquinos and Roësset (2000) to simulate the response of layered soils. This approach is an extension of a precedent work (Cairo et al., 2005) to analyse single piles and pile groups subjected to vertical harmonic loadings. Recently, other closed form solutions for the kinematic bending moments were published (i.e. Maiorano et al., 2009; Sica et al., 2011; Di Laora et al., 2012).

Closed-form solutions for the pile head responses have also been studied (Margason and Holloway, 1977; Flores-Barrones and Whitman, 1982; Miniero, 1990; Mylonakis, 1995; Nikolau et al., 2001). As highlighted by Mylonakis and Nikolau (2002), these

solutions are obtained accounting for homogeneous soil conditions and the kinematic effects are overestimated for deposit formed by alternating soft and stiff layers. More recent solutions (i.e. Dezi et al., 2009; de Sanctis et al., 2010; Di Laora et al., 2013) consider the effect of subsoil condition on the kinematic bending moments at pile head using the concept of the influence line, that is independent to the pile length, when it is larger than the active value. Using numerical analyses de Sanctis et al. (2010) demonstrated that the accuracy of the simplified solution is satisfactory if the maximum bending moment at pile head is considered as a linear function of the maximum acceleration at the soil surface in free-field condition.

2.2. SOIL-STRUCTURE INTERACTION

A summary of the SSI principles and guidance is reported in NIST (National Institute of Standard and Technology, 2012). The complete soil-structure interaction can be modelled using two different approaches: *(i)* a continuum-based model or *(ii)* a substructure-based approach.

Figure 2.4 shows a schematic illustration of the main features that should be taken into account for soil-structure interaction analysis using a continuum approach (also called direct method). In this method, the non-linear behaviour of each part of the model can be simulated, by using appropriate constitutive models.

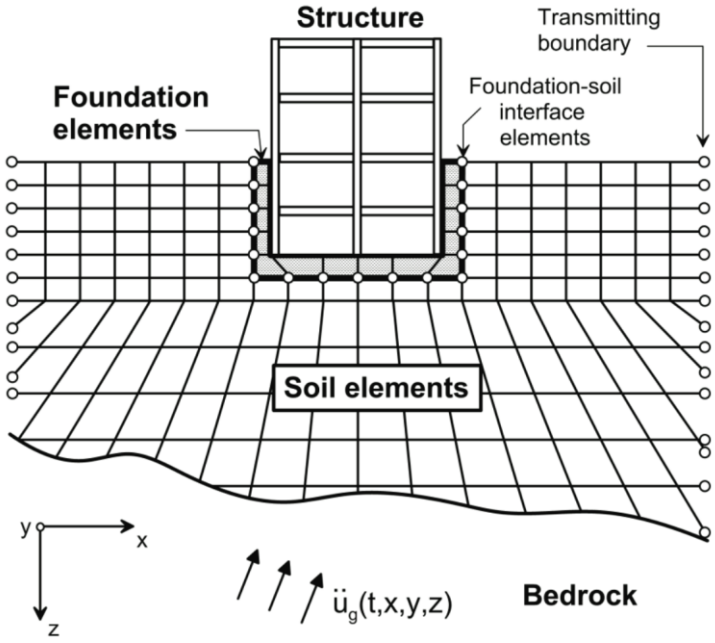

Figure 2.4. Schematic illustration of a direct analysis of soil-structure interaction using continuum modelling by finite elements (from NIST, 2012)

Figure 2.5 shows the substructure approach (also called indirect method). The idea of this method is to summarize the soil response with springs and dashpots that are calibrated to represent the continuum response. According to this approach, the input imposed to the structure (Foundation Input Motion – FIM) is adjusted from the free-field response accounting for effects due to the presence of the foundation.

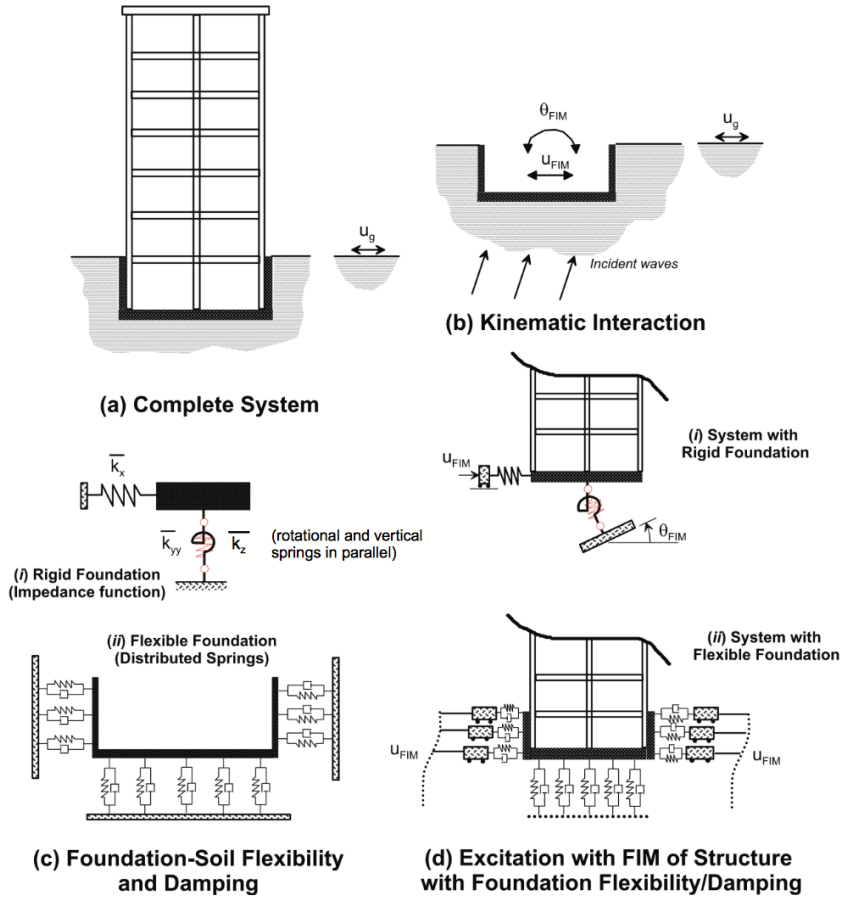

Figure 2.5. Schematic illustration of a substructure approach to analysis of soil-structure interaction using either: (i) rigid foundation; or (ii) flexible foundation assumptions (from NIST, 2012)

SSI can be studied by using analytical, numerical, experimental methods (scaled model or prototype) separately, and/or, by combining these methods in different manner. The reliability of the results is related to the assumptions or restrictions of the used approaches (i.e. Luco, 1973; Chopra and Gutierrez, 1974; Seed, 1975; Lysmer et al., 1975; Bielak, 1976; Solari et al., 1980; Mizuno, 1980; Wolf 1985; Beskos, 1993; Stewart and Fenves, 1998; Stewart et al., 1999a-b; Ghalibafian, 2006; Pitilakis et al., 2007; Kwon et al., 2013; Hokmabadi et al., 2014; Durante et al., 2015a).

3 EXPERIMENTAL 1-G MODELLING

Ad-hoc laboratory investigations are essential for studying complex soil-structure interaction, due the paucity of the field (or full scale model) data, which tend to be expensive to conduct and hard to interpret. Data from instrumented piles under buildings of different vibrational characteristics subjected to actual earthquake motions would be ideal. These data are rare due to high cost and the unpredictable nature of earthquake occurrence. Therefore, well-controlled laboratory investigation on model piles along with analytical and/or numerical simulations is pivotal for understanding the seismic response of both single piles and pile groups (see, for example, Muir Wood et al., 2002). Centrifuge and 1-g shaking table tests are typically adopted for this scope (e.g. Mizuno et al., 1984; Meymand, 1998; Wei et al., 2001; Chau et al., 2009; Tokimatsu and Suzuki, 2009; Moccia, 2009; Chidichimo, 2014, among others).

The approaches based on the use of the 1-g shaking table possess certain advantages over centrifuge procedures, such as the valuable benefit of working on a larger and more reliable physical models, which allow detailed measurements of pile response and numerous combinations regarding soil profile, pile-head boundary conditions, superstructure features. Additionally, it is possible to plan and carry out a wide set of tests with reasonable operating expenses.

In this chapter the experimental program performed at the Bristol University Laboratory for Advanced Dynamics Engineering (BLADE), within the Framework of the Seismic Engineering Research Infrastructures for European Synergies (SERIES) is described. This research programme is an extension of the work on Soil-Structure Interaction (SSI) carried out in a previous research programme (RELUIS, 2005-2008). Tests were carried out on a group of five piles embedded in a bi-layer deposit with different pile group configurations (with and without pile caps) and different superstructures, subjected to different input motions (i.e. white noise, sinedwells and

scaled earthquake ground motions). The dynamic response of the model was explored by means of an extensive 1-g shaking table campaign comprising two series of tests: *(i)* preliminary tests and *(ii)* a more comprehensive series of tests (i.e. Simonelli et al., 2012a,b; Durante et al., 2012; Durante et al., 2013a,b; Durante et al., 2014a,b; Simonelli et al., 2014; Chidichimo, 2014; Chidichimo et al., 2014; Durante et al., 2015a,b). More details about the experimental models are provided in the remainder of this chapter.

3.1 SCALING LAWS

The first step in an experimental study for both shaking table and centrifuge tests is the derivation of the scaling laws. The similitude relationships are essential for scaling up the experimental results to real prototypes. These relationships are described by a theory of scale model similitude: there are two procedures to scale up model results (Figure 3.1):

- The first approach is to use standard tables (look-up approach) for scaling the model observations by pertinent factors to predict the prototype response;
- The second approach is to study the underlying mechanics/physics of the problem based on the model tests recognizing that not all the interaction mechanisms can be scaled accurately in a given test. Once the mechanics/physics of the problem are identified in term of pertinent dimensionless ratios, the prototype response can be predicted through analytical and/or numerical modelling in which the physics/mechanics discovered are implemented in a suitable way (problem-specific scaling relationships).

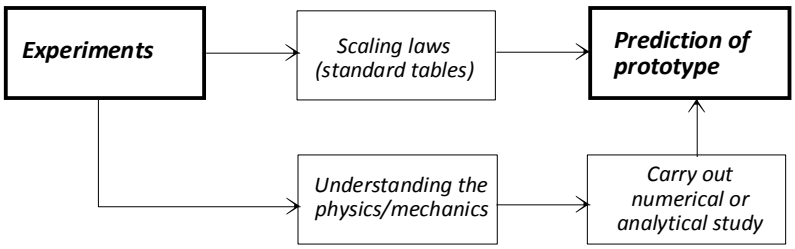

Figure 3.1. Main procedure for scale up model results (from Simonelli et al., 2014)

The second method, which has been adopted in the present study, is useful when none of the physical modelling techniques can simultaneously satisfy all the interactions to the appropriate scale, such as for studying a complex dynamic foundation-structure interaction configuration.

All physical phenomena can be expressed in term of dimensionless groups taking into account the physical mechanisms and parameters important for the analyzed problem. In this study the most important aspects are: *(i)* stiffness ratio between the two soil layers, *(ii)* characteristics of the Single-Degree-of-Freedom (SDOF) structure supported by the pile, *(iii)* frequency and intensity scaling of the earthquake record, *(iv)* pile-soil stiffness contrast; *(v)* ratio of strains and accelerations in the soil and the pile.

Muir Wood et al. (2002) scaling laws were adopted in the present study a number of scaling factors for single gravity soil models from four fundamental scaling factors (length, density, stiffness and acceleration) were derived. The scale factors utilized are shown in Table 3.1.

Table 3.1. Scale factors for single gravity models (from Muir Wood et al., 2002)

Variable	Scale Factor	1-g model	n-g model
Length	$Length_{model}/Lenght_{prototype} = n_l$	1/n	1/n
Density	n_ρ	1	1
Stiffness	n_G	$1/\sqrt{n}$	1
Acceleration	n_g	1	n
Stress	$n_\rho\, n_g\, n_l$	1/n	1
Strain	$n_\rho\, n_g\, n_l/n_G$	$1/\sqrt{n}$	1
Displacement	$n_\rho\, n_g\, n_l^2/n_G$	$1/n^{1.5}$	1/n
Velocity	$n_g\, n_l\, \sqrt{(n_\rho/n_G)}$	$1/n^{0.75}$	1
Dynamic time	$n_l\, \sqrt{(n_\rho/n_G)}$	$1/n^{0.75}$	1/n
Frequency	$\sqrt{(\, n_G\, /n_\rho)}/\, n_l$	$n^{0.75}$	n
Shear wave velocity	$\sqrt{(\, n_G\, /n_\rho)}$	$1/n^{0.25}$	1
Pile flexural rigidity	$n_G\, n_l^4$	$1/n^{4.5}$	$1/n^4$
Pile linear density	$n_\rho\, n_l^2$	$1/n^2$	$1/n^2$

The experimental campaign described hereafter refers to a research programme which is an extension of a previous study on SSI (ReLuis, 2005-2008); the prototype system is thus the same (Figure 3.2).

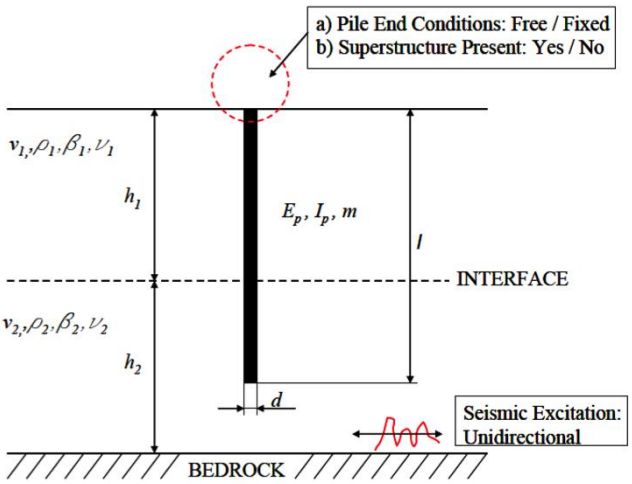

Figure 3.2. Reference numerical prototype (from ReLuis Report, 2008)

The above reference prototype has been employed in previous parametric studies (e.g. Mylonakis et al., 1997; Nikolaou et al., 2001; Sica et al., 2007; Maiorano et al., 2008). The prototype pile is a concrete pile of Young's modulus E_p=25 GPa, diameter d=600 mm and length l=20 m. The pile is embedded in a two-layer soil deposit. Each soil layer is characterized by its thickness h, density ρ, shear wave velocity V_s, Poisson's ratio ν, and damping ratio β. The prototype shear wave velocities are V_{s1}=100 m/s and V_{s2}=400 m/s. The Poisson's ratio and the thickness of the soil were considered the same for the two layers (ν_1= ν_2=0.4 and h_1=h_2=15 m respectively).

In this study, the ratio between the prototype soil depth (30 m) and the height of the test container (0.8 m), gives the fundamental scale factor for length (n=37.5). At model scale shear, wave velocities correspond to V_{s1}=40 m/s and V_{s2}=160 m/s. These shear wave velocities lead to a model stiffness ratio G_{bottom}/ G_{top} of 16, where G_{bottom} and G_{top} are the shear moduli of the bottom and top layer, respectively. Designing and building granular layered deposits of a given stiffness ratio is not a trivial task. The above values for the stiffness ratio of the bottom and top layers were used as indicative during the design stage.

3.2 MODELLING

The theoretical model employed in piles modelling is an Euler-Bernoulli beam in pure bending (Figure 3.3). It is assumed that the pile is not being so heavily loaded that it is stressed by axial load or in bending beyond its elastic range. The maximum lateral load capacity of the pile moving relative to soil is not exceeded (Muir Wood, 2004).

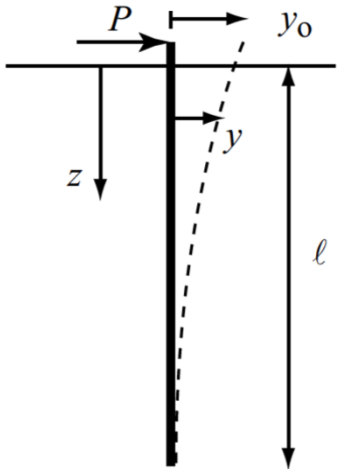

Figure 3.3. Pile under lateral loading (from Muir Wood, 2004)

The pile can be hence considered as a beam subjected to loading at the ground surface or at the head of the pile and by the resistance of the ground to relative movement of pile and soil. If the soil responds elastically, then the resisting force is proportional to relative displacements according to some coefficient of subgrade reaction k and the equation governing the deformation of the pile will be of the form:

$$EI\frac{d^4y}{dz^4}=-ky \tag{3.1}$$

where *EI* is the pile flexural rigidity, *y* is the horizontal deflection of the pile, *z* is the pile coordinate along depth and *k* is the coefficient proportional to soil shear modulus G (k=βG).

Equation 3.1 can be normalised by defining a dimensionless depth (ζ) and a dimensionless pile deflection (λ):

$$\zeta=\frac{z}{l} \quad ; \quad \lambda=\frac{y}{y_0} \tag{3.2 a, b}$$

where l is the length of the pile and y_0 is the lateral deflection of the pile at its top.

Equation 3.1 becomes:

$$\frac{EI}{l^4}\frac{d^4\lambda}{d\zeta^4}=-k\lambda \tag{3.3}$$

considering k=βG, a dimensionless group (Φ_1), which describes relative pile-soil stiffness can be defined as follows:

$$\Phi_1=\frac{Gl^4}{EI} \tag{3.4}$$

Since the pile length has no practical significance beyond 10 to 15 times the pile diameter (the so-called 'active length', Randolph, 1981), the dimensionless group to be used in modelling is adequately described by:

$$\Phi_2=\frac{Gd^4}{EI} \tag{3.5}$$

where *d* is the pile diameter.

The correct physical modelling requires the same dimensionless ratio Φ_2 for both model and the prototype: by adopting an aluminium alloy model pile (Young modulus E_{AL}=70 GPa, outer diameter D_e=20mm, length l=0.75m) and applying the equivalence law in Equation 3.5, the thickness (t) of the model pile is calculated (t=0.146mm). The smallest thickness aluminium tube that is commercially available is 6063-T6 HE9TF aluminium alloy tube of thickness t=0.71mm and outer diameter D_e=2.23mm, so this tube was adopted for the model piles.

3.3 EXPERIMENTAL SET-UP

The 6-degree-of-freedom earthquake simulator of BLADE and the equivalent shear beam (ESB) container was utilized to perform the aforementioned series of tests. More details on the devices used are given in the following paragraphs.

i) Experimental procedure

The testing procedure includes the following dynamic input motions:

- *White noise excitation*: during white noise exploratory testing, a random noise signal of bandwidth 0-100Hz and peak ground acceleration varying between 0.01g and 0.10g was employed. In total 45 horizontal (first phase), 28 horizontal and two vertical (second phase) white noise tests were performed;
- *Harmonic excitation*: sinedwell acceleration time-histories were imposed. In the first stage of testing 291 different sinedwells were used. Each one is formed by 12 steady-state cycles; 15 different frequencies of excitation (varying from 5Hz to 30Hz with a step of 2.5Hz and from 30Hz to 50Hz with a step of 5Hz) and acceleration amplitudes varying between 0.01g÷0.18g were applied. In the second stage 142 horizontal and 26 vertical sinusoidal excitations were employed, characterized by 16 steady cycles; 7 frequencies (varying from 5Hz to 45Hz with a step of 5Hz) were employed with acceleration amplitudes varying between 0.01g÷0.13g.
- *Earthquake excitation*: three earthquake records from the SISMA database (Scasserra et al., 2008) were selected for seismic testing: Tolmezzo from the Friuli 1976 earthquake, Sturno from the Irpinia 1980 earthquake and Nocera Umbra Biscontini from the Umbria-Marche 1997 event. The earthquake motions were modified by a frequency-scaling factor of 5 or 12 to account for different size between model and prototype. The frequency-scaled signals were applied at

acceleration amplitude varying from 0.043g to 0.577g. 19 earthquake input motions were used in total. More details about earthquake excitation are provided in the next paragraph.

The experimental program included also two pseudo-static tests:

- Pullover test: small increments of lateral load were applied, while monitoring the pile head response by means of displacement transducers;
- Snapback test: after the application of traction on the pile head through a pulley system (several weight on the pulley were applied) the wire was cut and the horizontal motion of piles was measured for the estimation of the natural frequency and damping ratio of the embedded pile. One of the five snapback test was performed at the end of the pullover test.

ii) Earthquake Simulator (shaking table)

The 6 degree-of-freedom Earthquake Simulator (ES) (Figure 3.4) consists of a 3m x 3m cast aluminium platform weighing 3.8 tonnes and capable of carrying a maximum payload of 15 tonnes. The platform has the shape of an inverted pyramid made by four sections and has a honeycomb-like network of stiffening diaphragms giving it high strength and bending stiffness. The platform surface is an arrangement of five aluminium plates with a regular grid of M12 bolt holes for attaching to the platform body and for mounting the specimens. The platform sits inside a reinforced concrete seismic block that has a mass of 300 tonnes. The block is located in a pit in the Earthquake Engineering Laboratory and is isolated from the rest of the laboratory by a 20 mm cork filled gap running between the block and the rest of the laboratory. Hydraulic power for the ES is provided by a set of 6 shared variable volume hydraulic pumps providing up to 900 litres/min at a working pressure of 205 bar. The maximum flow capacity can be increased to around 1200 litres/min for up to 16 seconds at times of peak demand with the addition of extra hydraulic accumulators. The platform is attached to the block by eight hydraulic actuators arranged in order to optimise the space available. The horizontal actuators are attached to the block by concrete filled steel box sections and to the platform by smaller closed triangular brackets. The vertical actuators are connected directly to the block and platform. Each actuator has a dynamic capacity of 70 kN and has a maximum stroke of 300 mm. Each of the four vertical actuators has a static section capable to carry the static loads of the platform plus specimen.

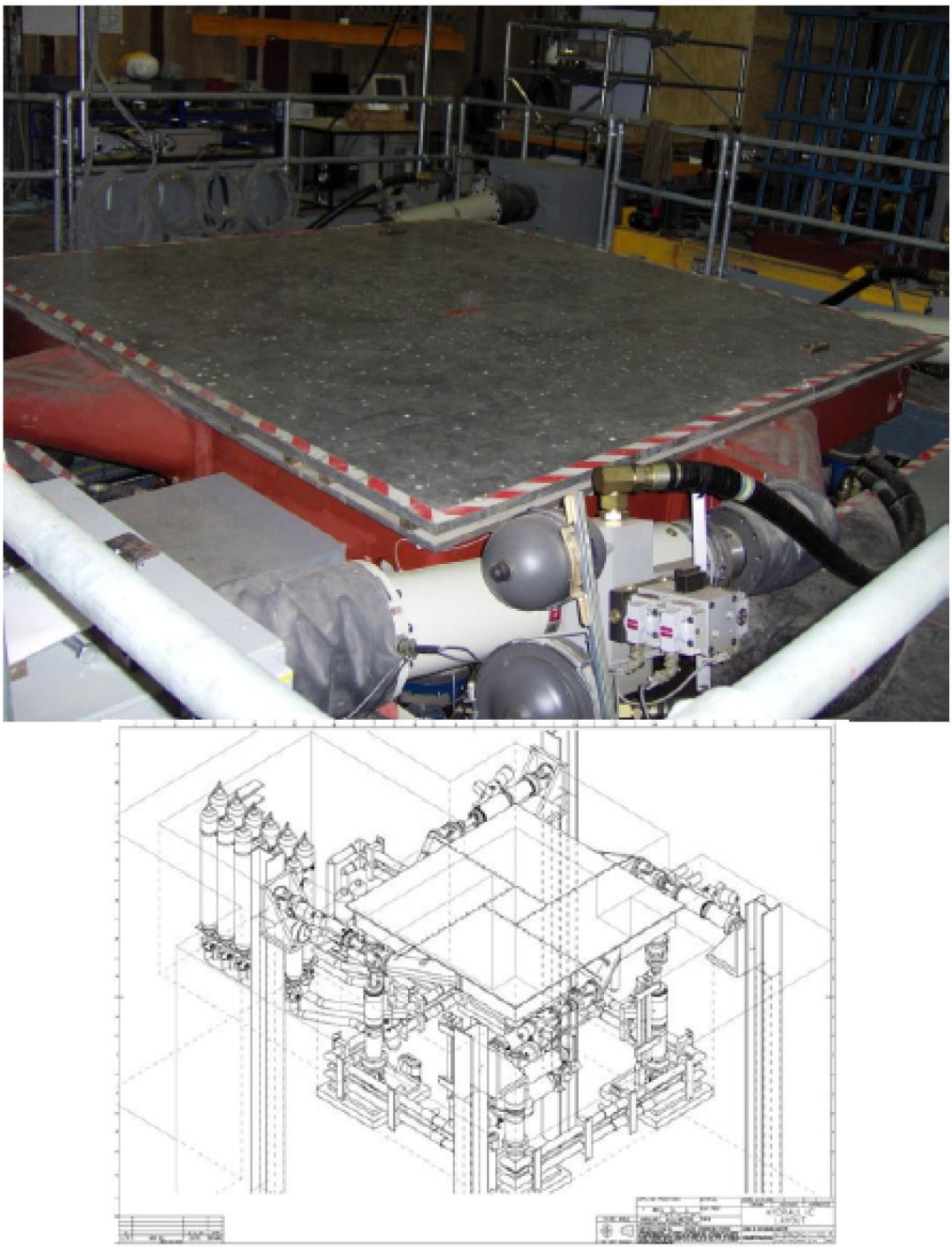

Figure 3.4. Earthquake simulator at Bristol University (from Moccia, 2009)

iii) Equivalent Soil Container

The equivalent soil container ensures that it follows the soil movements without influencing its response. Several different soil containers were proposed to minimize boundary effects; the most common are: (1) the Laminar box (Kutter, 1995; Hushmand et al., 1988; Ueng et al., 2006; Brennan et al., 2006), shown in Figure 3.5 and (2) the Equivalent Shear Beam box (Figure 3.6).

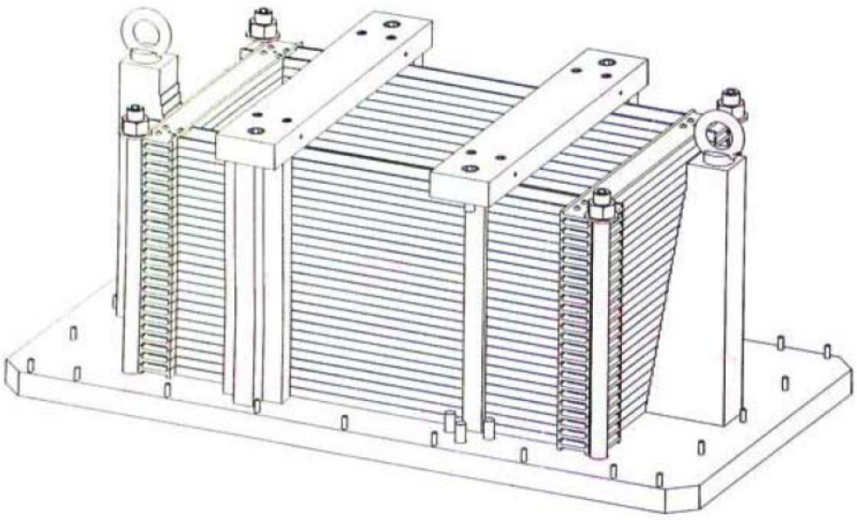

Figure 3.5. Laminar box - 3D view (from Knappet, 2006)

Laminar box soil containers are constructed from a stack of stiff rings, which may experience independent and unrestrained lateral displacements because of the box negligible shear stiffness. Internal walls of the rings are made smooth to restrict boundary shear stresses. Laminar box is often used to model liquefaction.

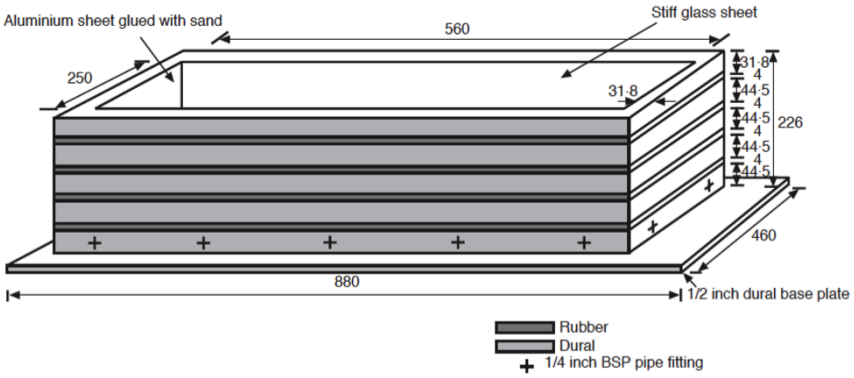

Figure 3.6. Equivalent Shear Beam - 3D view (Zeng and Schofield, 1996)

When liquefaction is not of interest, boundaries must be both frictional and flexible. Zeng and Schofield's (1996) Equivalent Shear Beam (ESB) centrifuge container, has roughened internal walls to enable shear stress transmission. It was constructed from an alternating stack of aluminium alloy and rubber rings for flexibility. The composite shear stiffness of the ESB was tuned to the dynamic stiffness of a test soil by careful detailing of the rubber layer thickness. This type of containers should be ideally designed to match the shear stiffness of the inner soil. However, the shear stiffness of the soil varies during shaking depending on strain level. Therefore, the matching between the end wall and the soil stiffness would be possible only at a particular strain level. The ESB of BLADE Laboratory is designed considering a value of strain in the soil close to failure conditions. It is thus more flexible than the soil deposit at lower

strain amplitudes and, consequently, the soil will always dictate the overall behaviour of the container (Bhattacharya et al., 2011). The resonant frequency and damping of the empty container in the first shear mode in the longitudinal direction were measured prior to testing as 5.7 Hz and 27%, respectively; such values are sufficiently different from the soil material properties. The Bristol University ESB was designed by Crewe et al. (1995) (Figure 3.7) and it is a direct descendant of the 'large flexible shear stack'. It is closer in size to Dar's 1993 original: 1.2m long as opposed to 5m, 0.55m wide as opposed to 1m, and 0.814m deep as opposed to 1.2m, significantly reducing the costs and time scales associated with testing.

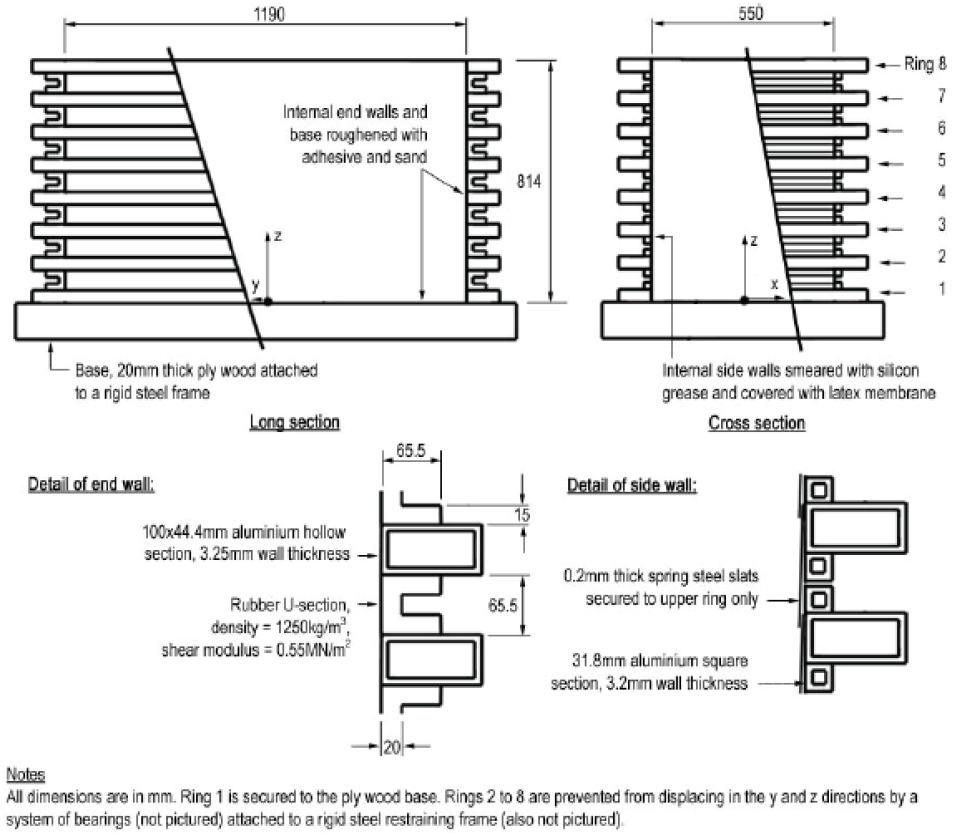

Figure 3.7. Shear stack details (from Crewe et al., 1995)

The ESB (Figure 3.8) consists of eight aluminium alloy rings separated by rubber U-sections across the end walls and a system of slats on the side walls. The rings are made of aluminium box section to minimize inertia while providing sufficient constraint for the K_0 condition. An outside steel frame built of steel L-sections restrains the stack movements in the horizontal and vertical directions. The frame contains four columns, four beams joining the top of the columns and four braces restricting any sway. Each column has seven roller bearings oriented in the Y direction, each one bearing on a separate ring (2 to 8). Thus, the unwanted vibrations of the stack on Y direction are prevented. There are roller bearings attached to the outside frame on each corner of

Ring 8 (bottom ring), which restrict the unwanted vibrations on Z direction. The stack will be attached to the shaking table and shaken in its longitudinal (Y) direction. In order to generate complementary shear stresses between the stack end walls and the soil, the inside surface of the end walls is roughened. The rigid base of the stack will be roughened with coarse sand to prevent sliding of the sand mass. The inside surface of the longitudinal walls of the stack will be covered with silicone grease and a latex membrane. The membrane will allow the soil to move freely in the longitudinal direction, which is the direction of shearing (2-D plane strain conditions).

Figure 3.8. Shear stack

iv) Digital Spectrum Analyser

A digital spectrum analyzer (Advantest 9211C) will be employed in the dynamic measurements (shape modes, natural frequency of vibration, damping). The analyzer computes the frequency response function (FRF) between the input and the output signals of interest. The FRF is applied to the product between the signal data and a window function (rectangular). The rectangular window function is zero-valued outside a chosen frequency interval. The rectangular window function has been proved to work well in the low dynamic range, when the signals have comparable strengths and frequencies. The FRF measurements will be processed using curve-fitting algorithms that take the experimentally measured FRFs and fit them to an analytical function using a least squared error technique. The poles of the transfer function will be used to compute the viscous damping for various modes of vibration.

A typical response of this procedure is reported in Figure 3.9.

			Excitation	Response
Project Reference:	TA4_110			
Date:	13/06/11	**Channel Number:**	1	14
Time:	11:59	**Instrument Type:**	Setra	Setra
Test Reference:	TA4_1106_FHP_X1R1	**Instrument ID:**	1402	1401
Numer of Averages:	16	**Location:**	Table	Surface
Window Type:	Hanning	**Direction:**	y	z
Frequency Range:	0–100 Hz			

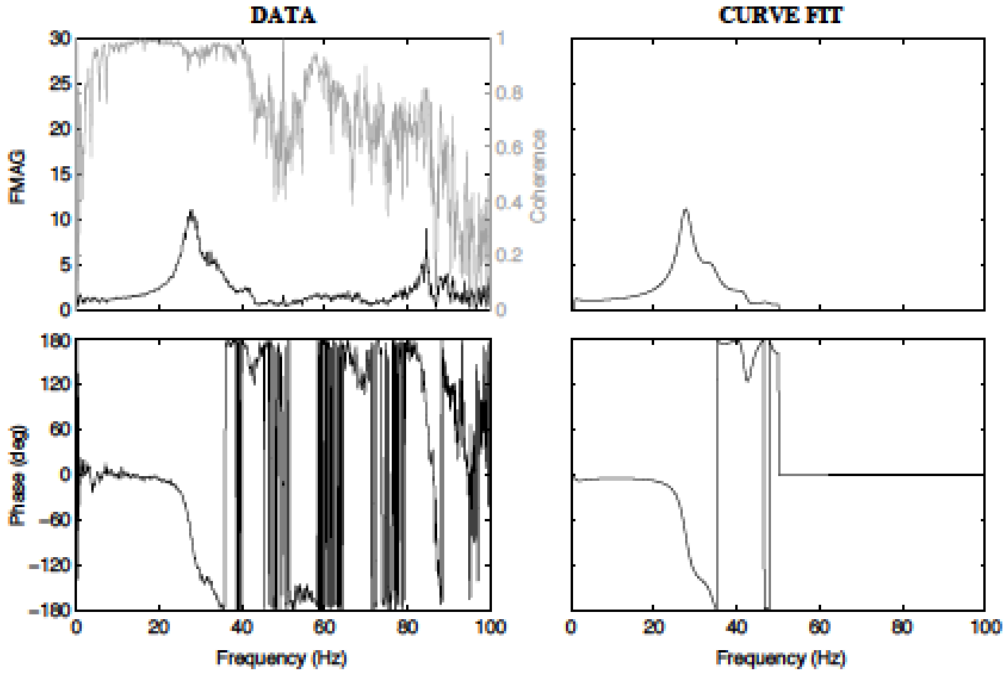

EXPLORATORY TEST SUMMARY

Frequency (Hz)	Amplitude	Phase	Coherence	Real	Imaginary	Damping (%)
27.63	11.11	−78.90	0.94	1.61	27.63	5.82
34.12	4.90	−165.16	0.98	1.84	34.12	5.39
41.91	1.73	141.64	0.94	0.95	41.91	2.26
47.26	0.78	−177.30	0.65	1.67	47.26	3.53

Figure 3.9. Typical Digital Spectrum Analyser response

v) Accelerometers

18 accelerometers type SETRA 141A (Figure 3.10) were installed for the direct evaluation of the response of the soil, the shear stack and piles. The accelerometers are of the high output capacitance type with inbuilt pre-amplifiers which operate over a frequency range of 0 to 3000Hz (Calibrated range: +/-8g). The SETRA accelerometer signals were amplified by a set of Fylde 245GA mini-amplifiers. These have multiple gain, variable sensitivity and offset options. The amplified signals will be supplied to a FERN EF6 multi-channel programmable filter that will be set at a common cut-off frequency on all channels (80 Hz) (Dietz et al., 2007). Data obtained in this way, through appropriate calibration factors, give direct measurements of the values of interest. Figure 3.10 shows also the typical device used for the accelerometer calibration.

Figure 3.10. SETRA accelerometer (left) and its calibration device (right)

vi) Linear Variable Displacement Transformer (LVDT)

Eight Linear Variable Displacement Transformers (LVDT, type RDP DCTH) (Figure 3.11) were installed for the evaluation of the horizontal and vertical displacement of piles, and horizontal displacement of the shear stack. The excitation voltage for the displacement transducers was supply by an RDP 600-type modular electronics system. The signal conditioning of the LVDTs will be made via the RDP 611 amplifier modules. These amplifiers allow optimisation of both the excitation voltage and gain and can impart DC offsets in order to zero signals.

Figure 3.11. Linear Variable Displacement Transformer (LVDT)

In the typical calibration procedure the displacement is imposed using the calibration device (Figure 3.12) and plotted versus the corresponding Volts read by the LVDT. The linear proportionality between the magnitude and the displacement, after several steps the calibration factor (CF) is the *x* coefficient of the interpolation equation.

Figure 3.12. Typical LVDT calibration device

vii) Strain-gauges

36 linear strain gauges pattern of 3 mm length (type EA-13-120LZ-120) (Figure 3.13) were used for the evaluation of the bending moments and the axial force on the instrumented piles. The excitation voltage for strain gauges was the same of the LVDT; the completion of the bridge and the excitation voltage for the strain gauges were made via RDP 628 strain gauge amplifier modules.

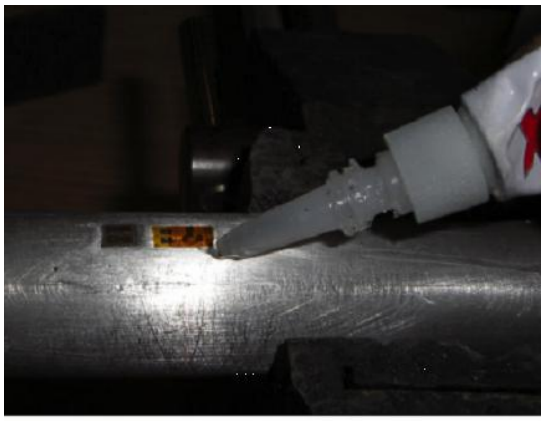

Figure 3.13. Strain-gauges glued to the pile

Strain gauges values were located on opposite pile side (Figure 3.14) at different height to obtain bending moments and axial force along piles. The deformations are generated by both bending moment (ε_{BM}) and axial force (ε_{AF}), and are given as:

$$\begin{cases} \varepsilon_1 = \varepsilon_{AF} + \varepsilon_{BM} \\ \varepsilon_2 = \varepsilon_{AF} - \varepsilon_{BM} \end{cases} \tag{3.6}$$

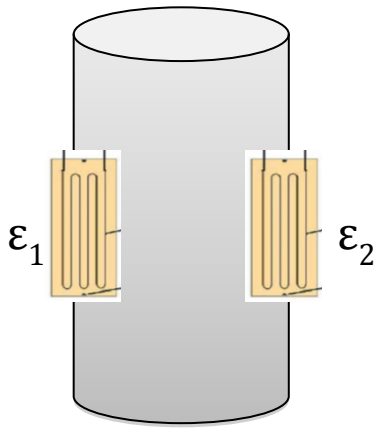

Figure 3.14. Schematic representation of strain- gauges location

In the hypotheses of the conservation of the plane section and of elasticity of the pile, it is possible to obtain the equations for the evaluation of bending moment (Equation 3.7) and axial force (Equation 3.8) (Figure 3.15):

$$M = \frac{\varepsilon_1 - \varepsilon_2}{2} E_p I_p \left(\frac{2}{D}\right) \tag{3.7}$$

$$N = \frac{\varepsilon_1 + \varepsilon_2}{2} E_p A_p \tag{3.8}$$

where E_p, I_p, D are the Young's modulus, the moment of inertia and the diameter of the pile respectively and A_p is the area of the pile cross-section.

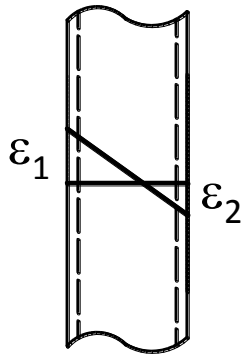

Figure 3.15. Typical strain responses along pile

viii) Indikon

An Indikon device (Figure 3.16) with a 0-30 mm range is used for the monitoring of the settlement of the model. The Indikon is a non-contact displacement transducer based on eddy effect.

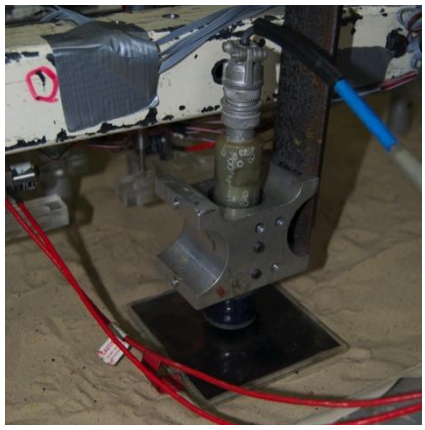

Figure 3.16. Indikon device

3.4 PHYSICAL MODEL CHARACTERISTICS

In the next paragraphs the details of the physical model, schematically reproduced in Figure 3.17, are given. The geometrical and mechanical characteristics of each component are reported. The experimental campaign was performed in two different phases (first and second phase).

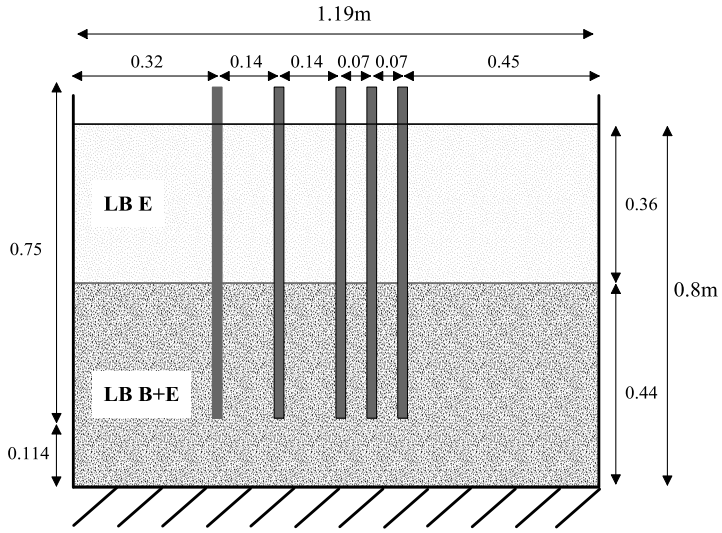

Figure 3.17. Physical model

3.4.1 Soil model geometry and properties

The soil configuration is the same in both phases. A two layers soil deposit was realized by pluviation (Figure 3.18). The top layer is made of 340mm of Leighton Buzzard sand (LB) fraction E, deposited through a 40mm diameter nozzle; a mass density of 1390 and 1339 kg/m^3 were obtained in the first and second phase respectively. The bottom layer (460mm) is a mix between LB fractions B and E (85% and 15%, respectively) pluviated through a 12mm diameter nozzle; a mass density of

1780 and 1827 kg/m^3 were obtained in the first and second phases respectively. The free surface of the soil deposit is 800mm above the base of the shear stack.

Figure 3.18. Pluviation for the bottom (left) and top layer (right)

The LB sand has been extensively used in the experimental research carried out in previous experimental studies (Seed and Idriss, 1970; Stroud, 1971; Tan 1990; Cavallaro et al., 2001; Lings and Dietz, 2004; Moccia, 2009; Visone and Santucci de Magistris 2009; Bui 2009; Cai, 2010). The characteristics of the LB sand are reported in Table 3.2.

Table 3.2. Leighton Buzzard sand properties

Materials	γ_s [kg/m^3	e_{min}	e_{max}	D_{10}	D_{50}	References
LB fraction E	2647	0.613	1.014	0.095	0.14	Tan (1990)
LB fraction B	2647	0.486	0.78		0.82	Ling and Dietz (2004)
LB fraction E+B	2647	0.289	0.614			Moccia (2009)

The soil layer properties obtained in the experimental tests are reported in Table 3.3. The shear wave velocity (V_s) reported is the equivalent homogeneous velocity. The V_s was derived from the white noise tests carried out before sinedwell and earthquake tests, for each stage of the experimental activity. The shear wave velocity contrasts between the bottom (V_{s2}) and top layer (V_{s1}) are quite close, around 1.6, for the two stages of tests.

Table 3.3. Soil layers properties

Soil layers	Thickness H [mm]	Void ratio e	Relative density Dr [%]	Dry unit weight γ_d [kN/m^3]	Shear wave velocity Vs [m/s]		Vs_2/Vs_1	
					Phase I	Phase II	Phase I	Phase II
Top LB(E)	340	0.9	28	13.63	51	54	1.59	1.57
Bottom LB(E+B)	460	0.48	41	17.46	81	85		

3.4.2 Structural elements configurations and properties

The structure components of the model consist of piles, a cantilever system (a single degree-of-freedom, SDOF) provided with its foundation and two kinds of connection, namely one between a small group of piles (so called short-cap connection) and the other connecting all the five piles (so called large-cap connection).

In both experimental phases, the five piles embedded in the bi-layer soil (Figure 3.17) consist of an alloy aluminium tube (commercial model 6063-T6) with thickness t = 0.71mm, outer diameter D = 22.23mm and length l = 750mm. Pile 3, 4 and 5 are closer to each other with a relative spacing s=70mm (s/D ≈ 3); pile 1 and 2 are placed at a distance of 140mm. The properties of the aluminium tubes are summarised in Table 3.4.

Table 3.4. Pile properties

Geometrical details [mm]	Unit weight [kN/m^3]	Length [mm]	Young's modulus [GPa]	Poisson's ratio
De = 22.23 t = 0.71	27	750	70	0.3

In the first stage of the tests the oscillator was formed by an aluminium column with extra masses added to its top to achieve different dynamic response. In the second phase, three different columns were used (two in aluminium and one in steel) to vary the pier stiffness.

The details of the columns are reported in Table 3.5. Details of the fixed base oscillator are reported in Table 3.6.

Table 3.5. Columns properties

Column material	Cross section [mm x mm]	Unit weight [kN/m^3]	Length [mm]	Young's modulus E [GPa]
Aluminium	3x12	27	100 (phase I) 50 -100 (phase II)	70
Steel	3x12	80	100 (phase II)	21

Table 3.6. Oscillators details

Column details	Total added mass [g]	Fixed base frequency (f_{fix}) [Hz]	Damping [%]
Aluminium h=100mm (phase I)	75	38.0	0.7
	125	30.5	1.2
	175	26.5	0.9
	275	20.5	1.4
	475	15.0	1.2
	975	10.4	1.5
Aluminium h=100mm (phase II)	75	36.28	0.75
Aluminium h=50mm (phase II)	150	27.02	0.59
Steel h=100mm (phase II)	300	20.37	0.45

Seven different model configurations were tested based on the model setup shown in Figure 3.17. The characteristics of the sample configurations are provided in Figure 3.19. In configuration 1 (Free-Head Pile - FHP), all pile heads are free to rotate and there is no oscillator attached. Configurations 2, 3 and 4 are characterized by free-head piles with the oscillator (Single Degree Of Freedom – SDOF) placed on Pile 1, 4 and 5 head (FHP+SDOF), respectively. Configuration 5 (Short-Cap - SC) has the short-cap connecting piles 4, 5 and 3, without any oscillator. Configuration 6 (SC+SDOF) is

characterized by the short-cap with the oscillator mounted on the central pile. Finally, configuration 7 (Long-Cap - LC) has the long-cap (connecting all the piles) without the oscillator.

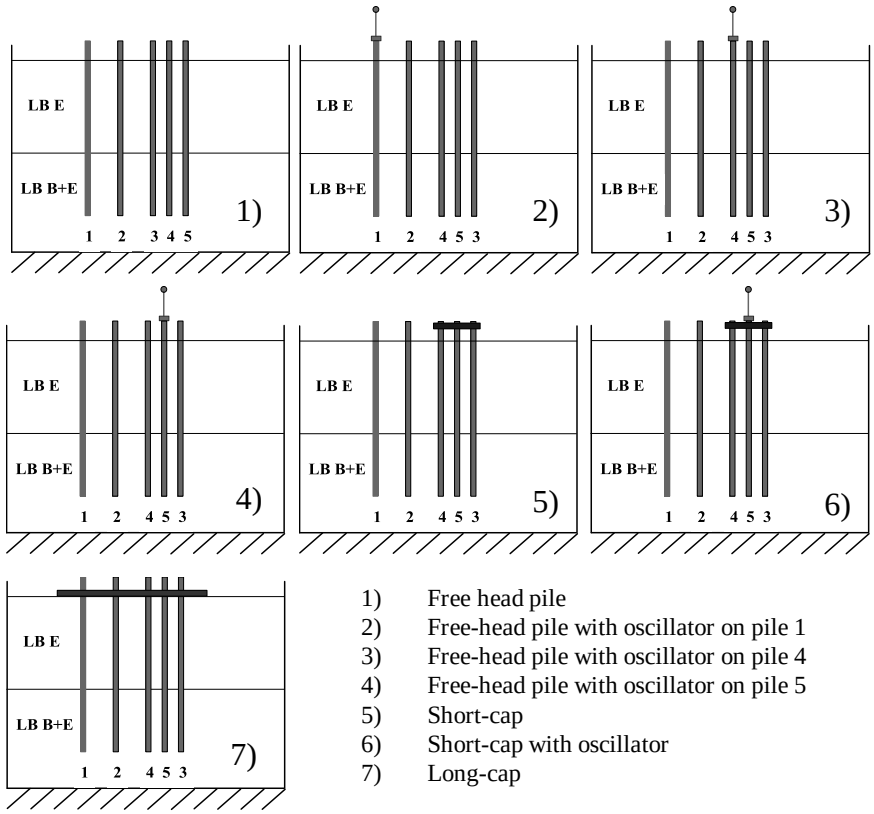

Figure 3.19. Tested model configurations

From Figure 3.20 to 3.24 some pictures of the physical model details set up at the BLADE laboratory are shown.

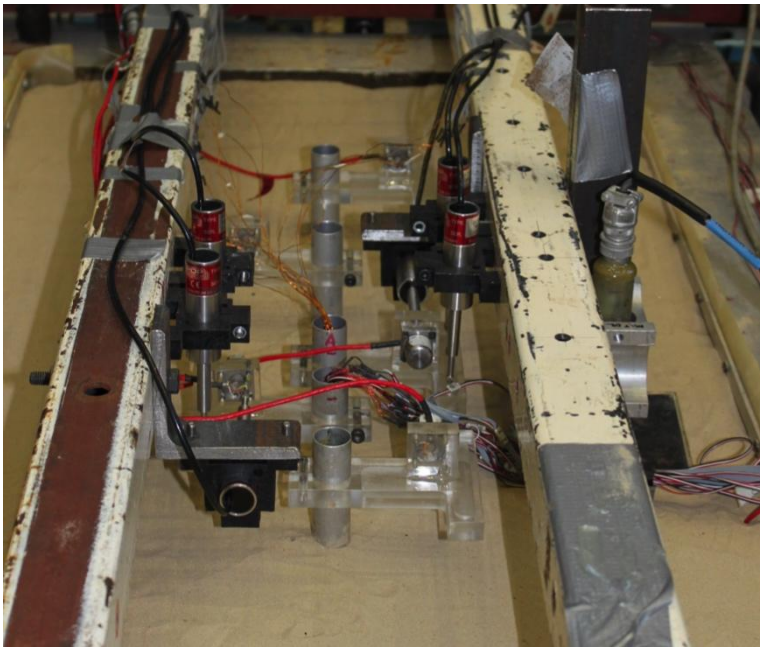

Figure 3.20. Free-head pile configuration (FHP)

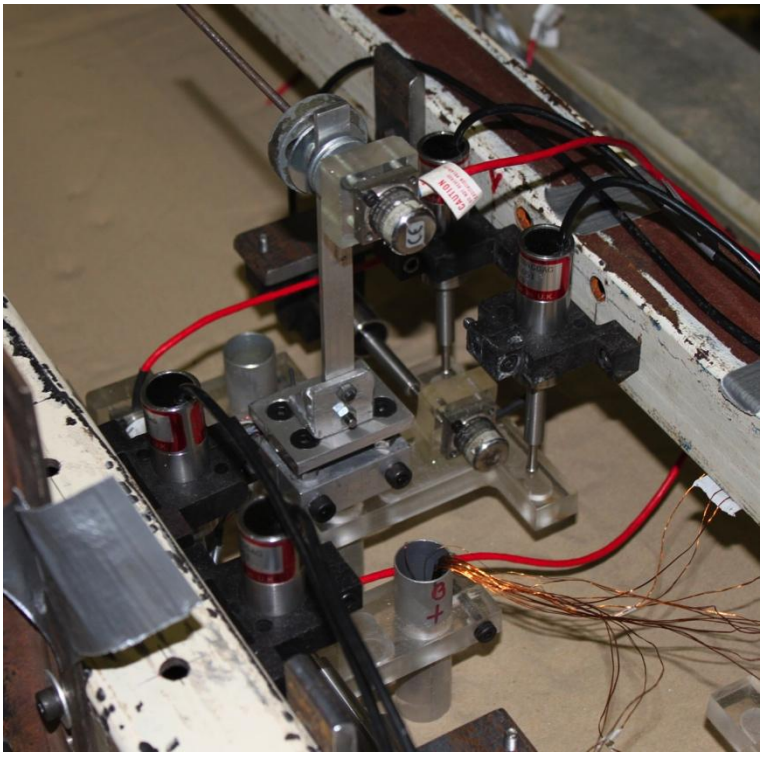

Figure 3.21. Oscillator on free-head pile configuration (FHP+SDOF)

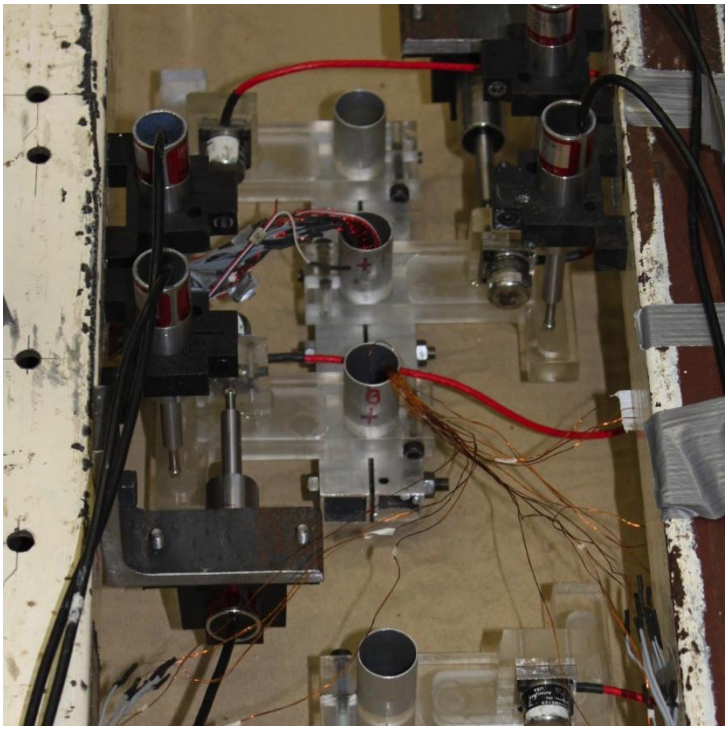

Figure 3.22. Short-cap configuration (SC)

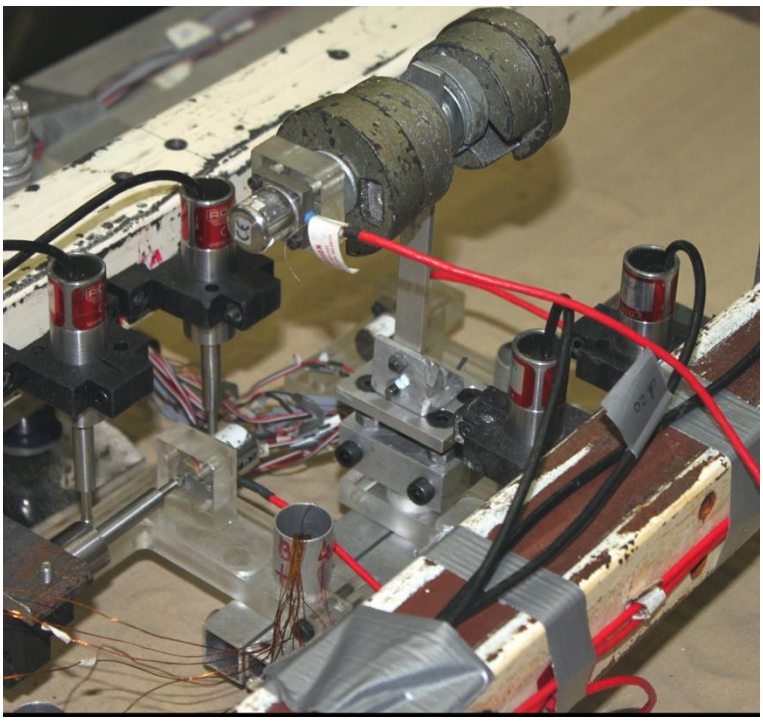

Figure 3.23. Oscillator on short-cap configuration (SC+SDOF)

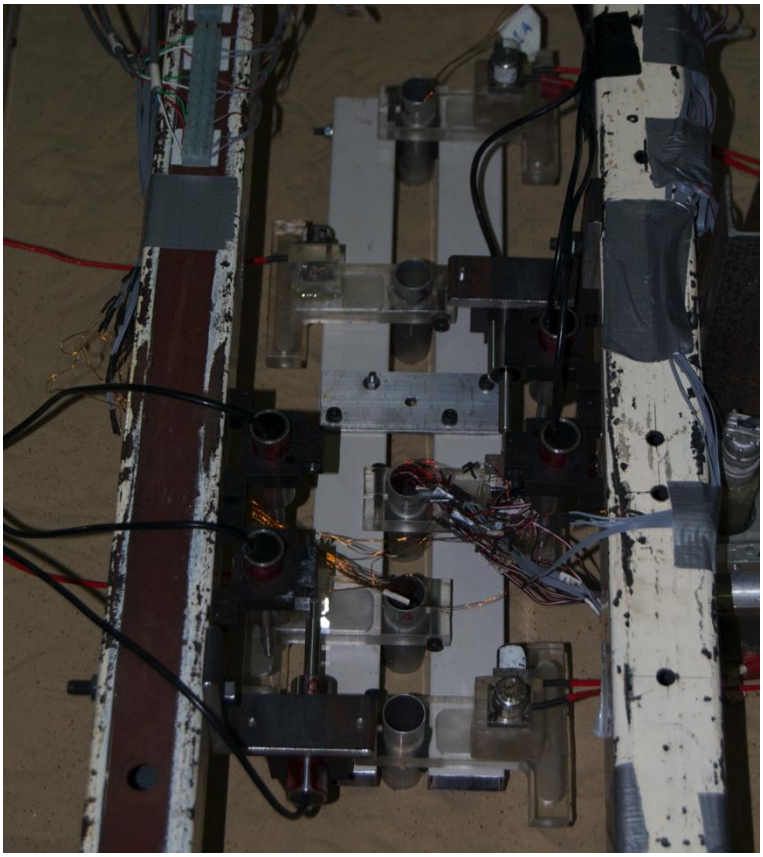

Figure 3.24. Long-cap configuration (LC)

3.4.3 Instrumentation set-up

Accelerometers were used to monitor the accelerations of the shaking table, the shear stack, the soil along a vertical array, the pile heads and the superstructure. The LVDT

transducers were employed to monitor the displacements of the pile in the horizontal and vertical direction. To evaluate the bending response along the piles, eight strain gauge pairs were attached on the shafts of pile 4 and 5; additionally, four strain gauges were placed on the shaft of pile 1 close to the layer interface only in the second phase of testing. In the second phase the no contact displacement Indikon transducer was employed for the evaluation of the settlement of the deposit. Overall, 63 data channels were employed. The locations of the instrumentations are reported in Figure 3.25.

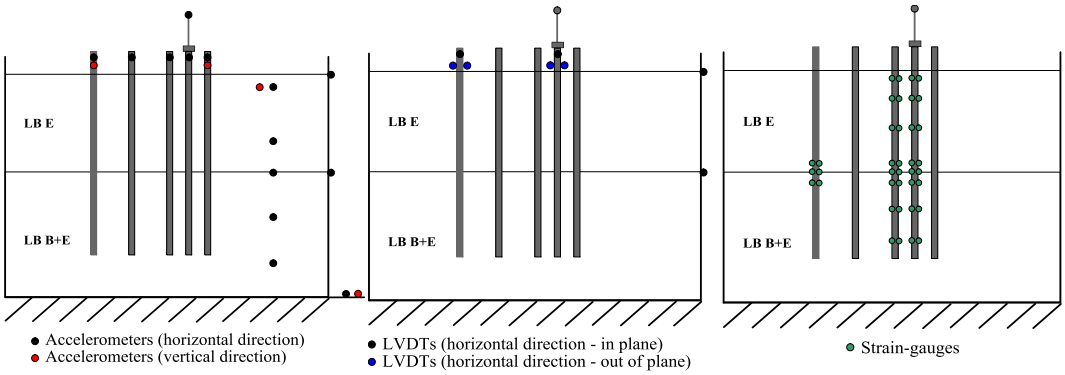

Figure 3.25. Model setup: accelerometers, LVDTs and strain gauges locations

3.5 EARTHQUAKE INPUT

The characteristics of the earthquakes input motion listed in §3.2.1 are reported in Table 3.7. The parameters adopted for the characterization of the ground motions used in this study are:

- Peak Ground Acceleration (PGA);
- Arias Intensity: it is a measure of the energy of a ground motion and determines the intensity of shaking by measuring the acceleration of transient seismic waves;
- Significant duration: defined as the time length in which the Arias Intensity increases from 5% to 95% of the total value;
- Predominant frequency: defined as the frequency at which the maximum spectral acceleration occurs in an acceleration spectrum calculated at 5% damping.

By applying the scaling factor law adopted in this experimental campaign (Table 3.1), the exact scaling factor for the frequency would be around 15 ($SF = n^{0.75}$), but in the tests a scaling factors equals to of 12 and 5 were adopted to ensure to fall in the optimal frequencies range of the shaking table (i.e. 0 – 50 Hz).

Figure 3.26 shows the comparison between the unscaled input motions (left hand-side) with the scaled ones, for a scaling factor equal to 12 (right hand-side).

Table 3.7. Characteristics of unscaled input motions

Input Motion	ID	PGA [g]	Arias Intensity [m/s]	Significant duration [s]	Predominant frequency [Hz]
Tolmezzo (Friuli 1976)	A270	0.315	1.200	4.895	1.56
Sturno (Irpinia 1980)	A000	0.227	1.184	15.024	2.63
Nocera-Umbra Biscontini (Umbria-Marche 1997)	RNC B090	0.314	0.206	1.860	5.56

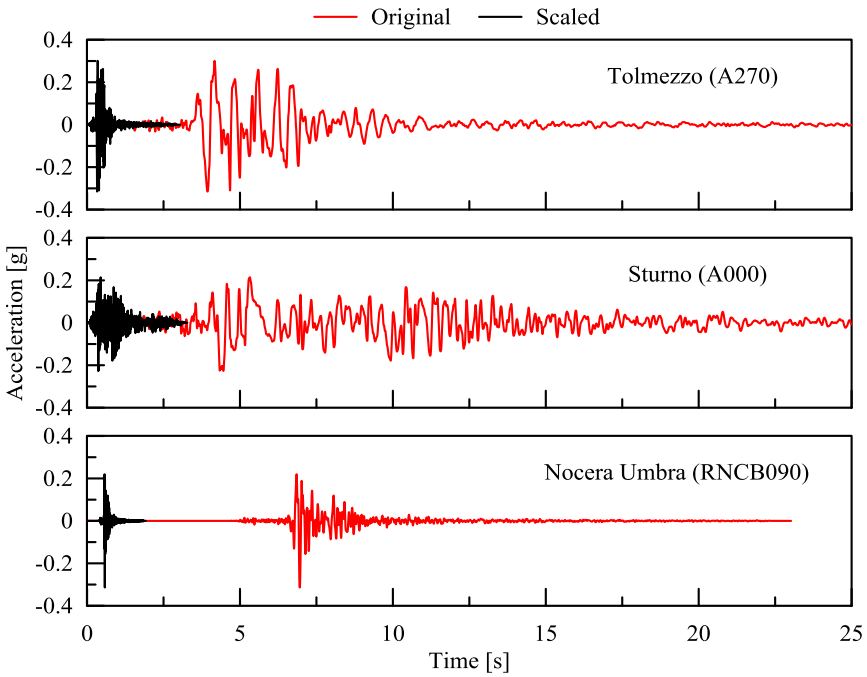

Figure 3.26. Unscaled and scaled (SF12) time histories for selected input motion

In order to study the system response under several strain level, the earthquake motion are scaled to different PGA; the values for each motion are reported in Table 3.8.

Table 3.8. Acceleration scaling

Input Motion	Original PGA [g]	Scaled PGA [g]
Tolmezzo SF12	0.315	0.10
Sturno SF12	0.227	0.15
Nocera-Umbra SF12	0.314	0.57

The shaking table actuators receive the input in terms of displacement time-histories. The procedure used to convert the accelerations into displacements, produce a misfit between the input actually produced by the actuators and the original one. The scaled signals recorded on the shaking table are compared with the ones obtained applying the desired scaling factor and are shown in Figure 3.27.

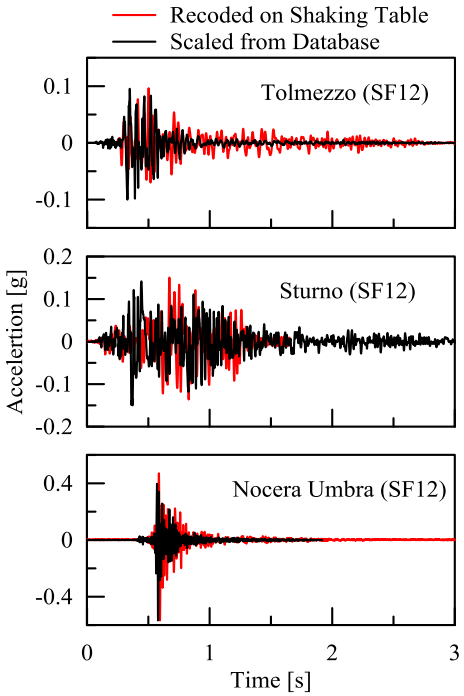

Figure 3.27. Scaled versus recorded input acceleration time histories

4. EXPERIMENTAL RESULTS

Typical results of the comprehensive laboratory experimental program carried out at the BLADE laboratory of the Bristol University are reported in this chapter. Several aspects of the free-field response are investigated; emphasis is posed on the effects of the variation in acceleration and frequency on soil response. The latter response is analysed with respect to the different input motions used in the experiments. The pure kinematic pile response and the complete soil-pile-structure interaction are also considered and discussed.

4.1. FREE-FIELD RESPONSE

The free-field response discussed in this section refers to the case with accelerometers within the deposit. In order to show the capability of the soil container (ESB) to match the soil movements, these recordings are compared against the accelerometers outside the container. The two vertical arrays are shown in Figure 4.1.

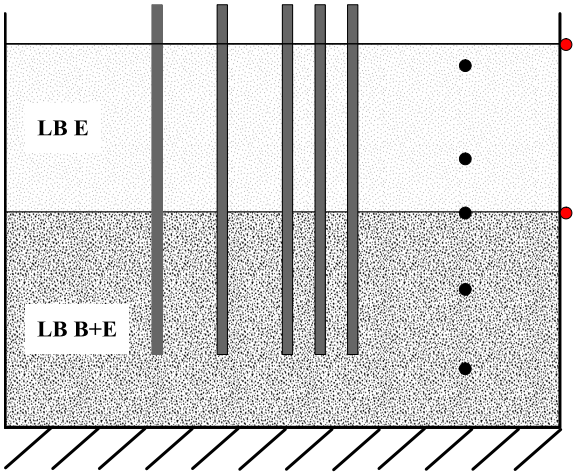

Figure 4.1. Vertical accelerometers array inside (black) and outside (red) the ESB

The comparison between the inside and outside response is possible only around the interface between the two soil layers and the soil surface. Figures 4.2 and 4.3 show the comparison at these elevations. The matching is almost perfect in both cases. The small difference in amplitude around the soil surface is related to the slightly different position of the two accelerometers (z=766 mm for the accelerometer inside the deposit and z=816 mm for the one connected to the shear stack).

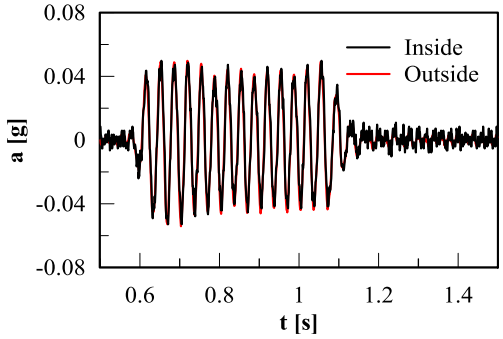

Figure 4.2. Comparison between the inside and outside accelerometers at the layers interface

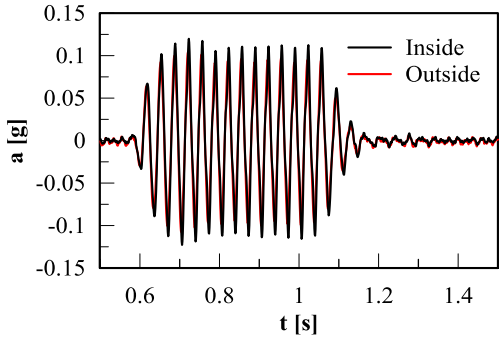

Figure 4.3. Comparison between the inside and outside accelerometers around the soil surface

4.1.1. White-noise response

The white-noise test is an exploratory test formed by a random noise signal of frequency range 0-100 Hz and almost constant acceleration (Figure 4.4).

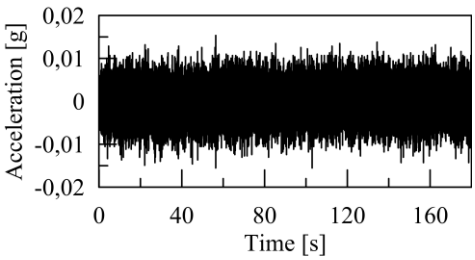

Figure 4.4. Typical white-noise input

This kind of test is useful for the evaluation of the dynamic characteristics of the model. The natural frequency of the whole deposit or the top layer can be evaluated by computing the corresponding transfer functions. More specifically, for the overall

deposit the transfer function is obtained from the ratio between the Fast Fourier Transform (FFT) of the accelerometer located at the surface over the FFT of the one located at the bottom of the deposit (i.e. at the shaking table). To obtain the transfer function of the top layer, the FFT of the signal at the surface is dived by the FFT of the accelerometer at the interface between the two layers. Figure 4.5 shows the typical transfer function for the whole system (Figure 4.5a) and for the top layer (Figure 4.5b).

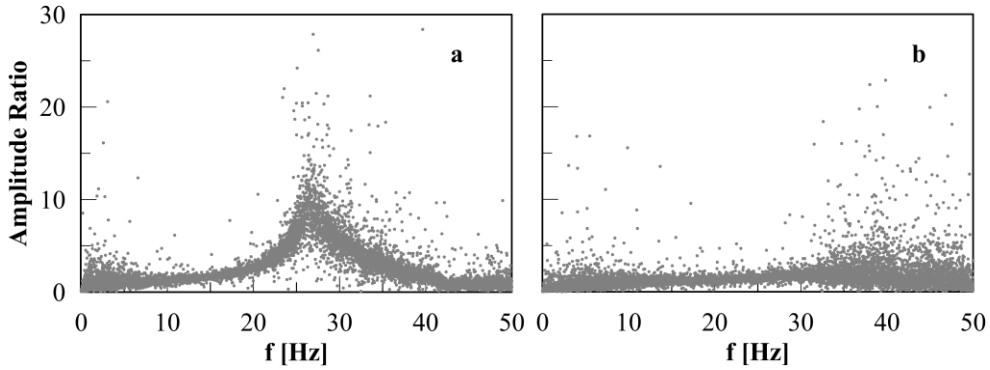

Figure 4.5. Typical transfer function for the overall deposit (a) and the top layer (b)

To estimate the fundamental frequencies of the whole system and of the top layer it is necessary to choose an analytical expression able to fit the experimental data. The theoretical expression for a visco-elastic homogeneous layer over rigid base is used for this aim (Equation 4.1).

$$A(f)=\frac{1}{\sqrt{\cos^2 F+(F\cdot D)^2}} \tag{4.1}$$

Where D is the damping ratio and F is the frequency factor, given by:

$$F(f)=\frac{\omega H}{V_s}=\frac{\pi f}{2f_{nat}} \tag{4.2}$$

where f_{nat} is the frequency of the system.

The transfer functions are computed for all the available white noise tests available to evaluate the influence of the input acceleration on the frequency and equivalent damping.

Figure 4.6 shows the transfer functions of the whole system for all the test performed during the first phase. For a deeper understanding of the behaviour staring to this point, only the fitted curves are reported. To highlight the difference between the lower amplitude test (0.01g) and the higher one (0.1g), the corresponding transfer functions are shown in red in Figure 4.6. The increasing of the input acceleration induces a reduction in terms of frequency (Figure 4.6 and Figure 4.7) and amplitude (Figure 4.6).

This trend can be related to higher soil strains with a consequent reduction of stiffness and increase of damping ratio (Figure 4.8).

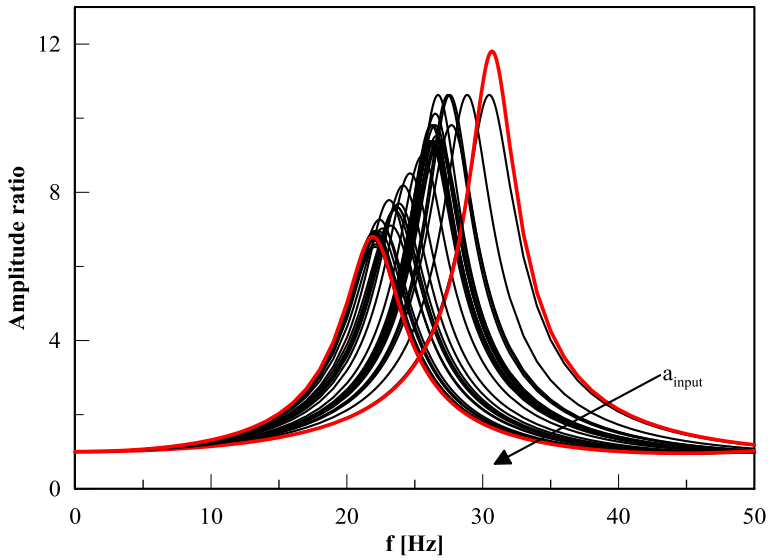

Figure 4.6. Transfer functions of the whole system from all phase I white-noise tests

Figure 4.7 shows the variation of the natural frequency of the whole system with the input acceleration. This representation allows to evaluate the effect of the day of the test in the frequency response. The sequence of tests (included sinedwell tests) increases the relative density of the two-layer soil deposit due to the shaking, which, in turn, increases the stiffness of the medium. For a given acceleration value, day by day, the frequency decreases (day effect). This effect becomes not relevant starting from the second day of testing; this can be probably due to the onset of a maximum relative density of the deposit.

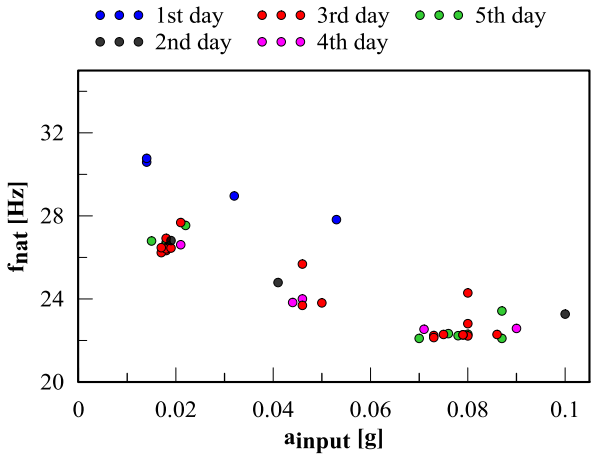

Figure 4.7. Variation of natural frequency of the whole system with input acceleration in phase I

Figure 4.8 shows the variation of the damping ratio with the input acceleration computed using Equation 1. Due to the assumed hypothesis in Equation 1

(homogeneous visco-elastic deposit), it is obvious that the obtained damping values may simply represent the behaviour of the system as a whole. The effect of the day of testing is evident also in Figure 4.8. This effect produces an increasing of the damping ratio with the increasing of the stiffness of the deposit. From the second day of testing this effect tends to vanish.

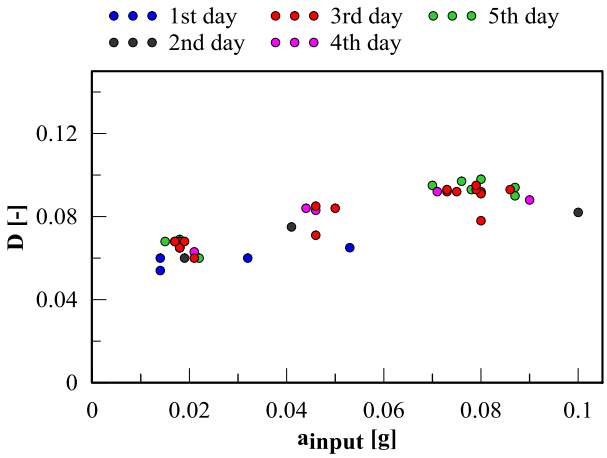

Figure 4.8. Variation of damping ratio of the all system with input acceleration in phase I

Similar analyses are carried out for the evaluation of the natural frequency of the top layer. Figure 4.9 shows the transfer functions of the top layer for the white noise tests performed in phase I. Figure 4.9 shows a different trend compared with the whole system for both, frequency (Figure 4.10) and damping ratio (Figure 4.11) variations.

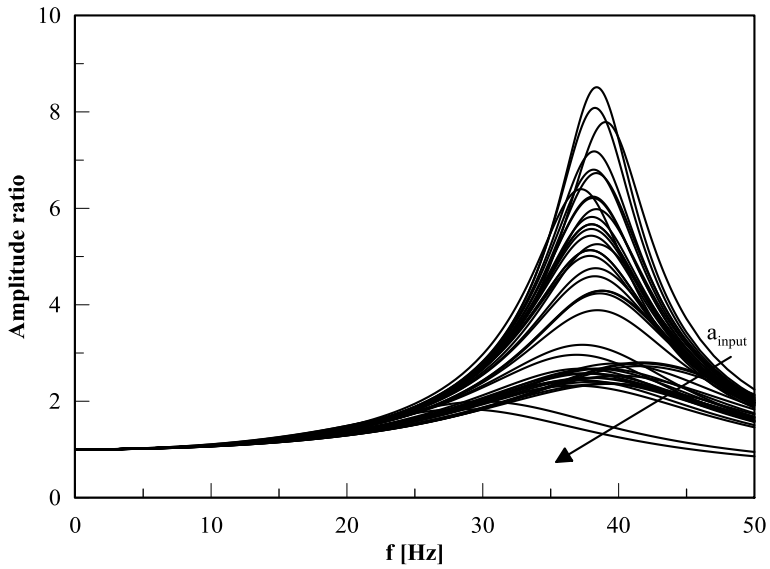

Figure 4.9. Transfer functions of top layer from all phase I white-noise tests

Figure 4.10 shows that the reduction of the natural frequency is not as evident as for the whole system (Figure 4.7). This is probably due to the shaking of the table that

generates the maximum increasing in stiffness in the top layer, thus inducing a small reduction of frequency with the increasing of acceleration.

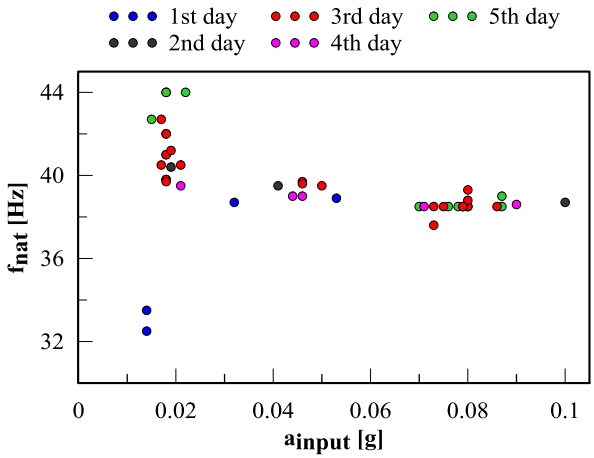

Figure 4.10. Variation of natural frequency of the top layer with input acceleration in phase I

For the top layer the assumptions used for Equation 4.1 are more restrictive, especially for the hypothesis of homogeneous layer over rigid base, for this reason the above equation is simply used to roughly identify the natural frequency, but not for the evaluation of the damping ratio.

Similar analyses are carried out for the white-noise tests performed in the second phase of testing. In the second phase, the results are coherent with those obtained during the first phase. For this reason only the variation in terms of frequency (Figure 4.11 and 4.12) and damping ratio (Figure 4.13) are reported for these data for the whole system and the top layer, together with the phase I result to show the repeatability of the tests in the two phases. To provide a context to the variations of natural frequency of the whole system (Figure 4.11), of the top layer (Figure 4.12) and the variation of the damping ratio for the whole system (Figure 4.13), with the input acceleration, linear fittings are shown, together with their equations and a measure of the accuracy of the fittings (R^2); the fittings should be intended only as a tools to evaluate general trends.

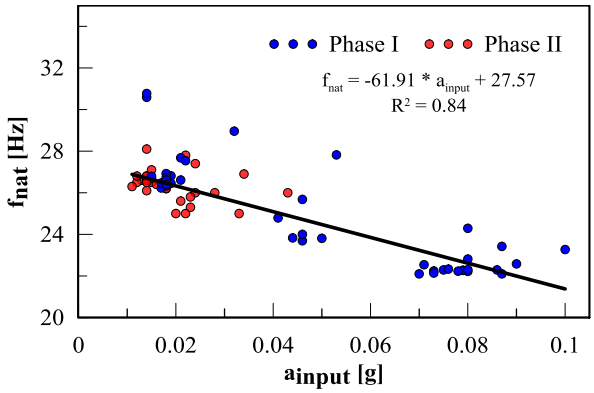

Figure 4.11. Variation of natural frequency of the whole system and its linear fitting with input acceleration

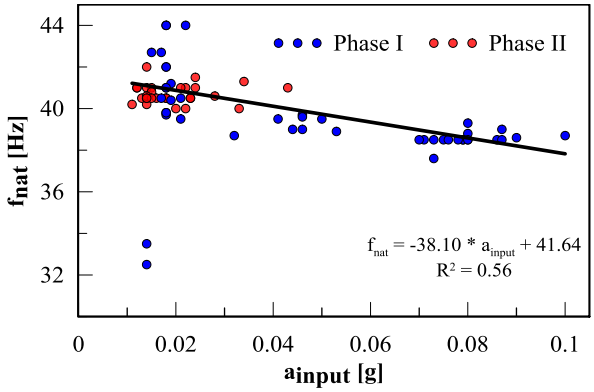

Figure 4.12. Variation of natural frequency of the top layer and its linear fitting with input acceleration

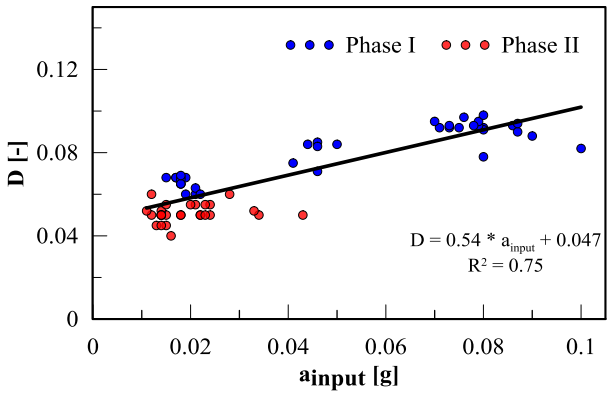

Figure 4.13. Variation of damping ratio of the whole system and its linear fitting with input acceleration

4.1.2. Harmonic response

Harmonic tests were used to evaluate the effect of the input frequency on the soil response. Figure 4.14 shows the comparison of seven sinedwell tests with the same input acceleration and different frequency values. The acceleration values reported in Figure 4.14 correspond to the absolute maxima for each depth. The frequency effect is

evident: the maximum amplification occurs when the input frequency is close to the natural frequency of the deposit (25-30 Hz).

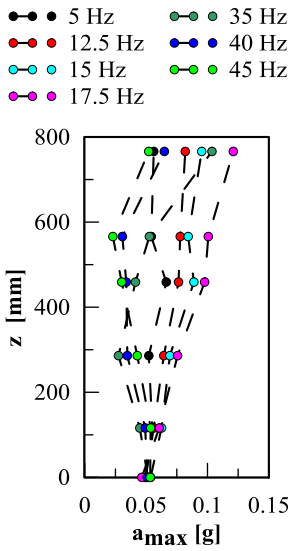

Figure 4.14. Frequency effect of sinedwell input motion (a=0.05g)

To further assess this effect, Figures 4.15 shows the amplification factor for the whole system and the top layer for each frequency for the tests reported in Figure 4.14, computed using the following equations:

$$A_{all}=\frac{a_{top}}{a_{input}} \tag{4.3}$$

$$A_{top}=\frac{a_{top}}{a_{interface}} \tag{4.4}$$

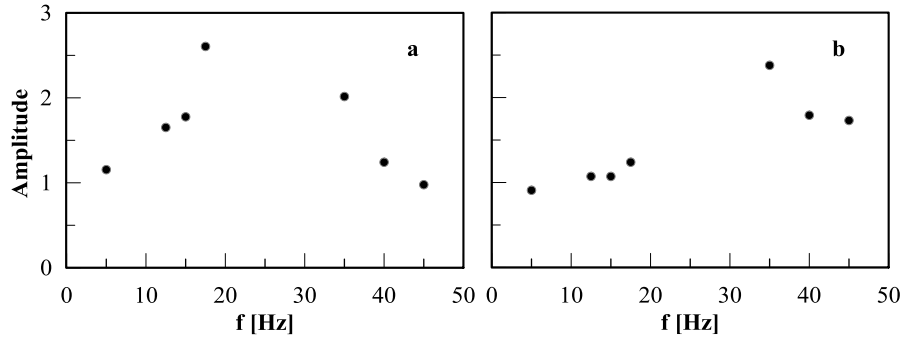

Figure 4.15. Amplification of the whole system (a) and top layer (b) for the sinedwell tests

It is clear that with a larger range of input frequency at the same acceleration it is possible to obtain the natural frequency of both upper layer and the whole system.

Another typical result of the sinedwell tests is represented by the variation of the input acceleration with a constant input frequency. Figure 4.16 shows the time-history responses of the free-field soil accelerations. These values refer to the application of a

sinedwell input motion with three increasing levels of input acceleration applied on the shaking table, namely 0.027g, 0.040g and 0.067g. The frequency of the input motion is 30 Hz. The free-field response increases with the increasing of the input acceleration level. The recorded accelerations are compliant with the input motion as also shown in the diagrams in the lower part of Figure 4.16, where the peak acceleration profile in the soil (quoted as a_{max}) is plotted. Figure 4.17a shows that the profiles of a_{max} exhibit similar shapes. These shapes are also compared in Figure 4.17b, where the dimensionless curves obtained by the ratio of Δa_{max} (computed as $a_{max}(z)$ minus the minimum value of a_{max} along the vertical axis) over the maximum value of Δa_{max} are plotted versus depth for the three sample tests. As expected, for this level of acceleration the shape function does not depend on the acceleration but is related to the input frequency. This effect is due to the fact that for small strain levels (the soil behaviour is still linear), the dynamic response of the system is dominated by the frequency of the input and by the ratio between it and the natural frequencies of the system.

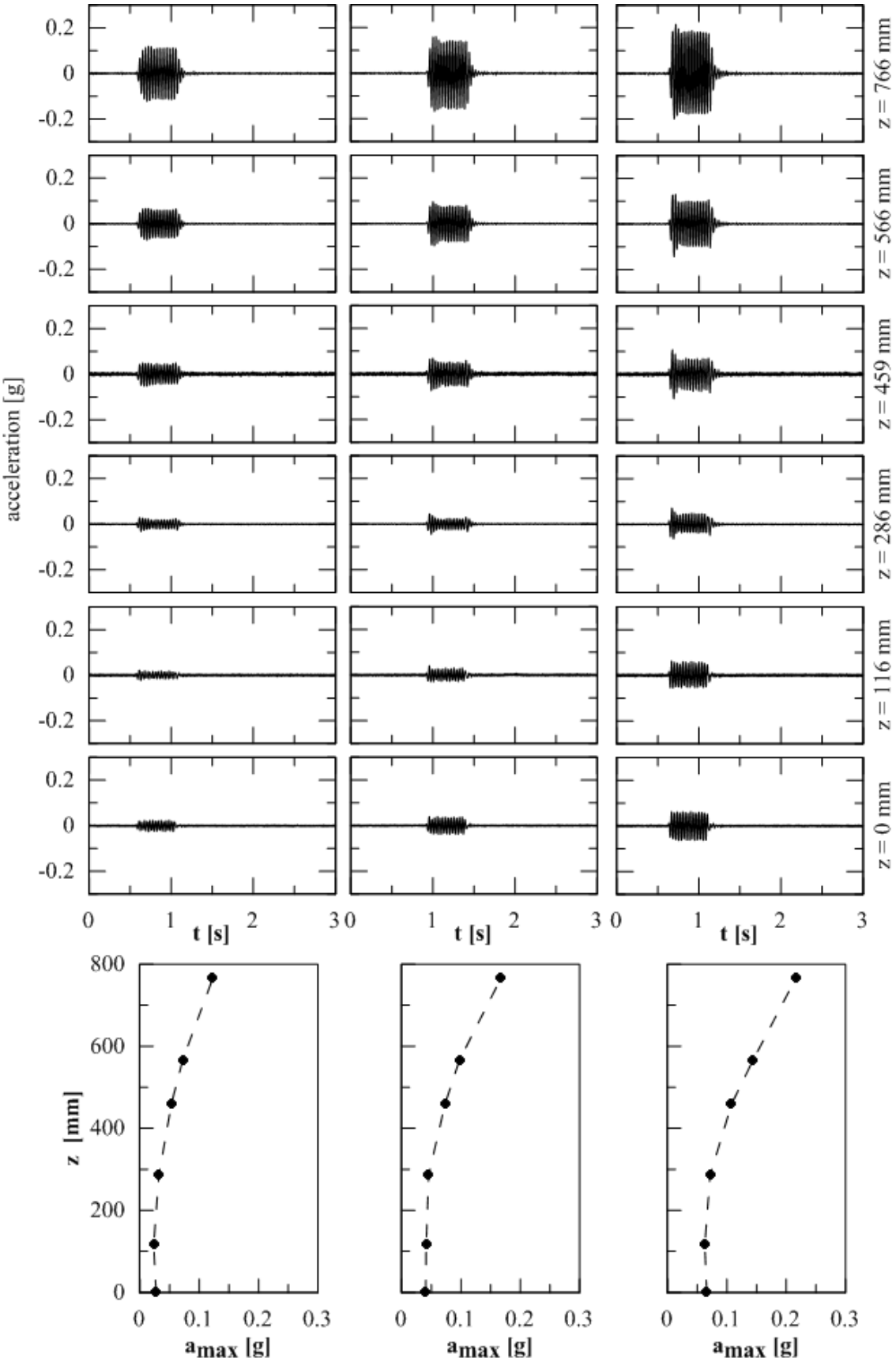

Figure 4.16. Time-histories and envelopes of free-field response for different amplitude of input acceleration

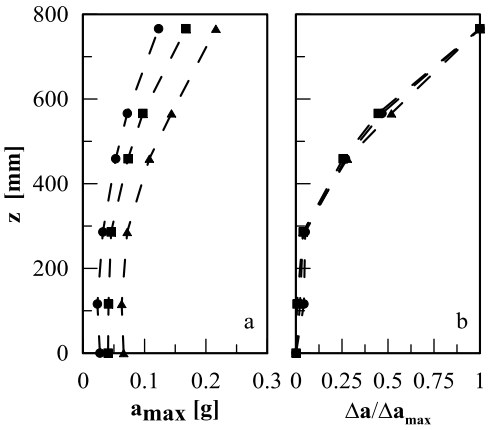

Figure 4.17. Envelope (a) and dimensionless acceleration profiles (b) vs. depth for different amplitudes of input accelerations

4.1.3. Earthquake response

In this paragraph a typical soil response to an earthquake input is reported. In the left hand-side of Figure 4.18 the maxima accelerations in the free-field condition is reported. The input considered (shown in the bottom part of right hand-side of Figure 4.18) is the Tolmezzo record scaled 12 times in frequency with a maximum acceleration equal to 0.1g. The amplification stems also from the time-history of the accelerations at the given depths, as for example input, interface and surface levels.

Figure 4.19 shows the FFTs of the three signals shown in Figure 4.18. Again, the amplification that occurs in the soil deposit, it is evident. The most important feature that can be observed in Figure 4.19 is the frequency range amplification (20-30 Hz) in which is contained the natural frequency of the soil. Such response can also be derived from Figure 4.7.

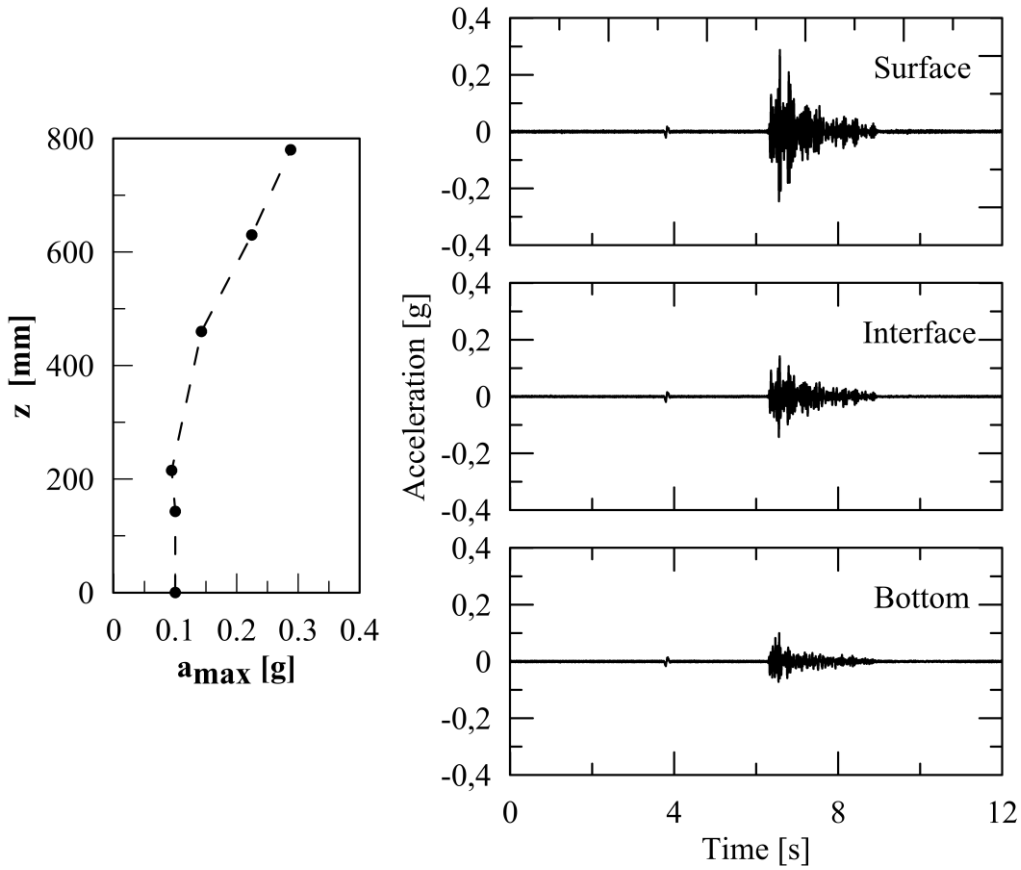

Figure 4.18. Typical free-field response (input: Tolmezzo SF12, PGA 0.1g)

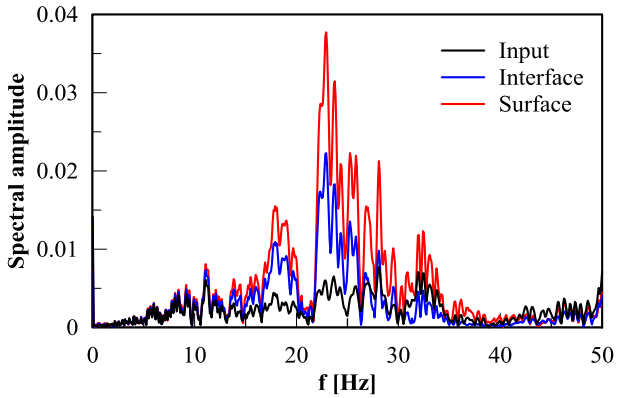

Figure 4.19. FFTs of the input, interface and surface signals for Tolmezzo SF12 earthquake

The settlements during the second phase of tests are evaluated using the indikon results. Figure 4.20 shows the cumulative settlements for each test. The maximum settlement occurs in the third and fourth days (i.e. the days in which the earthquakes were performed). In table 4.1 the initial and the final relative densities for each soil layer are reported. For the repartition of the total settlement measured by the indikon two different hypotheses are considered. Taking into account the very low initial relative density of the top layer, in the first case the total settlement is assigned to the top layer, whereas in the second case the 80% is assigned to the top and the 20% to the

bottom layer. As expected, a significant variation in terms of relative density occurs in the top layer. This variation can allow to a variation of the dynamic response of the system, due to the increasing of stiffness.

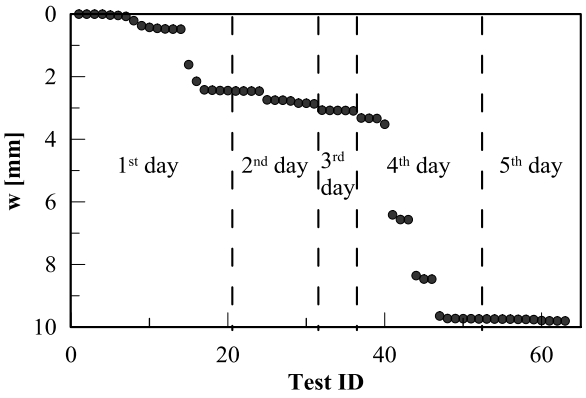

Figure 4.20. Settlements for each test

Table 4.1. Relative density variation

		H [m]	mass density [kg/m^3]	n [-]	e [-]	e_{min}	e_{max}	D_r [%]
Initial	Upper layer	0.34	1339.15	0.49	0.98	0.61	1.01	9.32
	Bottom layer	0.46	1826.82	0.31	0.45	0.29	0.61	50.78
w = 100% upper	Upper layer	0.33	1378.91	0.48	0.92	0.61	1.01	23.53
	Bottom layer	0.46	1826.82	0.31	0.45	0.29	0.61	50.78
w = 80% upper + 20% bottom	Upper layer	0.33	1370.77	0.48	0.93	0.61	1.01	20.69
	Bottom layer	0.46	1834.64	0.31	0.44	0.29	0.61	52.68

4.2. PILE RESPONSE

Typical pile responses are reported herein referring to harmonic tests. Two different model configurations are considered: *(i)* free-head pile (no connection at pile head, FHP) to analyse the pure kinematic interaction and *(ii)* short-cap connection among piles head (SC) to analyse the connection effect on the pile head and at the interface. As explained in §3.3.vii, the pile response is investigated in terms of bending moment and axial force using strain-gauges responses located at different piles elevations.

4.2.1. Harmonic response

i) Kinematic interaction at soil interface

By using the results of the free-head pile configuration (Figure 4.21), the evaluation of the pure kinematic interaction was carried out.

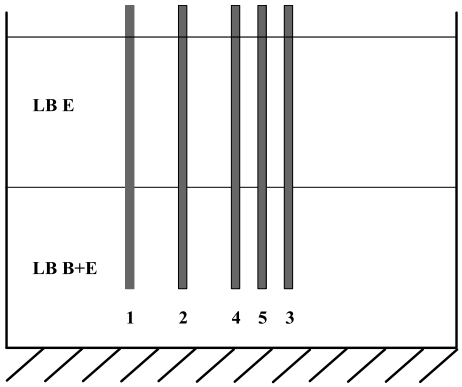

Figure 4.21. Free-head pile configuration

The set of data used herein refer to the same input considered in the second part of §4.2.1 (sinedwell tests with input frequency 30 Hz and increasing accelerations). Two examples of measured strain time-histories and corresponding bending moments of pile 4 are shown in Figure 4.22 and 4.23 for input acceleration equal to 0.027g and 0.067g respectively. These responses were selected as they correspond to typical response of the sample pile groups. For the input acceleration of 0.027g (Figure 4.22) the strains appear almost symmetric respect to the horizontal axis and in opposite phase, which suggests the pure bending acting on pile. Additionally, when the excitation stops, strains return to zero, with no residual deformations. On the contrary, for the input acceleration equal to 0.067g (Figure 4.23) the strain time-histories show a residual deformation that produce a residual bending moment and axial force.

Piles deflection during shaking can be obtained considering the instantaneous response at representative instants. The selected times (marked with circles in Figure

4.24) correspond to peaks in the input signal for the test with input acceleration equal to 0.027g.

Figure 4.25 reports the instantaneous responses for the soil column, pile 4 and pile 5. By examining Figure 4.25, it is possible to conclude that the soil response is consistent with the first mode shape; according to the expected response, the shapes of the pile deformation show three inversions due to the presence of the interface.

The absolute maxima computed bending moments at each pile elevation are reported in Figure 4.26 for pile 4 and 5. As expected, piles exhibit zero moments at the top and bottom, due to the absence of restraints. The kinematic interaction increases with the input acceleration level and the maximum bending moment is located around the soil interface. It is also interesting to observe the different response of the two instrumented piles. Pile 4 exhibits higher bending moments respect to pile 5 due to the different local condition transferred by surrounding soil and piles. Pile 4 is the external pile of the small group (formed by piles 4, 5 and 3) while pile 5 is the internal one (Figure 4.21) which exhibits lower stresses.

The effect of the input acceleration on kinematic pile response is also evident in Figure 4.27 were the maximum bending moments are reported for different input motions. Additionally in Figure 4.27 several existing formulations for the evaluation of the kinematic effects are reported (Margason and Holloway, 1977; Dobry and O'Rourke, 1983; Mylonakis, 2001; Nikolaou et al., 2001). The analytical solutions tend to overestimate the kinematic bending moment, especially for the lower accelerations.

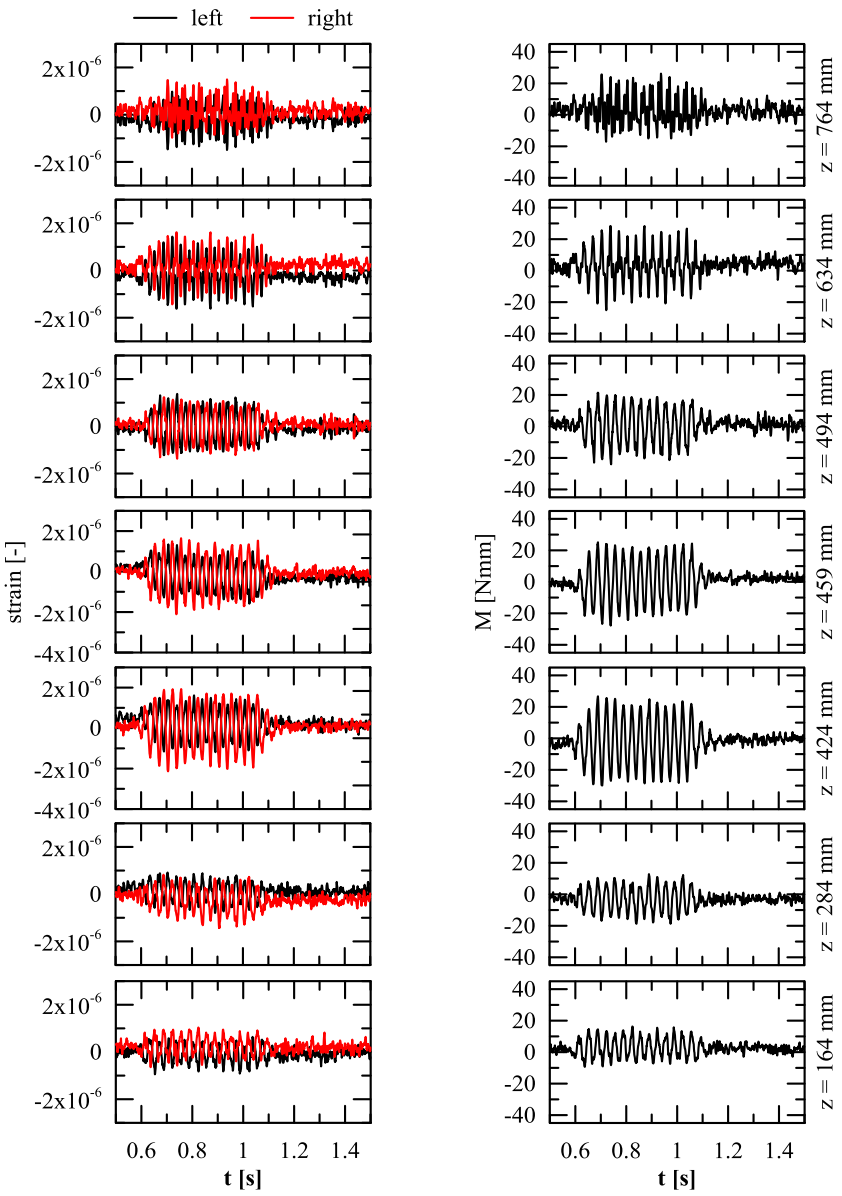

Figure 4.22. Time-histories of measured strains (left) and computed bending moments (right) along pile 4 for input acceleration equal to 0.027g

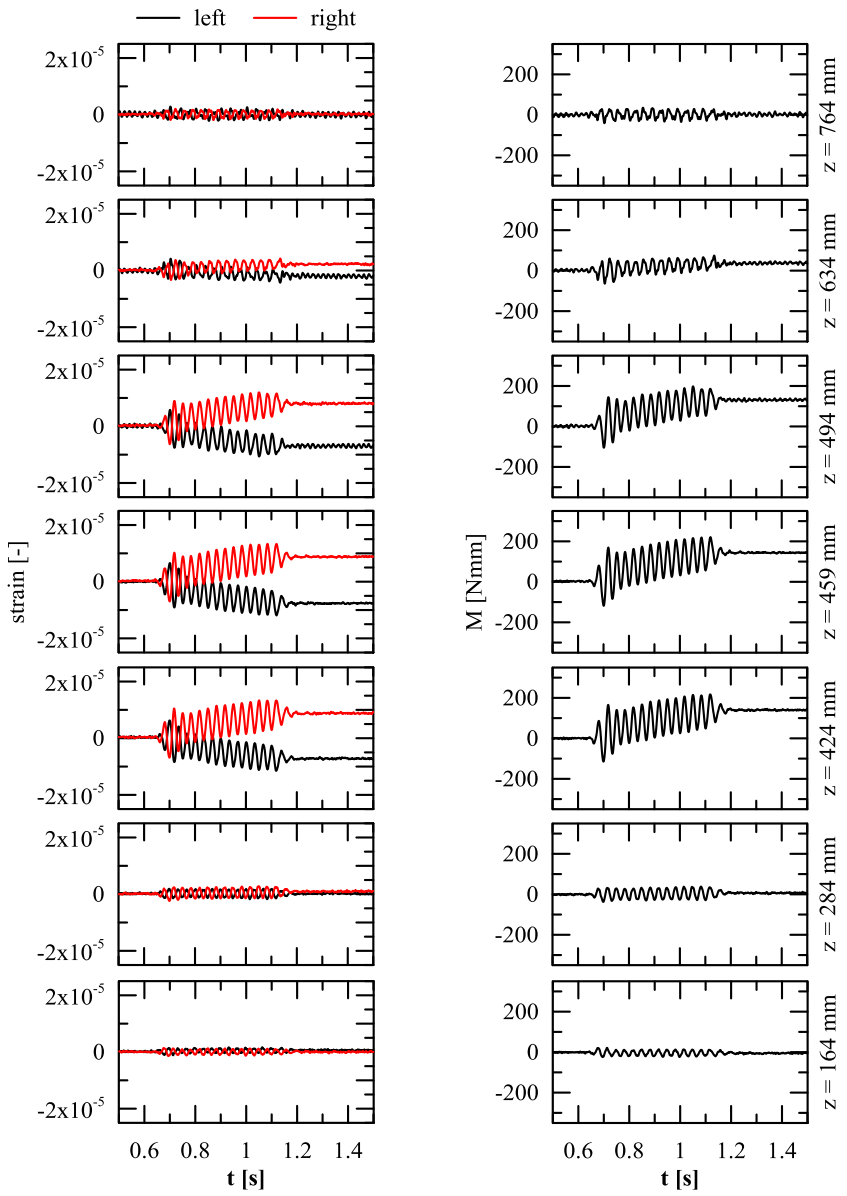

Figure 4.23. Time-histories of measured strains (left) and computed bending moments (right) along pile 4 for input acceleration equal to 0.069g

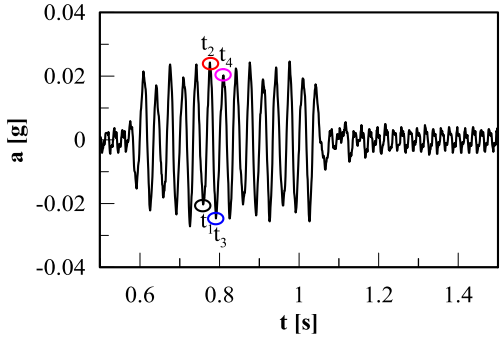

Figure 4.24. Input time history and selected instants (FHP configuration)

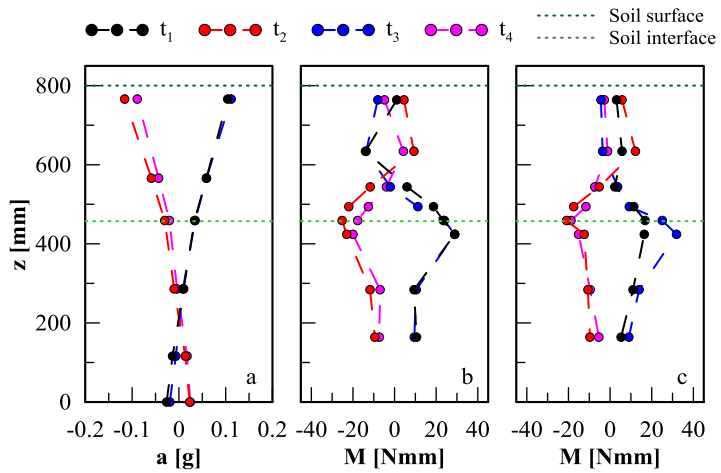

Figure 4.25. Instantaneous responses for soil column, pile 4 and pile 5 (FHP configuration)

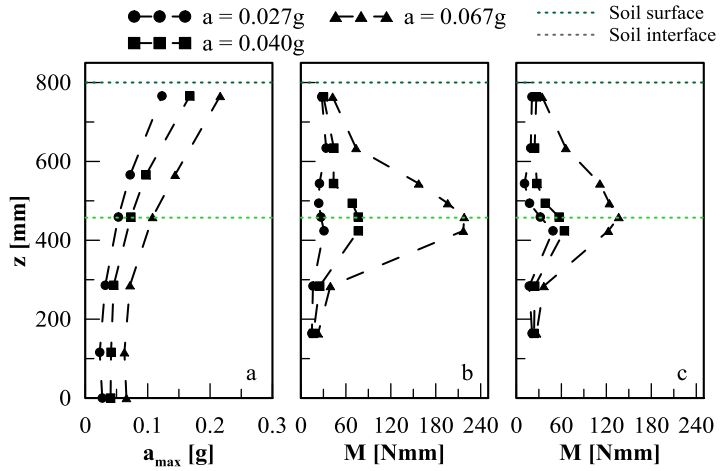

Figure 4.26. Envelope of absolute maximum soil acceleration (a) bending moments along pile 4 (b) and 5 (c) for 30 Hz input frequency and increasing accelerations (0.027g- 0.069g)

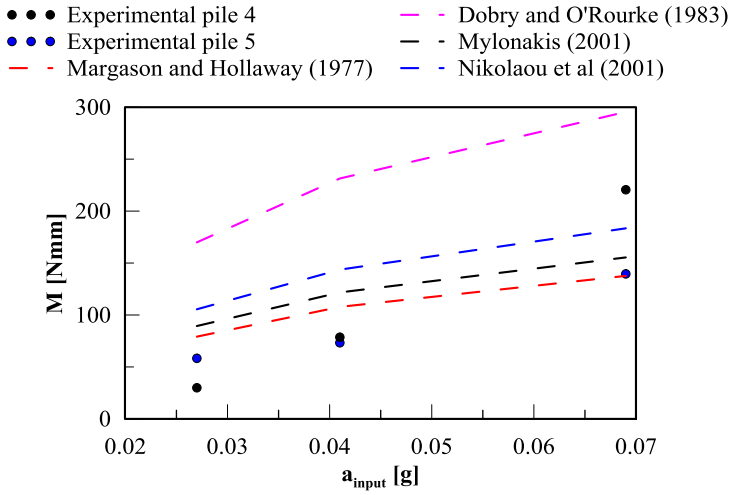

Figure 4.27. Kinematic bending moments versus input accelerations: experimental and analytical results

ii) Pile head response

The evaluation of the pile head response is evaluated considering the short-cap pile configuration (Figure 4.28).

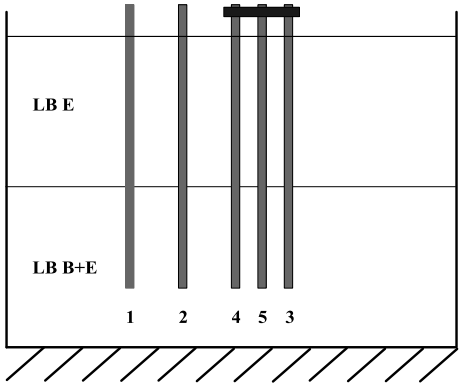

Figure 4.28. Short-cap configuration

The set of data considered to analyse the pile head response is quite large; the frequency and input acceleration chosen are reported in Figure 4.29.

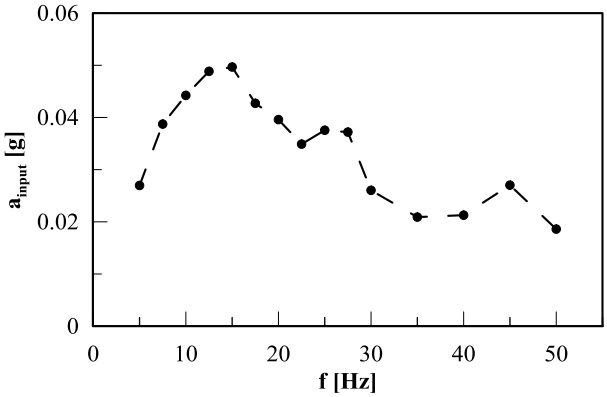

Figure 4.29. Frequencies and accelerations of the sinedwells input

Using Equation 4.3, the amplification factor for the whole system is computed and reported in Figure 4.30. The maximum soil amplification occurs for the sinedwell with frequency equal to 22.5 Hz. This information is useful because the bending moment at the pile-head is related to the surface acceleration. Additional evidence of such effect can be found in Figure 4.31 where the absolute maxima bending moments for the short-cap configuration are reported for each test considered for both the instrumented piles (piles 4 and 5). The same shape of Figure 4.30 and 4.31 demonstrates the close relationship between these two quantities. As expected the pile connection generates almost the same bending at the two pile heads. In Figure 4.31 the computed pile-head bending moment using the de Sanctis et al. (2010) formulation are also reported. This formulation is able to predict the experimental values in an accurate manner.

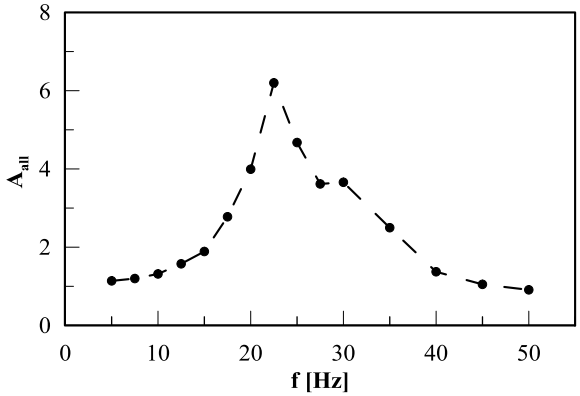

Figure 4.30. Soil amplification for the whole system

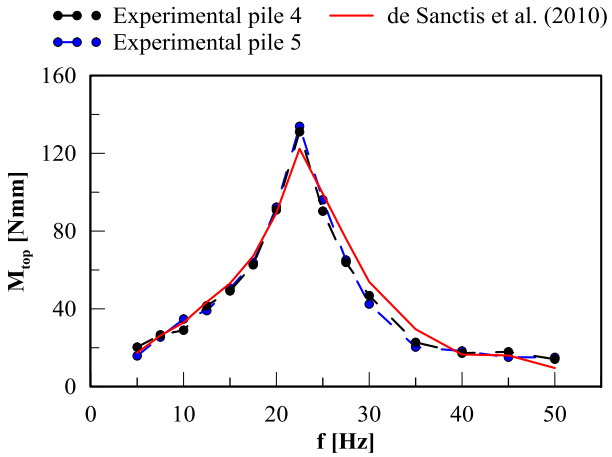

Figure 4.31. Pile - head bending moments for each test

Figure 4.32 shows the envelopes of the absolute soil accelerations (Figure 4.32a) and piles bending moments (Figures 4.32b, c). The effect of the pile connection is clear in all tests; it does not dependent on the input frequency (and to the resonance condition).

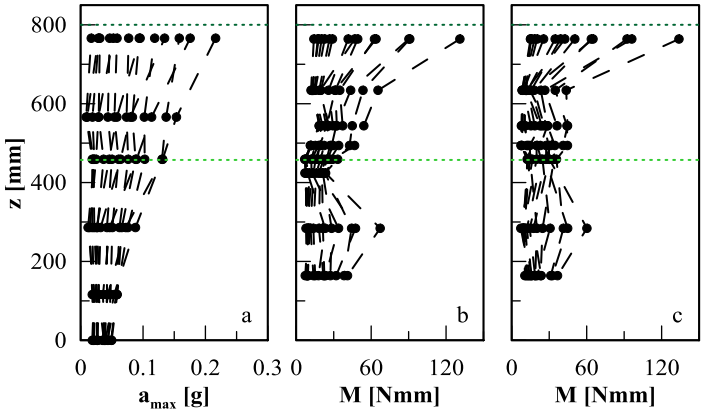

Figure 4.32. Envelope of absolute soil acceleration (a) and bending moments along pile 4 (b) and 5 (c) for all the tests reported (SC configuration)

Soil and pile deflections for the short-cap configuration are evaluated from the responses at fixed instants. Referring to the test with frequency equal to 30 Hz and input

amplitude equal to 0.03g. In Figure 4.33 the instants considered for such analysis types are marked with circles.

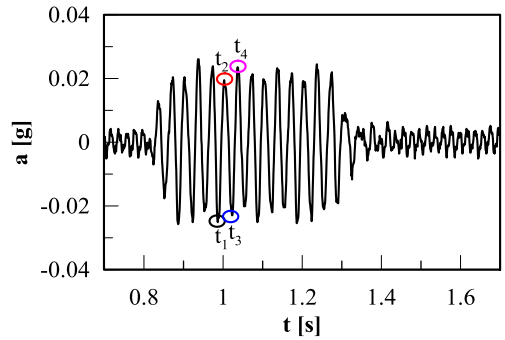

Figure 4.33. Input time history and selected instants (SC configuration)

The system response at marked instants is reported in Figure 4.34. The soil response is not affected by the connection at the pile head, while the pile responses show the increasing of bending moments at the pile head due to the connection.

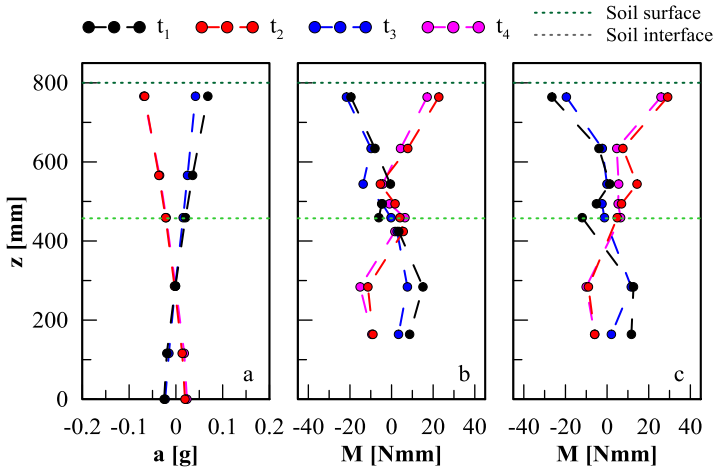

Figure 4.34. Instantaneous responses for soil column (a), pile 4 (b) and pile 5 (c) for SC configuration

iii) Configuration effect

The effect of the pile head condition can be evaluated comparing the two configurations (SC and FHP). To this aim, in Figure 4.35 the instantaneous responses of these two configurations are reported for soil, pile 4 and pile 5 excited by the same input motion (f=30 Hz and a=0.03g). The soil response in the selected instant is almost the same for both the configuration (Figure 4.35a). From the analysis of Figures 4.35b and 4.35c it is clear that piles deflections is influenced by the presence of the connection even around the layers interface. In the SC configuration, the bending at the top generates a bending redistribution along the piles that generate a lower bending at the layer interface compare to ones obtained in the FHP configuration. This behaviour is

more evident comparing directly the envelope of the absolute bending moments along pile 4 and 5 for these two configurations (Figure 4.36).

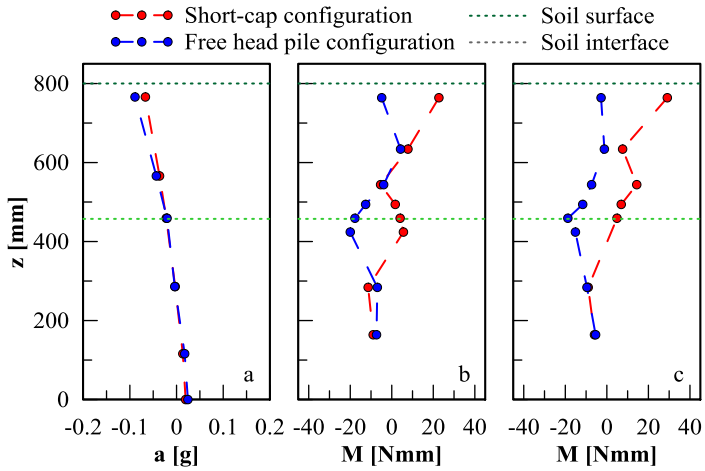

Figure 4.35. Instantaneous responses for soil column (a), pile 4 (b) and pile 5 (c) for short-cap (red) and free head pile (blue) configurations

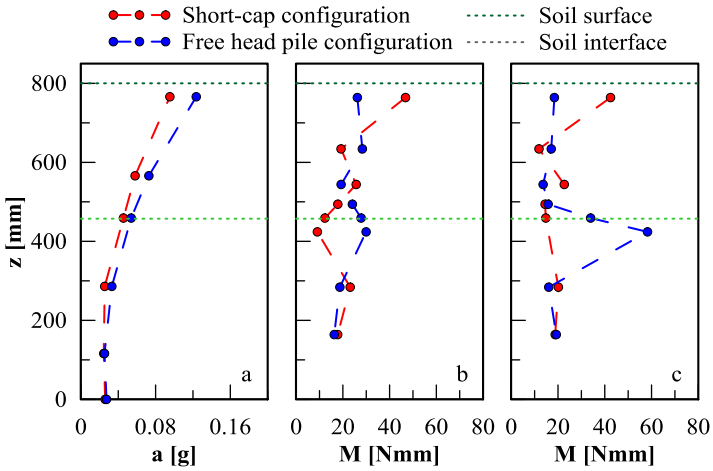

Figure 4.36. Envelope of free-field accelerations (a) and bending moments along piles 4 (b) and 5 (c) for short-cap (red) and free head pile (blue) configurations

4.2.2. Earthquake response

A typical pile response due to an earthquake input is reported herein. The pile configuration is the free head. The input considered is the Nocera Umbra Biscontini record, scaled 12 times in frequency with the maximum input acceleration equal to 0.57g (Figure 4.37).

For this earthquake input, the analyses of the instantaneous profiles are computed for the instant in which the maximum acceleration occurs at the interface (Figure 4.38).

The instantaneous profiles are reported in Figure 4.39. The comparison between the soil (Figure 4.39a) and pile responses is consistent with the behaviour observed for the harmonic tests.

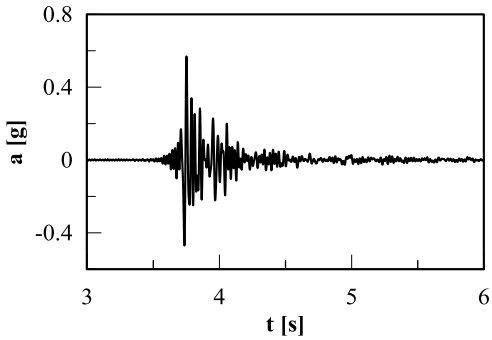

Figure 4.37. Nocera Umbra Biscontini record (SF 12)

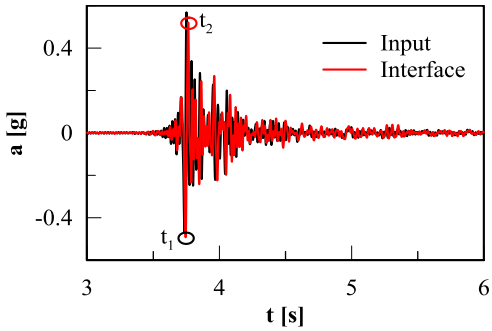

Figure 4.38. Input and interface accelerations for Nocera Umbra signal (SF12)

Figure 4.40 shows the envelopes of the absolute maximum soil acceleration in the free-field condition along depth and the bending moments for pile 5.

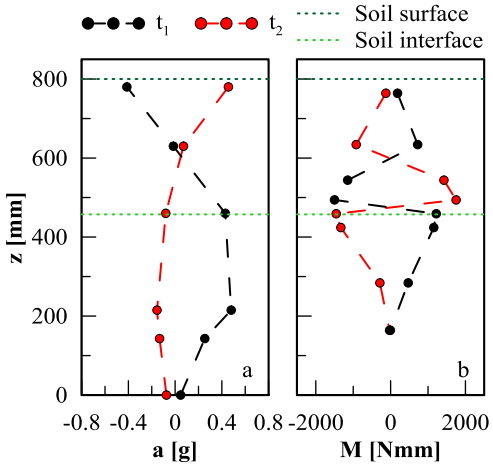

Figure 4.39. Instantaneous profiles for soil accelerations (a) and bending moments along pile 5 (b)

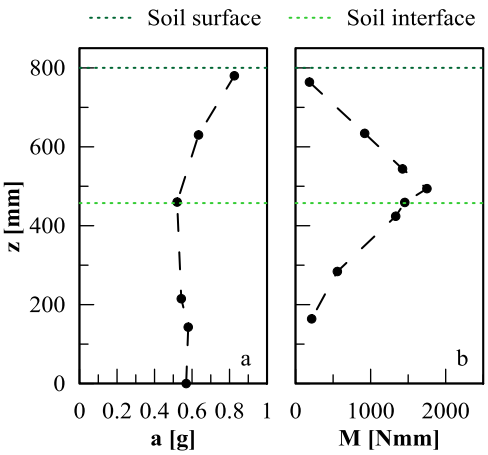

Figure 4.40. Envelope of absolute soil accelerations in free-field condition (a) and bending moments along pile 5 (b)

4.3. SOIL-PILE-STRUCTURE RESPONSE

The estimation of the fixed base response is a crucial information to estimate reliably the soil-pile-structure interaction. For this reason, in the experimental campaign the dynamic response of the fixed base oscillator is investigated attaching the oscillator directly to the shaking table (Figure 4.41) and performing white-noise tests.

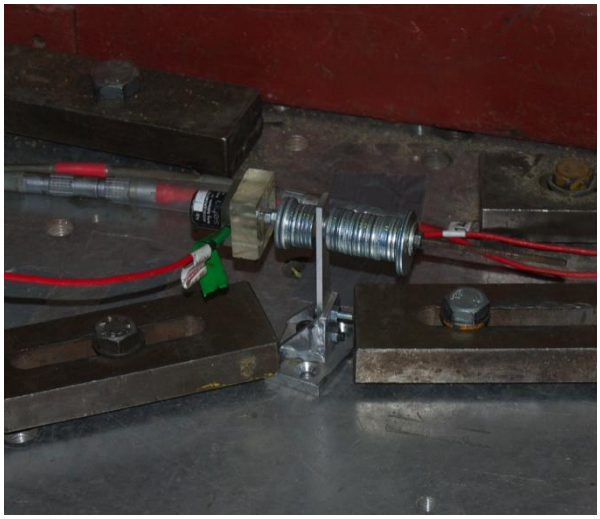

Figure 4.41. Fixed base oscillator

The dynamic properties obtained from these tests, already reported in §3.4.2, are shown in Table 4.2 and adopted for the evaluation of the period elongation. It is arguable that the damping ratio increasing with the increasing of the mass, could be related to the effect of the movement of the elements added at the top of the column, to achieve the desired mass.

Table 4.2. Properties of the sample oscillator

Column details	Total added mass [g]	Fixed base frequency (f_{fix}) [Hz]	Damping [%]
Aluminium h=100mm	75	38.0	0.7
	125	30.5	1.2
	175	26.5	0.9
	275	20.5	1.4
	475	15.0	1.2
	975	10.4	1.5

The soil-pile structure interaction effects are analysed referring to the different pile-head configurations, namely free-head pile (FHP) and short-cap connection at piles head (SC).

4.3.1. White-noise response

In this section, the evaluation of the period shifting and the damping ratio of the whole system (soil, pile and superstructure) is shown, with respect to the fixed base oscillator. Additionally, white-noise excitations were used for evaluating the influence of input motion amplitude on system response.

The transfer functions are computed, for the evaluation of the dynamic properties of the studied systems, referring to several records (Figure 4.42). Three transfer functions are considered for the evaluation of the following responses:

- *system response referred to the shaking table*: computed as the ratio between the FFT of the accelerogram at the top of the oscillator (A) and the FFT of the one at the shaking table (B);

- *system response referred to the free-field condition*: computed as the ratio between the FFT of the accelerogram at the top of the oscillator (A) and the FFT of the one at the soil surface (C);

- *oscillator response*: computed as the ratio between the FFT of the accelerogram at the top of the oscillator (A) and the FFT of the one at the bottom of the oscillator (D).

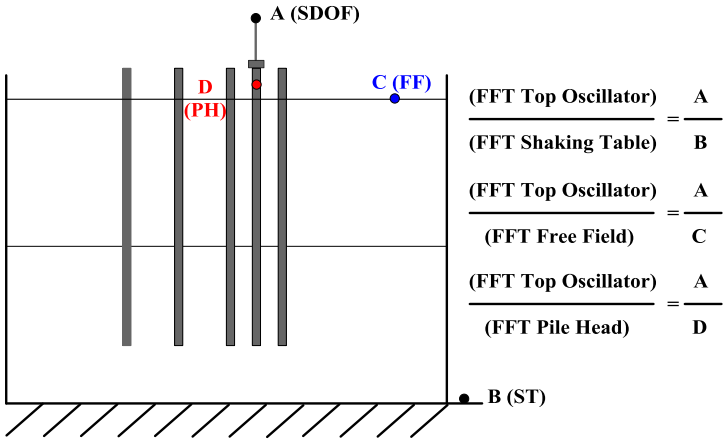

Figure 4.42. Accelerometers location

i) Free-head piles with oscillator

The response for the free-head pile configuration with the oscillator connected at the top of pile 5 is described in this section (Figure 4.43). The tests reported herein refer to the first phase of testing and six different masses for the oscillator, namely 75g, 125g, 175g, 275g, 475g and 975g. Two different inputs acceleration are used for the white-noise tests (0.02g and 0.08g).

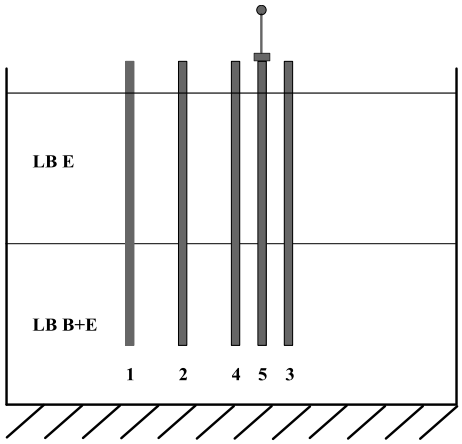

Figure 4.43. Free-head pile with oscillator configuration (FHP+SDOF)

Figure 4.44 shows all the transfer functions computed for the 0.02g white-noise tests for the reported masses. The larger amplification and the highest frequency value for each mass are obtained when the transfer function refers to the base oscillator. The interaction effect can be evaluated considering the transfer functions computed referring to the shaking table or free-field signal. Figure 4.44 shows that the frequency in these two cases is the same, whereas the amplification that occurs could be different. This difference is related to the piles effect that tends to increase the amplification.

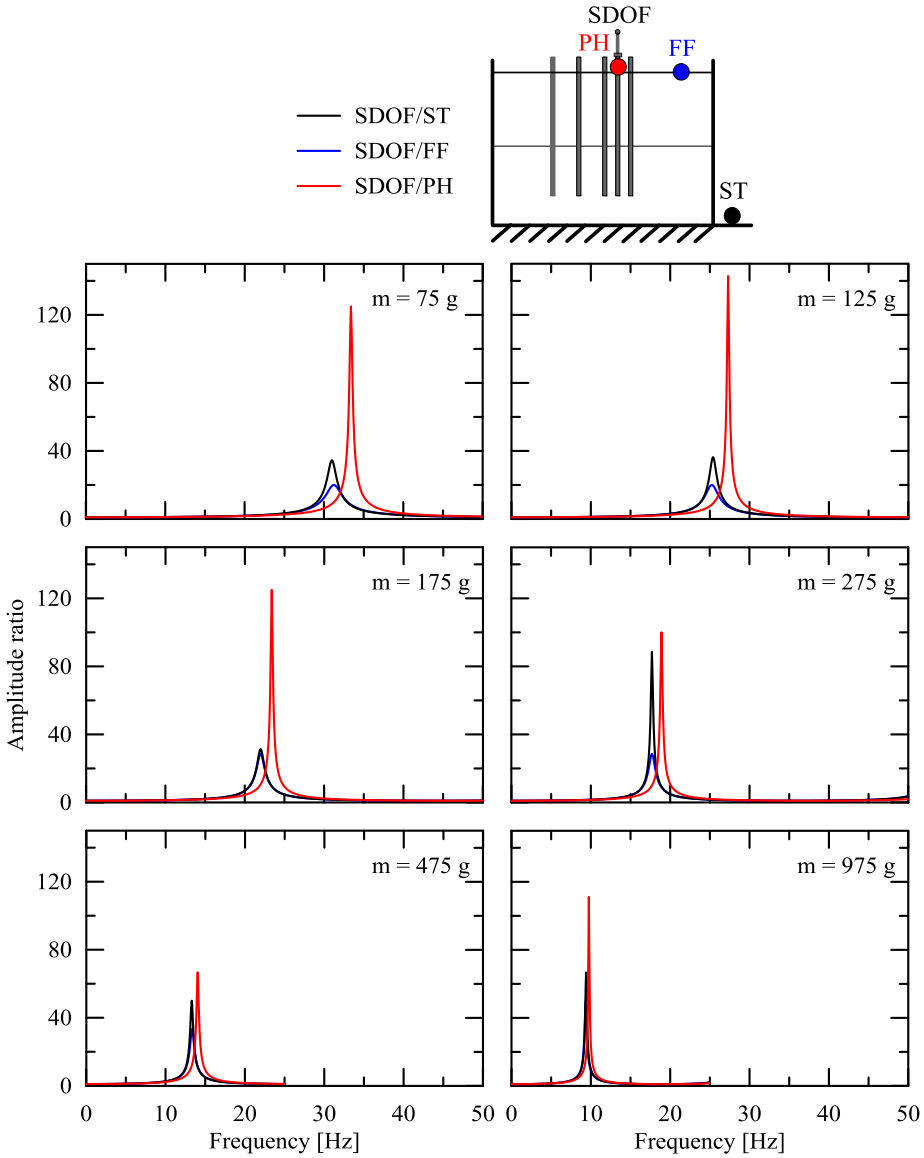

Figure 4.44. Transfer functions for all the oscillator masses for the 0.02g white noise test (FHP+SDOF configuration)

Figure 4.45 displays, in the same plot, the transfer functions of the masses considered for the input motion with maximum acceleration equal to 0.02g; the functions are computed with reference to the SDOF base (Figure 4.45a) and the free-field (Figure 4.45b). The experimental outcomes confirm that the frequency decreases as the mass increases.

Similar analyses are carried out for the white noise with the input acceleration equal to 0.08g (Figure 4.46). The response of the systems is similar to the one observed for the smaller input acceleration exception for the values reached.

In order to investigate the effects of seismic SPSI on SDOF response, the shifting of the SDOF fundamental frequencies (and periods) with respect to the SDOF fixed-base configuration has been evaluated. The values for the two white noise excitations and

different masses are summarized in Table 4.3. The maximum period elongation occurs on the oscillator with 75 grams mass excited with the higher input acceleration (0.08g), referring to the shaking table or free-field, as expected. These transfer functions involve all the contributions in the period elongation.

Table 4.4 shows the average and the standard deviation of the frequency and of the period elongation in percentage of each mass for the two different input amplitudes considered for the FHP+SDOF configuration.

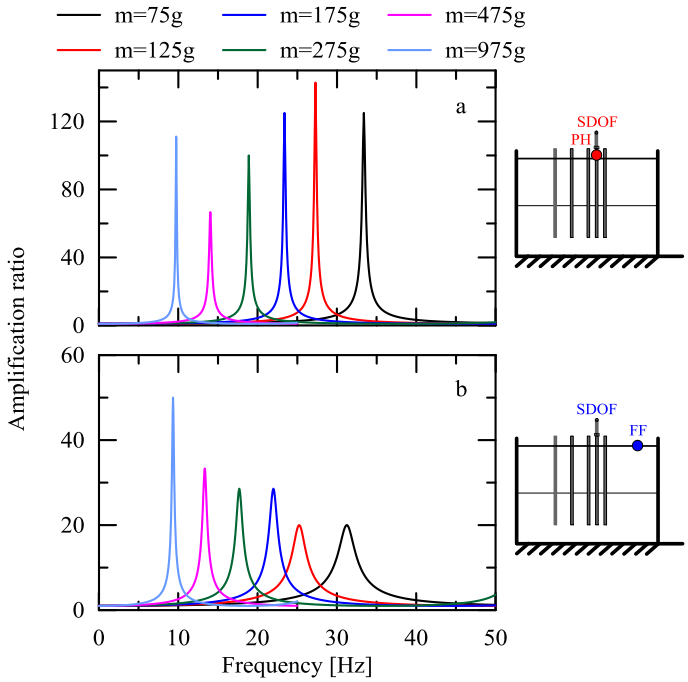

Figure 4.45. Transfer functions for all the oscillator masses for the 0.02g white noise test referred to SDOF base (a) and free-field (b) (FHP+SDOF configuration)

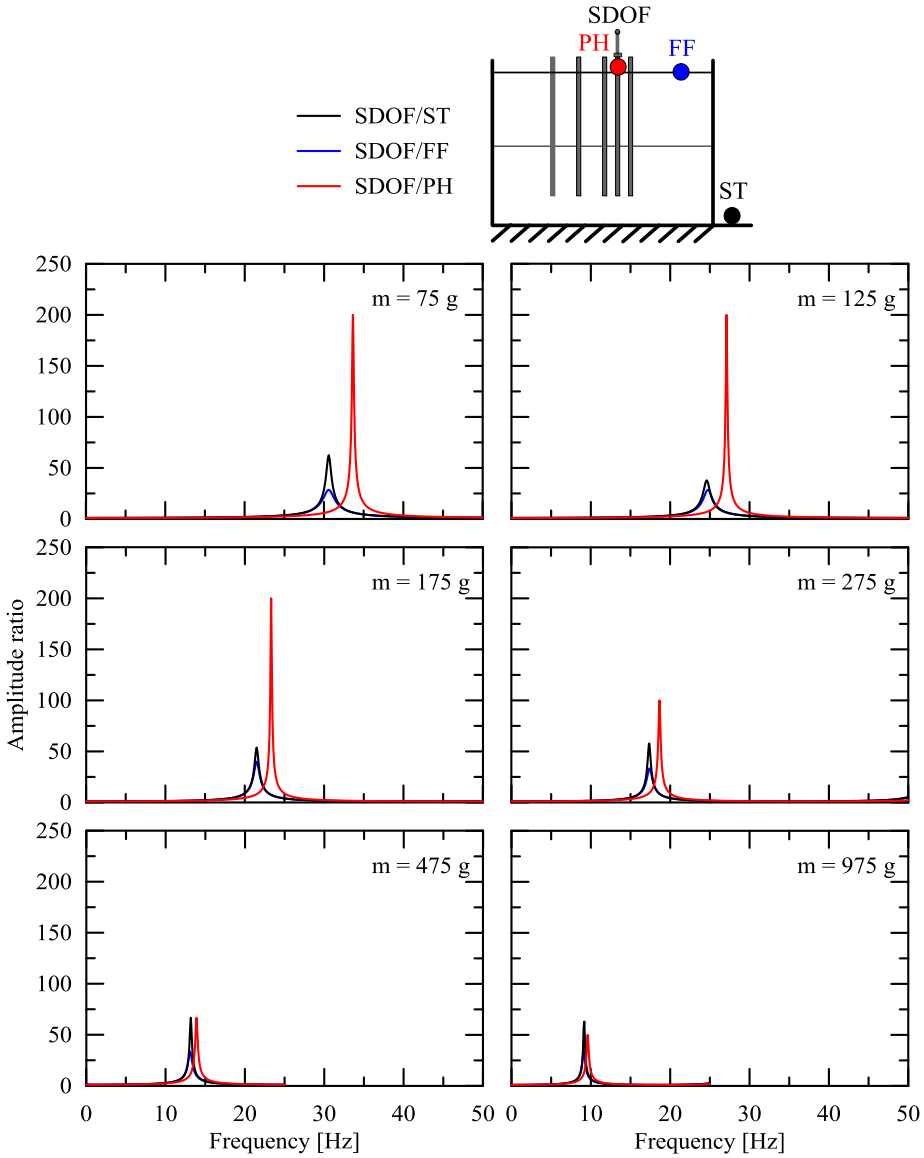

Figure 4.46. Transfer functions for all the oscillator masses for the 0.08g white noise test (FHP+SDOF configuration)

Table 4.3. Period shifting for the sample systems in the FHP+SDOF configuration

mass [grams]	transfer function	a_{input} ~ 0.02g				a_{input} ~ 0.08g			
		f [Hz]	T_{SSI} [s]	ΔT [%]	D [%]	f [Hz]	T_{SSI} [s]	ΔT [%]	D [%]
75	SDOF/S.T.	31.00	0.032	22.58	2.90	30.60	0.033	24.18	1.60
	SDOF/F.F.	31.25	0.032	21.60	5.00	30.60	0.033	24.18	3.50
	SDOF/P.H.	33.40	0.030	13.77	0.80	33.65	0.030	12.93	0.50
125	SDOF/S.T.	25.40	0.039	20.08	2.75	24.60	0.041	23.98	2.64
	SDOF/F.F.	25.25	0.040	20.79	5.00	24.75	0.040	23.23	3.50
	SDOF/P.H.	27.30	0.037	11.72	0.70	27.10	0.037	12.55	0.50

(continued on next page)

Table 4.3. Period shifting for the sample systems in the FHP+SDOF configuration (cont.)

mass [grams]	transfer function	a_{input} ~ 0.02g				a_{input} ~ 0.08g			
		f [Hz]	T_{SSI} [s]	ΔT [%]	D [%]	f [Hz]	T_{SSI} [s]	ΔT [%]	D [%]
175	SDOF/S.T.	22.00	0.045	20.45	3.18	21.50	0.047	23.26	1.86
	SDOF/F.F.	22.00	0.045	20.45	3.50	21.50	0.047	23.26	2.50
	SDOF/P.H.	23.40	0.043	13.25	0.80	23.33	0.043	13.59	0.50
275	SDOF/S.T.	17.70	0.056	15.82	1.13	17.35	0.058	18.16	1.73
	SDOF/F.F.	17.70	0.056	15.82	3.50	17.40	0.057	17.82	3.00
	SDOF/P.H.	18.90	0.053	8.47	1.00	18.65	0.054	9.92	1.00
475	SDOF/S.T.	13.30	0.075	12.78	2.00	13.18	0.076	13.81	1.50
	SDOF/F.F.	13.35	0.075	12.36	3.00	13.10	0.076	14.50	3.00
	SDOF/P.H.	14.05	0.071	6.76	1.50	13.90	0.072	7.91	1.50
975	SDOF/S.T.	9.40	0.106	10.64	1.50	9.15	0.109	13.66	1.50
	SDOF/F.F.	9.35	0.107	11.23	2.00	9.10	0.110	14.29	3.00
	SDOF/P.H.	9.75	0.103	6.67	0.90	9.60	0.104	8.33	2.00

Keys: S.T. shaking table; F.F. free-field; P.H. Pile head; $\Delta T=(T_{SSI}-T_{fix})/T_{fix}$

Table 4.4. Average and standard deviation of frequency and period elongation for the FHP+SDOF configuration

mass [grams]	transfer function	Frequency f_n [Hz]	σ	Period elongation ΔT_m [%]	σ
75	SDOF/S.T.	30.80	0.283	23.38	1.131
	SDOF/F.F.	30.93	0.460	22.89	1.824
	SDOF/P.H.	33.53	0.177	13.35	0.594
125	SDOF/S.T.	25.00	0.566	22.03	2.758
	SDOF/F.F.	25.00	0.354	22.01	1.725
	SDOF/P.H.	27.20	0.141	12.14	0.587
175	SDOF/S.T.	21.75	0.354	21.86	1.987
	SDOF/F.F.	21.75	0.354	21.86	1.987
	SDOF/P.H.	23.37	0.049	13.42	0.240

(continued on next page)

Table 4.4. Period shifting for the sample systems in the SC+SDOF configuration (cont.)

mass [grams]	transfer function	Frequency f_n [Hz]	σ	Period elongation ΔT_m [%]	σ
275	SDOF/S.T.	17.53	0.247	16.99	1.655
	SDOF/F.F.	17.55	0.2212	16.82	1.414
	SDOF/P.H.	18.78	0.177	9.20	1.025
475	SDOF/S.T.	13.24	0.085	13.30	0.728
	SDOF/F.F.	13.23	0.177	13.43	1.513
	SDOF/P.H.	13.98	0.106	7.34	0.813
975	SDOF/S.T.	9.28	0.177	12.15	2.135
	SDOF/F.F.	9.23	0.177	12.76	2.164
	SDOF/P.H.	9.68	0.106	7.50	1.174

Keys: S.T. shaking table; F.F. free-field; P.H. Pile head; $\Delta T=(T_{SSI}-T_{fix})/T_{fix}$

Figure 4.47 summarizes the results for the period elongation and the damping ratio for the two input accelerations referred to free-field. The results are expressed in terms of wave parameter ($\sigma = \frac{v_s}{f_{fix}h}$) that can be expressed as the ratio of the soil shear wave velocity V_s and the product of the fixed base frequency (f_{fix}) and the height of the oscillator (h). According to several authors (i.e. Ciampoli and Pinto, 1995; Kramer, 1996; Stewart el al., 1999a) this dimensionless parameter governs the SSI effects in seismic structural response. The increasing of the SSI effect with the inverse ratio of the wave parameter for both the input accelerations is clear. Figure 4.47a shows the data and the corresponding linear fitting, that indicates a linear dependency of the period elongation with 1/σ. In Figure 4.47b the variation in terms of damping ratio is shown, in this case the trend is not clear, for this reason it was decided to not use any fitting of data.

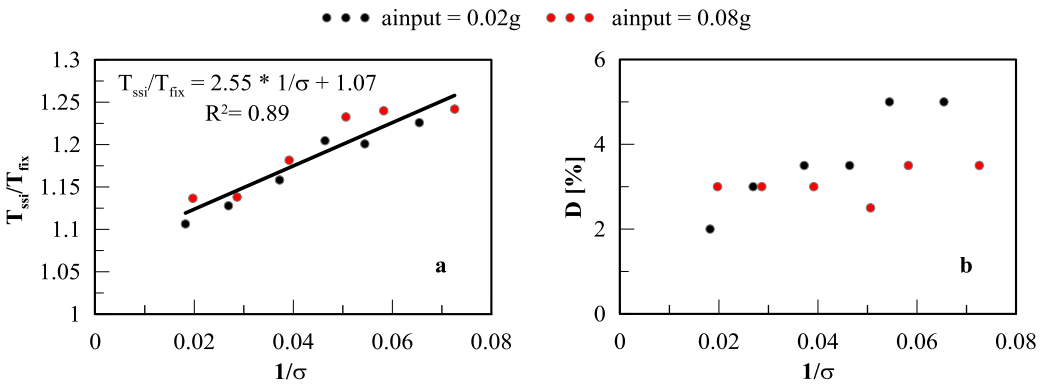

Figure 4.47. Period elongation (a) and damping ratio (b) for the FHP+SDOF configuration

ii) Short-cap connection with oscillator

The response of the oscillator placed on pile 5 for the short-cap configuration is examined hereafter (Figure 4.48). The results are relative to the first phase tests. Five different masses are used, namely 125g, 175g, 275g, 475g and 975g. Three different inputs acceleration are adopted for the white-noise tests (0.02g, 0.05g and 0.08g).

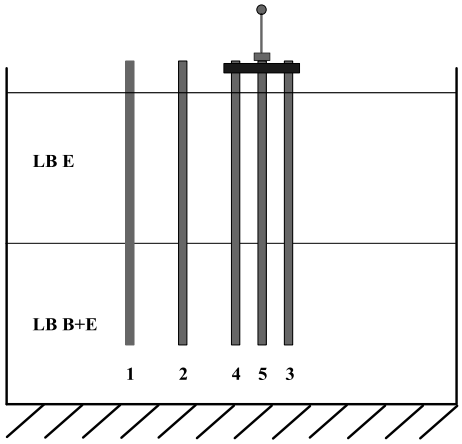

Figure 4.48. Short-cap connection with oscillator configuration (SC+SDOF)

Figure 4.49 shows the transfer functions computed for the 0.02g white-noise test for the considered masses. The connection at the pile heads changes the system response. The connection represents a strong restrain for both oscillator and piles, producing natural frequencies very close to the fixed ones.

Figure 4.50 displays in the same plot the transfer functions of the considered masses for the input motion with maximum acceleration equal to 0.02g, computed with reference to the SDOF base (Figure 4.50a) and the free-field (Figure 4.50b). The experimental outcomes confirm that the frequency decreases as the mass increases.

Similar analyses are carried out for the white-noise with the input accelerations equal to 0.05g (Figure 4.51) and 0.08g (Figure 4.52). The response of the system is similar to the one observed for the smaller input acceleration exception for the amplitude.

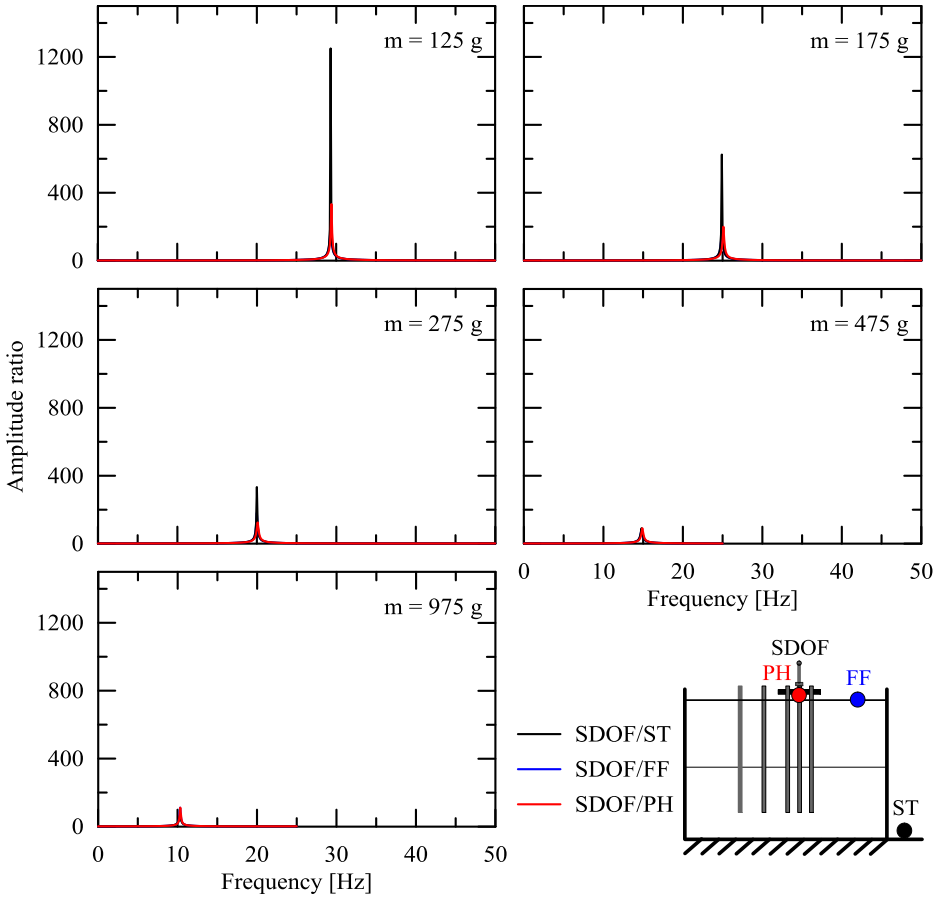

Figure 4.49. Transfer functions for all the oscillator masses for the 0.02g white noise test (SC+SDOF configuration)

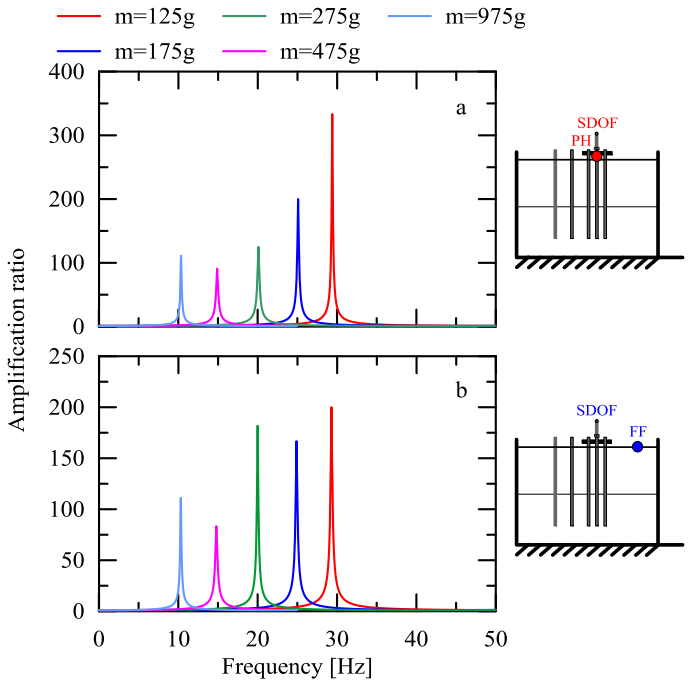

Figure 4.50. Transfer functions for all the oscillator masses for the 0.02g white noise test referred to SDOF base (a) and free-field (b) (SC+SDOF configuration)

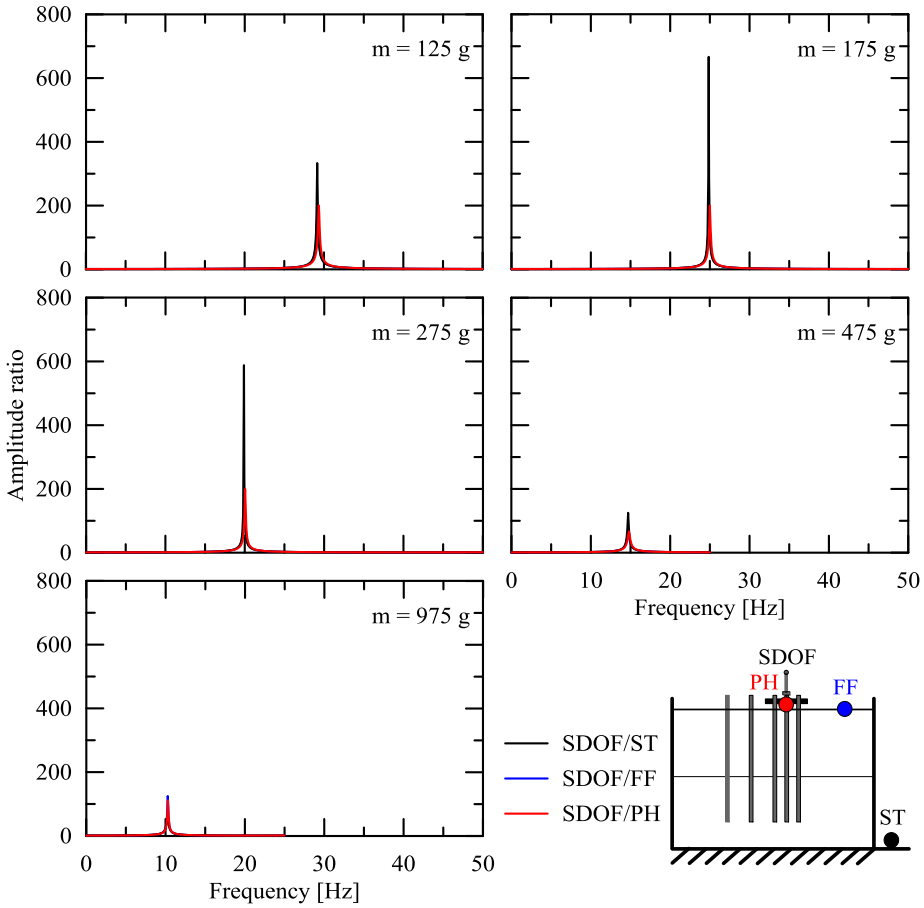

Figure 4.51. Transfer functions for all the oscillator masses for the 0.05g white noise test (SC+SDOF configuration)

In analogy with the FHP+SDOF configuration, the shifting of the SDOF fundamental frequencies (and periods) with respect to the SDOF fixed-base configuration has been evaluated. The values for the three white noise excitations and different masses are summarized in Table 4.5. The period elongation is almost negligible, due to the connection capability to reproduce base condition for the oscillators very close to the fixed ones. In this configuration the maximum elongation is obtained for the oscillator with 175g mass.

Table 4.6 shows the average and the standard deviation of the frequency and of the period elongation in percentage of each mass for the three different input amplitudes considered for the SC+SDOF configuration.

Figure 4.53 summarizes results for period elongation and damping ratio for the three input accelerations, expressed in terms of the wave parameter ($1/\sigma$). The effect of $1/\sigma$ on the period elongation is similar to that observed for the FHP+SDOF configuration. A linear fitting can be considered again satisfactory even if the scatter is higher then in the

previous case. In Figure 4.53b the damping ratio response is not related to the input acceleration and it is always very close by the fixed base values.

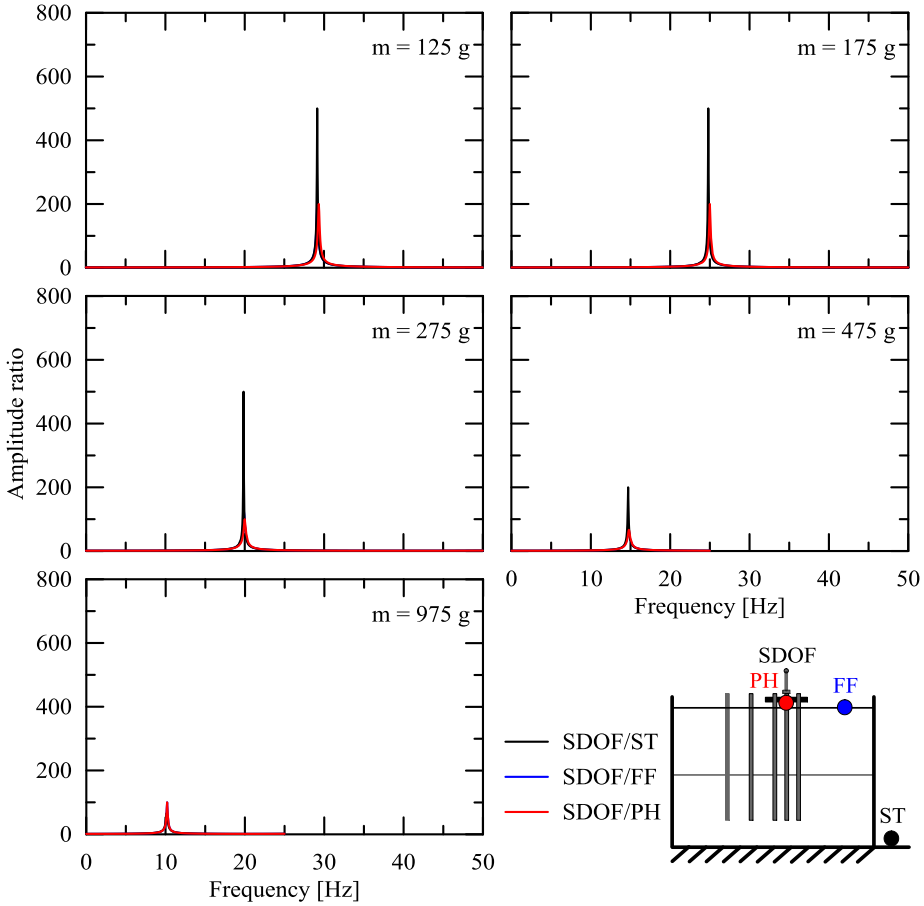

Figure 4.52. Transfer functions for all the oscillator masses for the 0.08g white noise test (SC+SDOF configuration)

Table 4.5. Period shifting for the sample systems in the SC+SDOF configuration

mass [grams]	transfer function	a_{input} ~ 0.02g				a_{input} ~ 0.05g				a_{input} ~ 0.08g			
		f [Hz]	T_{SSI} [s]	ΔT [%]	D [%]	f [Hz]	T_{SSI} [s]	ΔT [%]	D [%]	f [Hz]	T_{SSI} [s]	ΔT [%]	D [%]
125	SDOF/S.T.	29.30	0.034	4.10	0.08	29.15	0.034	4.63	0.30	29.15	0.034	4.63	0.20
	SDOF/F.F.	29.30	0.034	4.10	0.50	29.18	0.034	4.52	0.50	29.15	0.034	4.63	0.50
	SDOF/P.H.	29.40	0.034	3.74	0.30	29.35	0.034	3.92	0.50	29.35	0.034	3.92	0.50
175	SDOF/S.T.	24.90	0.040	6.43	0.16	24.85	0.040	6.64	0.15	24.80	0.040	6.85	0.20
	SDOF/F.F.	24.90	0.040	6.43	0.60	24.90	0.040	6.43	0.50	24.85	0.040	6.64	0.50
	SDOF/P.H.	25.10	0.040	5.58	0.50	25.00	0.040	6.00	0.50	25.00	0.040	6.00	0.50
275	SDOF/S.T.	20.00	0.050	2.50	0.30	19.90	0.050	3.02	0.17	19.85	0.050	3.27	0.20
	SDOF/F.F.	20.00	0.050	2.50	0.55	19.95	0.050	2.76	0.50	19.90	0.050	3.02	0.80
	SDOF/P.H.	20.10	0.050	1.99	0.80	20.05	0.050	2.24	0.50	20.00	0.050	2.50	1.00
475	SDOF/S.T.	14.80	0.068	1.35	1.10	14.70	0.068	2.04	0.80	14.70	0.068	2.04	0.50
	SDOF/F.F.	14.80	0.068	1.35	1.20	14.70	0.068	2.04	1.50	14.75	0.068	1.69	1.50
	SDOF/P.H.	14.90	0.067	0.67	1.10	14.80	0.068	1.35	1.50	14.80	0.068	1.35	1.50
975	SDOF/S.T.	10.30	0.097	0.97	1.50	10.25	0.098	1.46	1.50	10.15	0.099	2.46	1.50
	SDOF/F.F.	10.32	0.097	0.78	0.90	10.28	0.097	1.17	0.80	10.20	0.098	1.96	1.00
	SDOF/P.H.	10.35	0.097	0.48	0.90	10.30	0.097	0.97	0.90	10.20	0.098	1.96	1.00

Keys: S.T. shaking table; F.F. free-field; P.H. Pile head; $\Delta T=(T_{SSI}-T_{fix})/T_{fix}$

Table 4.6. Average and standard deviation of frequency and period elongation for the SC+SDOF configuration

mass [grams]	transfer function	Frequency f_n [Hz]	σ	Period elongation ΔT_m [%]	σ
75	SDOF/S.T.	29.20	0.087	4.45	0.306
	SDOF/F.F.	29.21	0.079	4.42	0.280
	SDOF/P.H.	29.37	0.029	3.86	0.104
125	SDOF/S.T.	24.85	0.050	6.64	0.210
	SDOF/F.F.	24.88	0.029	6.50	0.121
	SDOF/P.H.	25.03	0.058	5.86	0.242
175	SDOF/S.T.	19.92	0.076	2.93	0.393
	SDOF/F.F.	19.95	0.050	2.76	0.260
	SDOF/P.H.	20.05	0.050	2.24	0.255
275	SDOF/S.T.	14.73	0.058	1.81	0.398
	SDOF/F.F.	14.75	0.050	1.69	0.345
	SDOF/P.H.	14.83	0.058	1.12	0.393
475	SDOF/S.T.	10.23	0.076	1.63	0.759
	SDOF/F.F.	10.27	0.061	1.30	0.601
	SDOF/P.H.	10.28	0.076	1.14	0.754
975	SDOF/S.T.	29.20	0.087	4.45	0.306
	SDOF/F.F.	29.21	0.079	4.42	0.280
	SDOF/P.H.	29.37	0.029	3.86	0.104

Keys: S.T. shaking table; F.F. free-field; P.H. Pile head; $\Delta T=(T_{SSI}-T_{fix})/T_{fix}$

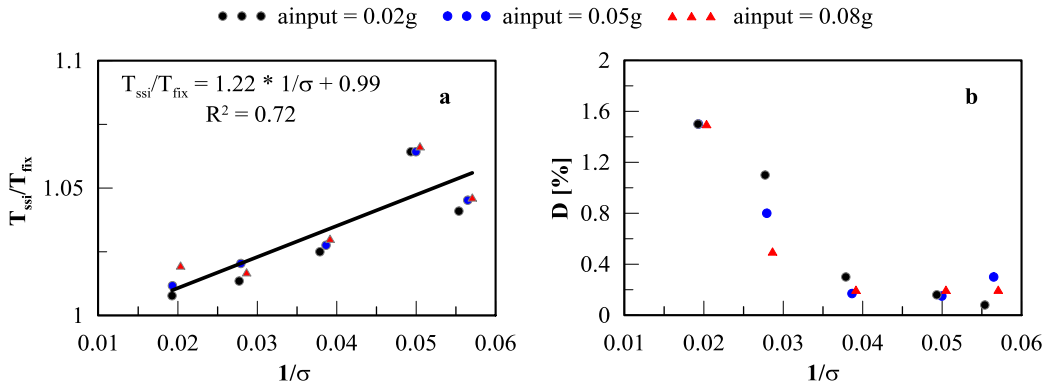

Figure 4.53. Period elongation (a) and damping ratio (b) for the SC+SDOF configuration with respect to free-field

iii) Configuration effect

The effect of the configuration is considered referring to the input accelerations available for both the configurations (0.02g and 0.08g). Referring to the oscillator with the maximum period elongation in the SC+SDOF configuration (m=175g), Figure 4.54 shows the transfer functions computed with reference to the SDOF base (Figure 4.54a) and the free-field (Figure 4.54b) for the white noise with 0.02g input acceleration. The SC+SDOF configuration gives a very low elongation (around 6%), while in the FHP+SDOF configuration it reaches the 20% considering the complete soil-pile-structure interaction (referring to the free-field signal).

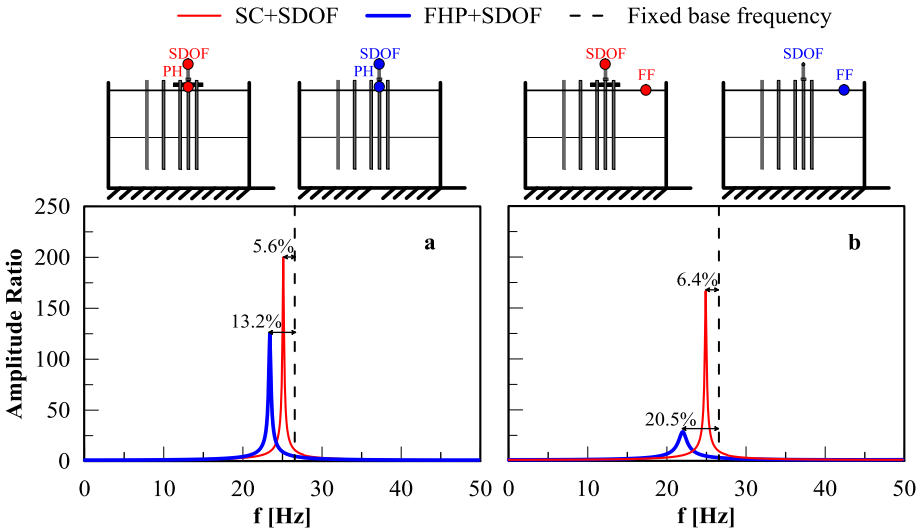

Figure 4.54. Comparison of transfer functions for FHP+SDOF and SC+SDOF configurations (m=175g), with respect to the SDOF base (a) and free-field (b) for input acceleration equal to 0.02g

Figure 4.55 shows the transfer functions (with reference to the SDOF base (Figure 4.55a) and the free-field (Figure 4.55b)) for the two pile configurations (SC+SDOF and FHP+SDOF) with mass oscillator equal to 175g, for white noise test with 0.08g input acceleration. The period elongation for the soil-pile-structure interaction in SC+SDOF configuration is not significantly affected by input acceleration (3%), contrary to what observed in the FHP+SDOF configuration (12%). Another effect of the input acceleration is the increasing in the amplification, especially for the FHP+SDOF configuration when evaluated with reference to the SDOF base.

Referring to the results relative to 0.02g input acceleration, Figure 4.56 shows the comparison between the two configurations in terms of the natural frequencies (top) and the damping ratios (bottom) for all the oscillators. The results shown refer to both the SDOF base (left hand-side) and the free-field (right hand side). The effect of the configuration is clear not only in terms of period elongation but also of damping ratio.

Figure 4.56 shows that for a particular value of 1/σ (corresponding to m=175g) occurs the maximum elongation. This aspect can be related to the double resonance effect that occurs in the system when the elongated period and the soil have a similar value. Similar shapes can be observed in the damping response, but the maximum values depend on the configuration and the system considered (referred to SDOF base or free-field).

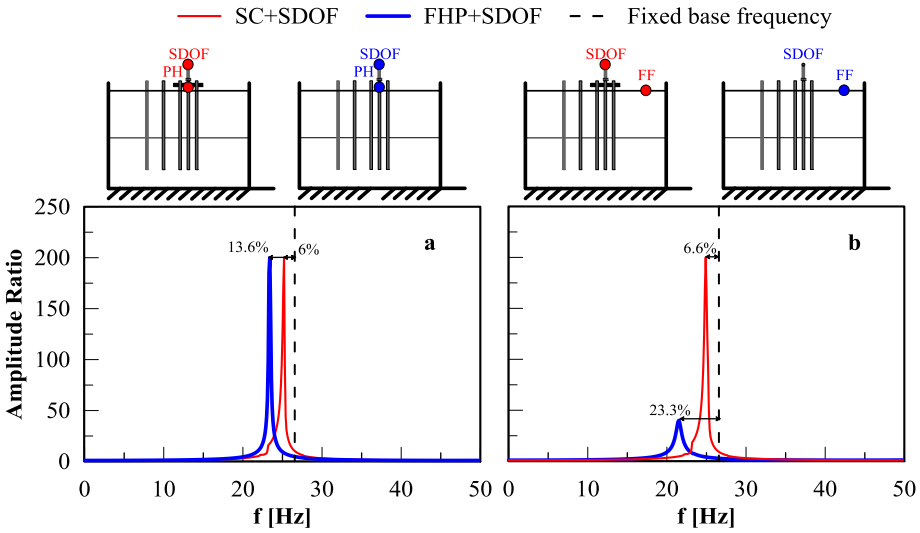

Figure 4.55. Comparison of transfer functions for FHP+SDOF and SC+SDOF configurations (m=175g), with respect to the SDOF base (a) and free-field (b) for input acceleration equal to 0.08g

Similar results are obtained for the 0.08g white noise test (Figure 4.57). As observed previously, the input acceleration changes the amplification in the system. Additionally, the increasing in acceleration generates a decreasing in the damping ratio and an increasing of the period elongation.

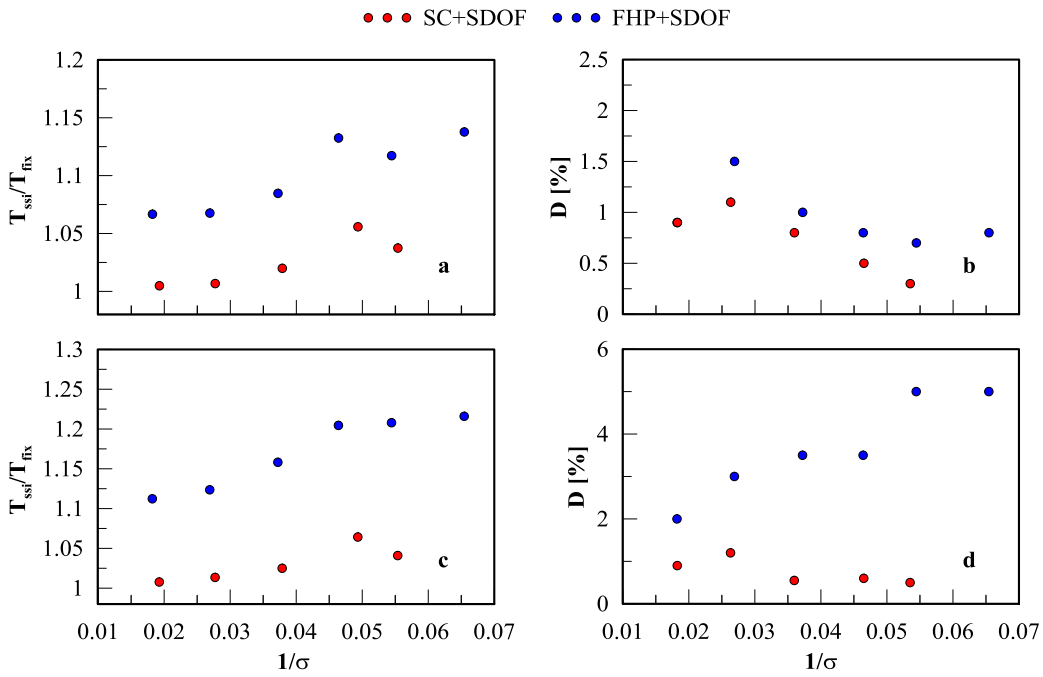

Figure 4.56. Period elongation (a,c) and damping ratio (b,d) for FHP+SDOF and SC+SDOF configurations, with respect to the SDOF base (a,b) and free-field (c,d) for 0.02g input motion

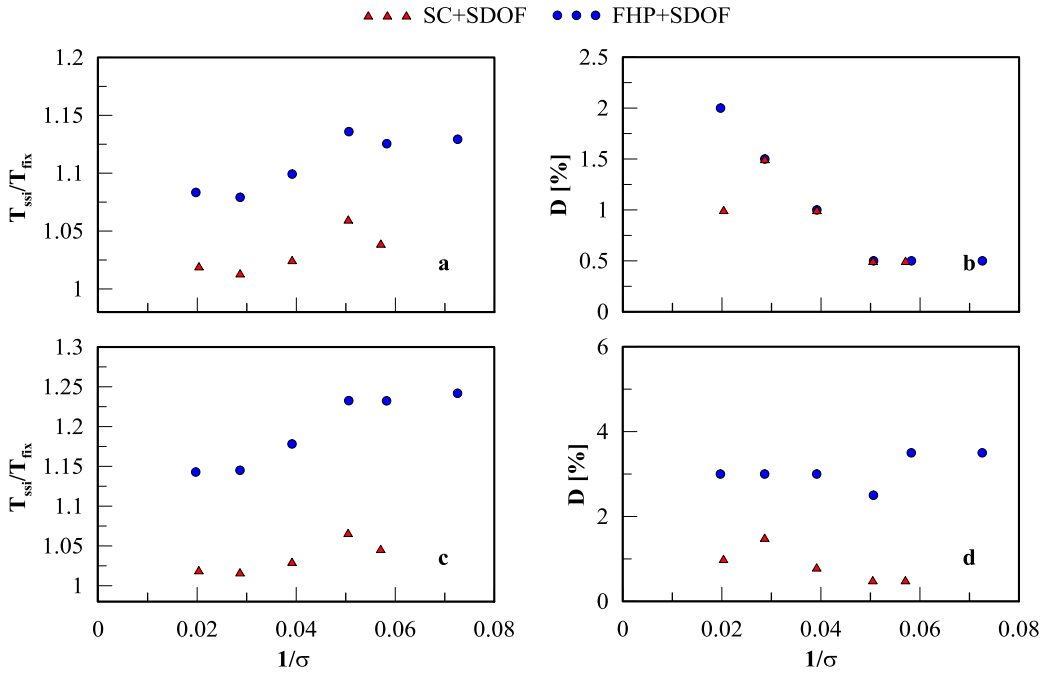

Figure 4.57. Period elongation (a,c) and damping ratio (b,d) for FHP+SDOF and SC+SDOF configurations, with respect to the SDOF base (a,b) and free-field (c,d) for 0.08g input motion

4.3.2. Harmonic response

The effect of the period elongation on the response of the pile in the FHP+SDOF (Figure 4.43) and SC+SDOF configurations (Figure 4.48) are presented in this section with reference to the harmonic input motion. Presented results refer to the harmonic input with frequency of 20 Hz and amplitude at the shaking table equal to 0.1g.

i) Free-head piles with oscillator

In Figure 4.58a the response of the soil considering different SDOF masses are compared in terms of absolute maximum acceleration versus depth in the free-field condition. In these tests, the response of the soil does not vary, i.e. the kinematic component does not vary and the variations of the response along the piles are simply related to the inertial effects due to the masses.

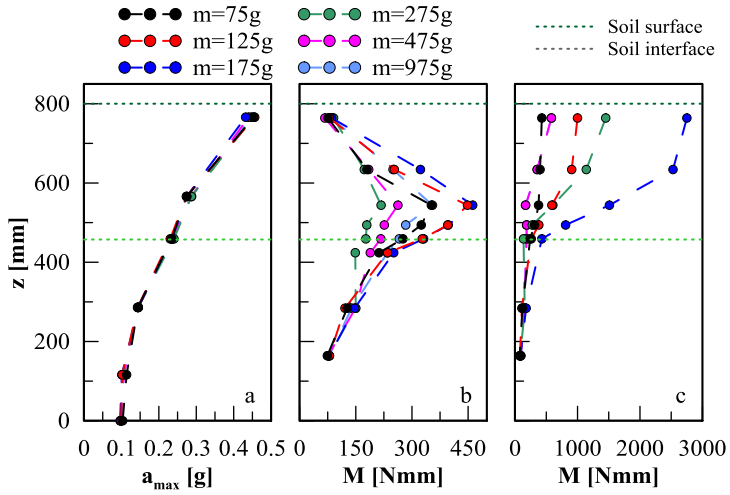

Figure 4.58. Envelope of free-field accelerations (a) and bending moments along piles 4 (b) and 5 (c) for FHP+SDOF configuration (input: f=20 Hz, a=0.1g)

Using the strain-gauges records for both piles 4 and 5 the bending moments are computed and reported in Figure 4.58b and 4.58c respectively in terms of absolute maximum along depth. The inertial effects are significant at the pile head up to a depth that is a function of the mass value. It can be useful to consider the dynamic response of the system. The increasing of the maximum bending moment at the pile head (M_{PH}) is related to the resonance condition. This statement is confirmed by Figure 4.59, in which M_{PH} is plotted versus the ratio between the input fundamental frequency and the frequency of the system. The resonance condition are checked for the two different system frequencies: the first one, quoted as structural frequency (f_{stru}), which refers to the frequency of the oscillator, is obtained from the transfer function between the top of the oscillator and its base (the head of the pile); the second frequency summarizes the soil-structure-interaction and it is obtained from the transfer function between the top of the oscillator and the free-field (f_{SSI}).

Figure 4.59 shows that the maximum bending moment at the pile head (obtained for the mass of 175g) corresponds f_{stru} = 22.2 Hz and f_{SSI} = 18.6 Hz. Considering the input frequency (20 Hz), it is possible to verify the resonance conditions for all the masses. Results in Figure 4.59 confirm the relationship between the pile head response and the

resonance. The increasing of the maximum bending moment at the pile head is not a function of the SDOF mass, in fact the minimum occurs for the mass farthest to the resonance (m=975g, $f_{input}/f_{system} \approx 2$).

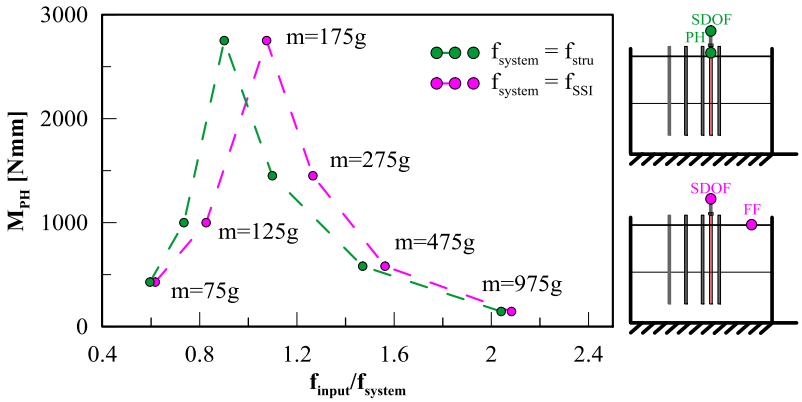

Figure 4.59. Maximum bending moment at pile head versus resonance condition for FHP+SDOF configuration for pile 5

Figure 4.58b shows the envelope of the absolute bending moments along piles 4. The experimental results show that the maximum is dependent on the resonance condition of oscillator connected to the close pile, indeed the maximum along the pile 4 occurs in the test with the oscillator mass of 175g. Another experimental result is the location of the maximum of bending moment along pile 4 in this configuration. The bending moment in this configuration is not found at the interface between the two layers (as in the kinematic interaction) but it is always located at lower depth (Figure 4.58b). In the free-head pile configuration the location of the maximum bending moment is always very close to the layer interface (§4.2.1.1). This behaviour is shown in Figure 4.60, where the comparison of the envelope of bending moments along pile 4 between the free-head pile without the oscillator (FHP) (loaded by frequency of 20 Hz and a_{max}=0.09g) and the free-head pile with SDOF on pile 5 considered in this paragraph (loaded by frequency of 20 Hz and amax=0.10g) is provided. The corrrespondance of the input motion in the two tests confirms that the different location of the maximum bending moment is related to the interaction between piles 4 and 5 also if not connected.

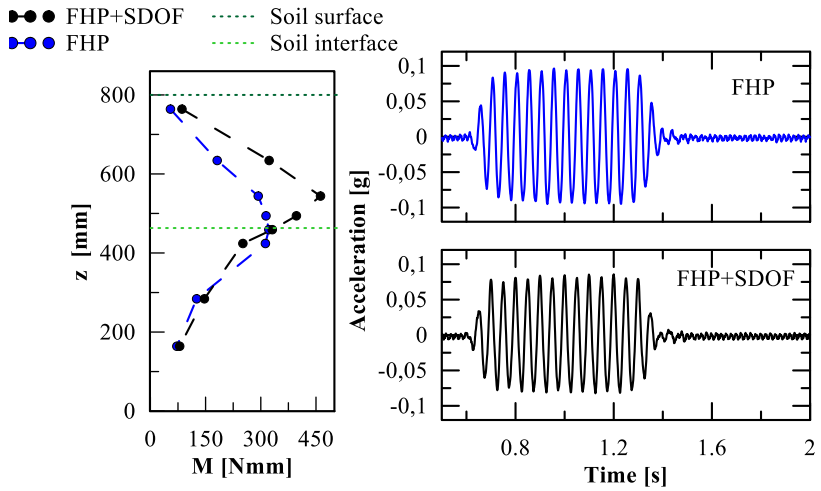

Figure 4.60. Envelope of absolute bending moment along pile 4 (input: f=20 Hz, a=0.01g)

ii) Short-cap connection with oscillator

In this section the results of the short-cap connection with oscillator are reported. The input is the same of the previous section (f=20 Hz and a=0.1g). All masses considered in the previous paragraph are analysed here, with the exception of the 75g mass that is not present in this configuration. The free-field responses in all the tests are always coincident (Figure 4.61a). Pile responses (Figure 4.61b and 4.61c) show that at pile heads the maximum bending moments are almost the same in the tests, due to the connection. The envelopes of absolute bending moment show a different shape along both pile 4 and 5 for the test with the mass oscillator equal to 275g. The different response is related to the resonance conditions. In this configuration (SC+SDOF) the resonance occurs for a higher mass respect to the FHP+SDOF configuration. The 275g mass oscillator is characterized by f_{fix} = 20.4 Hz, f_{stru} = 19.6 Hz and f_{SSI} = 19.4 Hz, that generates a soil-pile-structure interaction very low (about 5%), in agreement with the white-noise results.

The maxima bending moments at the piles 4 (Figure 4.62a) and 5 (Figure 4.62b) heads for the different masses respect to the resonance conditions are reported in Figure 4.62. The increasing of bending moment at pile heads observed in resonance condition in the FHP+SDOF configuration (Figure 4.59) is also present in this configuration even if it is less impressive.

In the SC+SDOF configuration the axial force acting on piles 4 and 5 has also been computed. Starting from the strain-gauges records the axial forces are computed using the method described in §3.2.6. In Figure 4.63 the axial force (N) at the pile heads are reported referring to the resonance conditions. The combination of presence of the oscillator and the connection among piles generates different responses in terms of axial

force at pile heads. The pile 4 response (the lateral one) is subjected to a significant higher axial force due to the rocking effect induced by the oscillator. On the contrary, at pile 5 head, the axial force is not far from the theoretical one computed taking into account the static contribution given by the weight of the oscillator (reported also in Figure 4.63). Nevertheless, the effect of the resonance affects also the response in terms of axial force, increased for both piles.

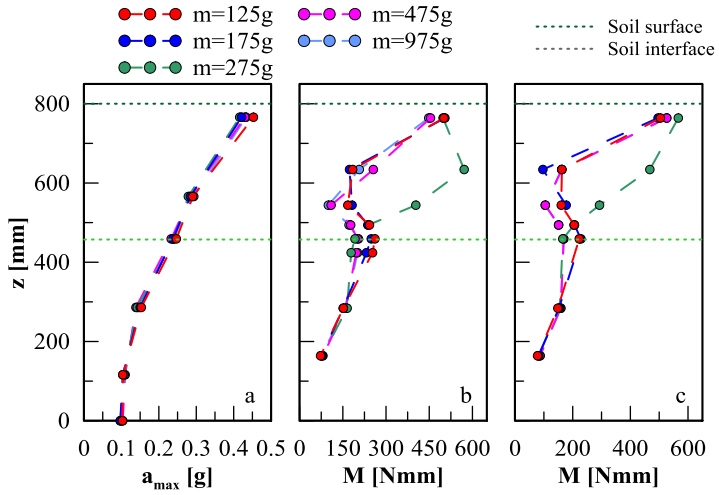

Figure 4.61. Envelope of free-field accelerations (a) and bending moments along piles 4 (b) and 5 (c) for SC+SDOF configuration (input: f=20 Hz, a = 0.1g)

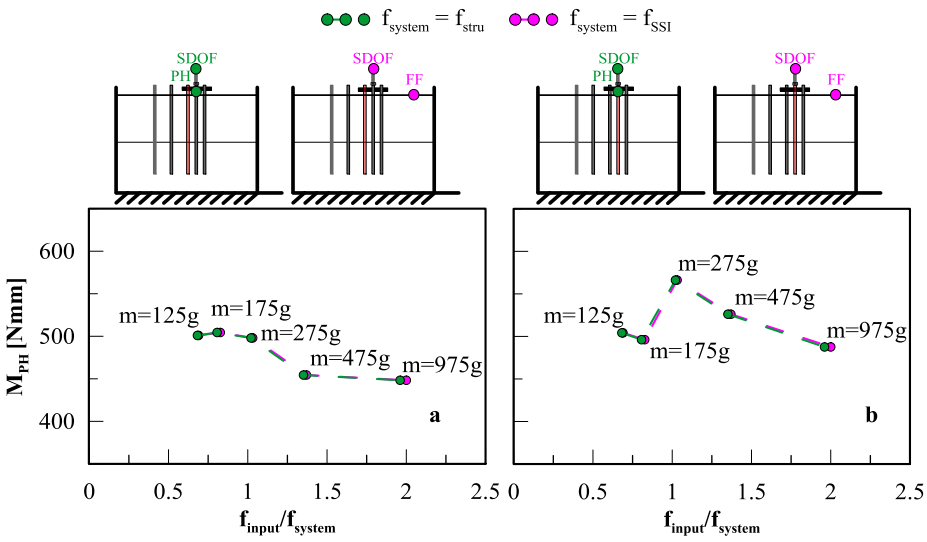

Figure 4.62. Maximum bending moment at pile head versus resonance condition for SC+SDOF configuration for pile 4 (a) and pile 5 (b)

The effect of the resonance in this configuration has been investigated analysing different input frequencies, to be sure that it is representative of an actual behaviour. Figures 4.64 and 4.65 show the envelopes of the absolute maximum soil accelerations and bending moments along piles 4 and 5 for other tests. The different shapes in the

bending moment envelopes are generated by the resonance conditions, as summarised in Figure 4.66.

The axial forces acting at the pile 4 and 5 heads are shown in Figure 4.67. The rocking effect is evident in all tests.

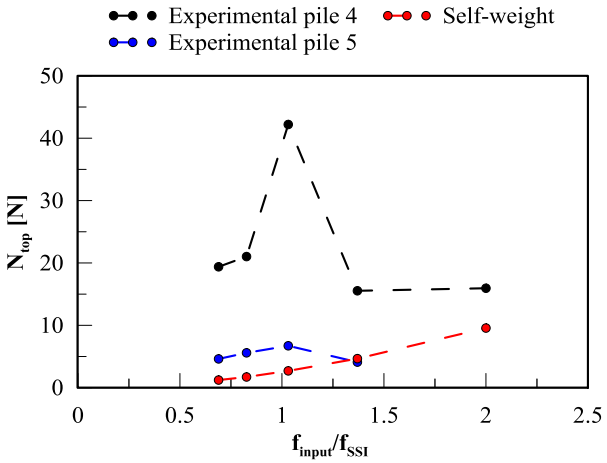

Figure 4.63. Axial force at the pile heads for SC+SDOF configuration (f=20 Hz, a=0.1g)

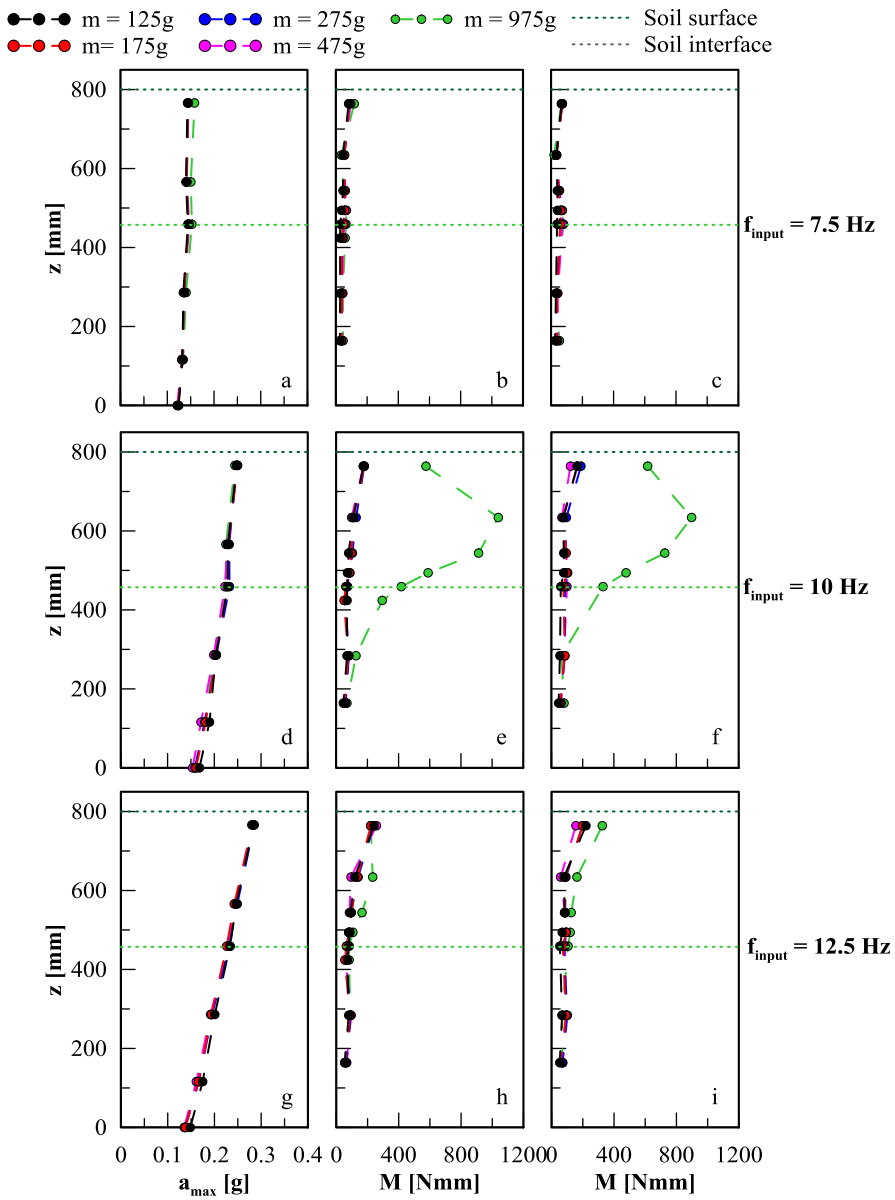

Figure 4.64. Envelope of absolute soil acceleration (a,d,g) and bending moments along pile 4 (b,e,h) and 5 (c,f,i) for all the tests reported (SC+SDOF configuration)

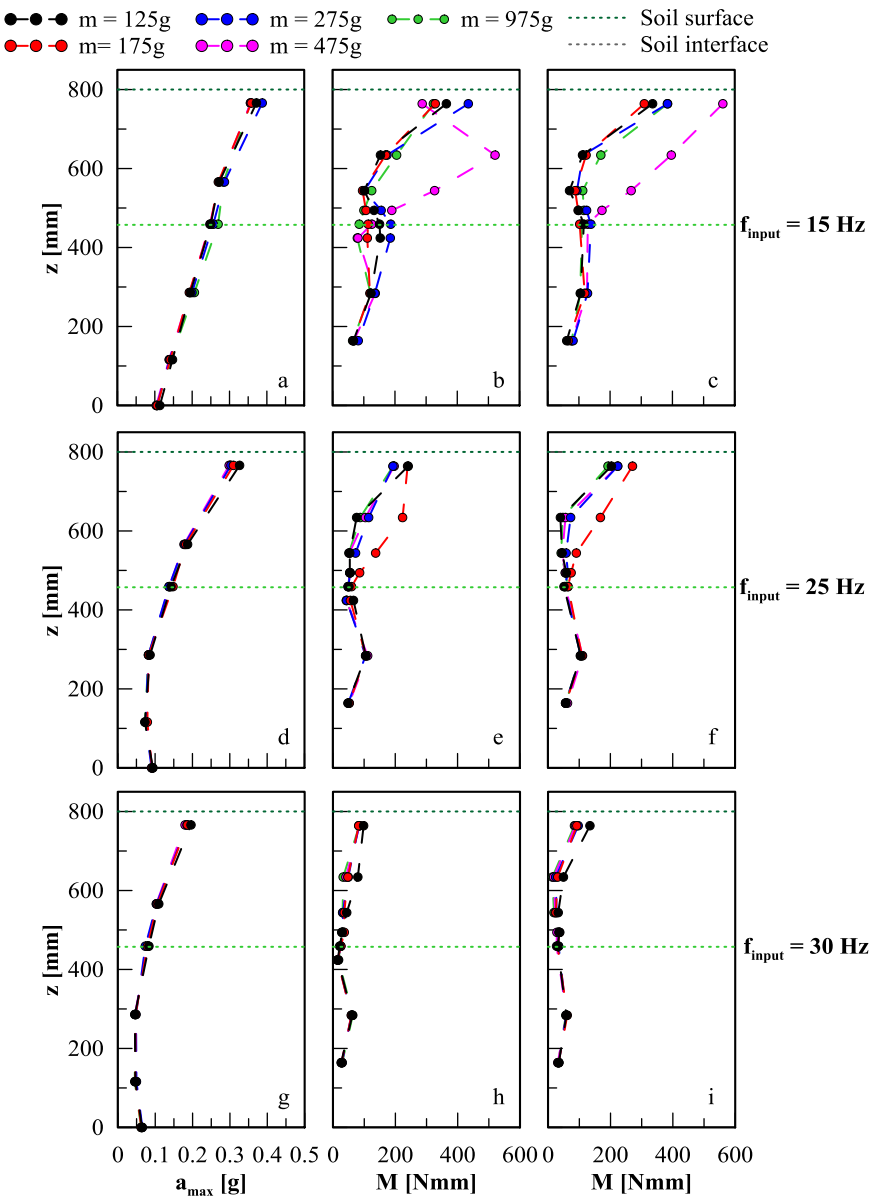

Figure 4.65. Envelope of absolute soil acceleration (a,d,g) and bending moments along pile 4 (b,e,h) and 5 (c,f,i) for all the tests reported (SC+SDOF configuration)

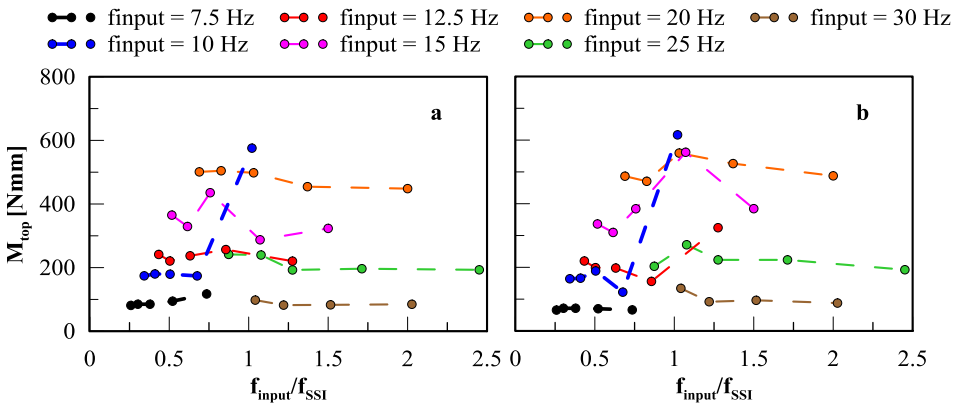

Figure 4.66. Resonance condition for SC+SDOF configuration

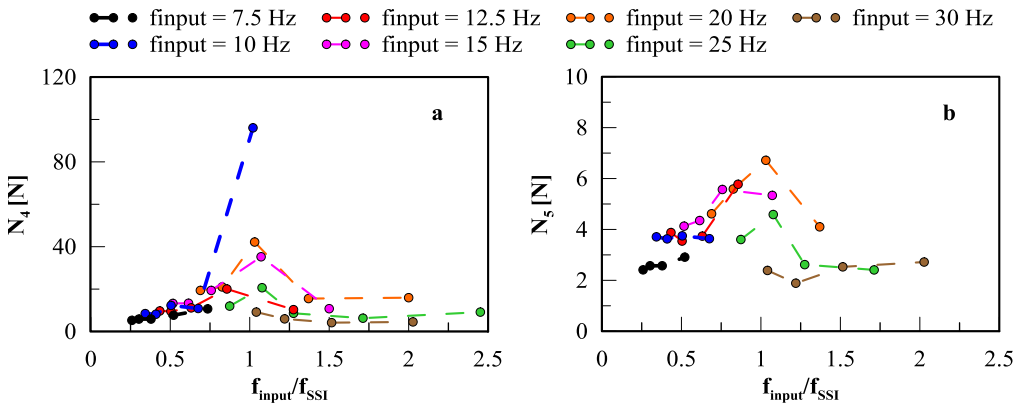

Figure 4.67. Axial force for SC+SDOF configuration

iii) Configuration effect

The effect of the configuration on the piles response has been already shown in §4.2.1.3, thus, in this paragraph, the comparison is shown only for the two masses in resonance with the system, namely 175g (for the FHP+SDOF configuration) and 275g (for the SC+SDOF configuration). The input is a sinusoidal wave with 20 Hz frequency and 0.1g input acceleration.

Figure 4.68 shows the comparisons for the oscillator with mass of 175g between the two configurations in terms of absolute maximum soil acceleration in the free-field condition along depth (Figure 4.68a) and the envelope of absolute bending moments along piles 4 (Figure 4.68b) and 5 (Figure 4.68c). The soil response in the tests is similar. The maximum bending moment at the pile 5 head occurs for the FHP+SDOF configuration (Figure 4.68c), because there is not a redistribution of the inertial effects. At the soil interface the bending moment is larger in the FHP+SDOF configuration, but this is due to the reduction of the kinematic bending moment in the SC+SDOF configuration. The pile connection tends to change the curvature in the piles (Figure 4.69) with a consequent reduction in the bending moments at the interface, as already observed in §4.2.1.3. The response of pile 4 presents almost zero bending moments at the top and the bottom for the FHP+SDOF configuration (the oscillator is not connected to this pile). In the SC+SDOF configuration the maximum bending moment is at the pile head, due to the connection and it is almost zero at the bottom. The bending moment reduction at the soil interface due to the head connection is evident also in pile 4. The piles responses are not affected by the configuration below the soil layer interface.

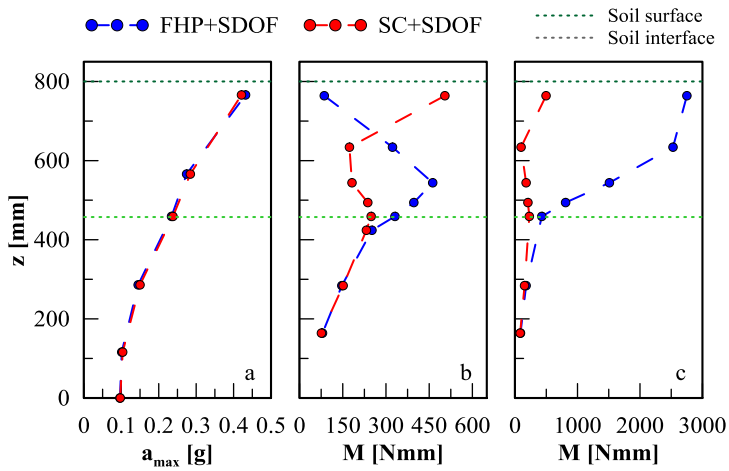

Figure 4.68. Envelope of free-field accelerations (a) and bending moments along piles 4 (b) and 5 (c) for FHP+SDOF and SC+SDOF configurations (m=175g, input: f=20 Hz, a = 0.1g)

Figure 4.69 shows the instantaneous profiles of the soil acceleration (Figure 4.69a) and bending moments along piles 4 (Figure 4.69b) and 5 (Figure 6.69c). The instants chosen for these profiles correspond to the instant in which the bending moment at pile 5 head is maximum and after half cycle. The location of the maximum bending moment at pile 4 for FHP+SDOF configuration is in an upper position respect to the SC+SDOF one.

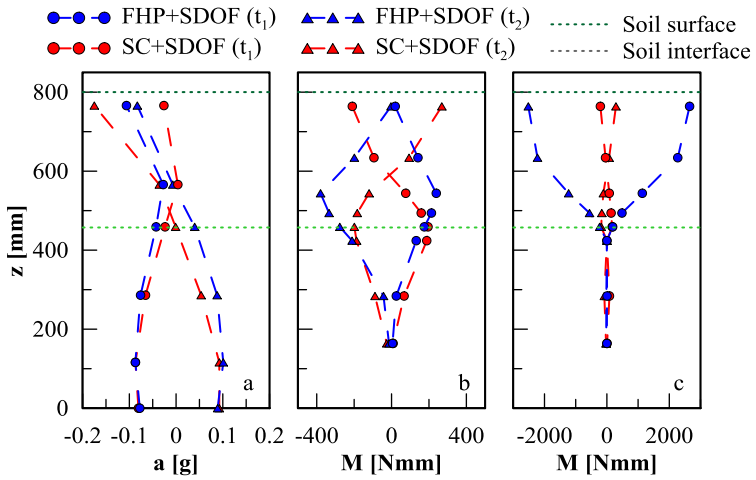

Figure 4.69. Instantaneous responses for soil column (a), pile 4 (b) and pile 5 (c) for short-cap (red) and free head pile (blue) configurations

The effect of the configuration can be similarly observed for the oscillator mass that goes in resonance in the SC+SDOF configuration (Figure 4.70). The free-field response (Figure 4.70a) can be considered the same in the two tests also in this case. Pile 4 (Figure 4.70b) and pile 5 (Figure 4.70c) have the same behaviour driven by the head condition.

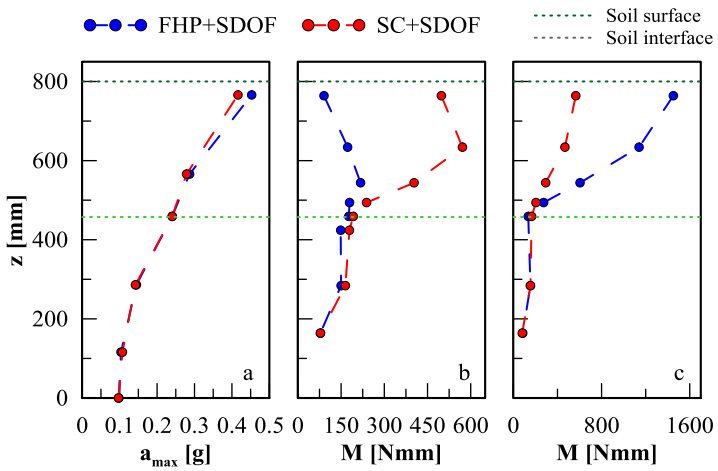

Figure 4.70. Envelope of free-field accelerations (a) and bending moments along piles 4 (b) and 5 (c) for FHP+SDOF and SC+SDOF configurations (m=275g, input: f=20 Hz, a = 0.1g)

The connection in the SC+SDOF configuration generates a lower bending moment at the pile heads compared to the ones generate by the FHP configuration, but it distributes the inertial effect at higher depth. This statement is evident comparing Figure 4.71 against Figure 4.72. In these figures the time histories of the bending moments along piles for SC+SDOF and FHP+SDOF configuration respectively are reported. Figure 4.71 shows also that the connection is able to transfer the inertial effect also to pile 4 (the oscillator is located at pile 5 head).

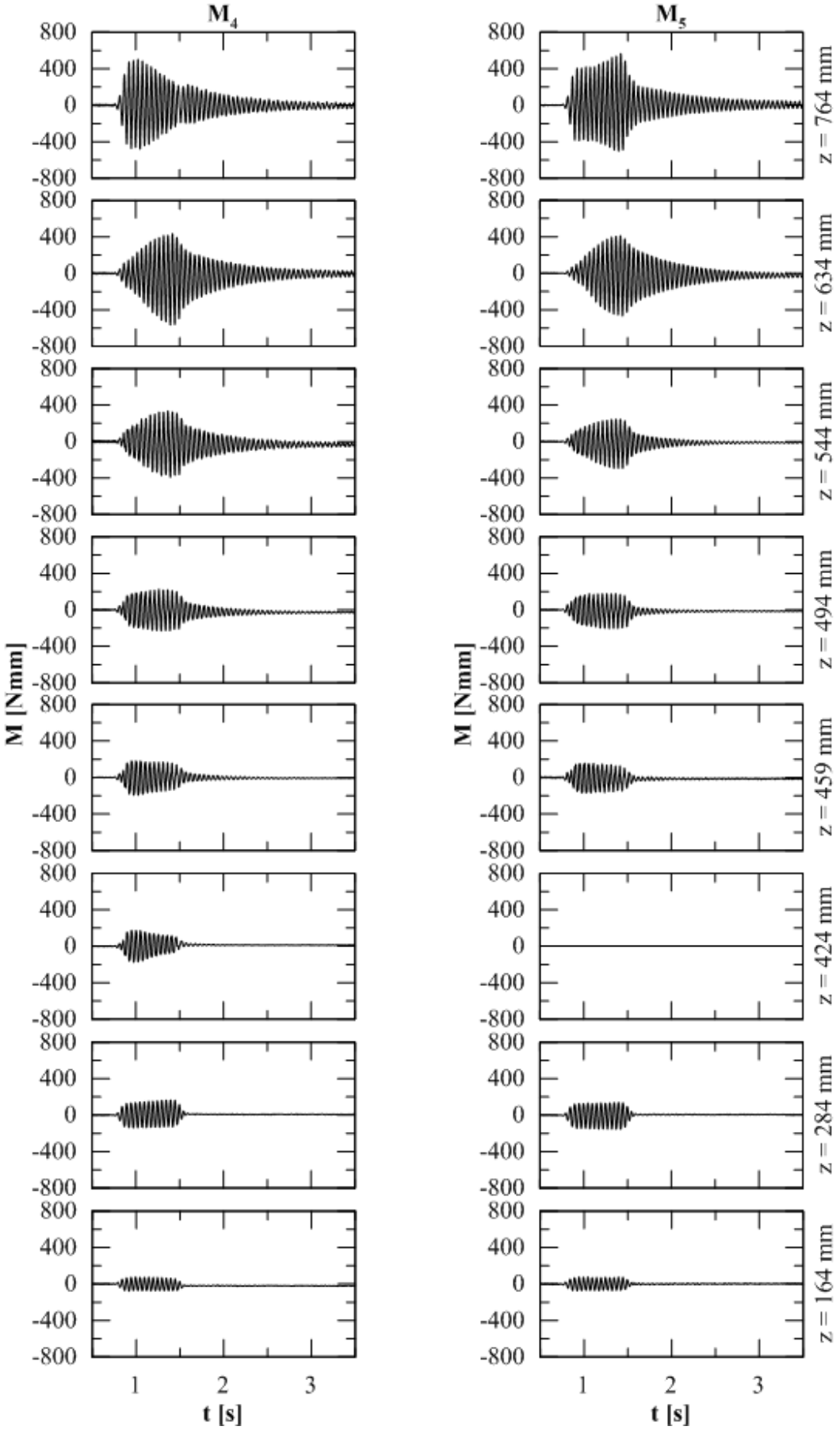

Figure 4.71. Time histories of bending moments at each depth for SC+SDOF configuration

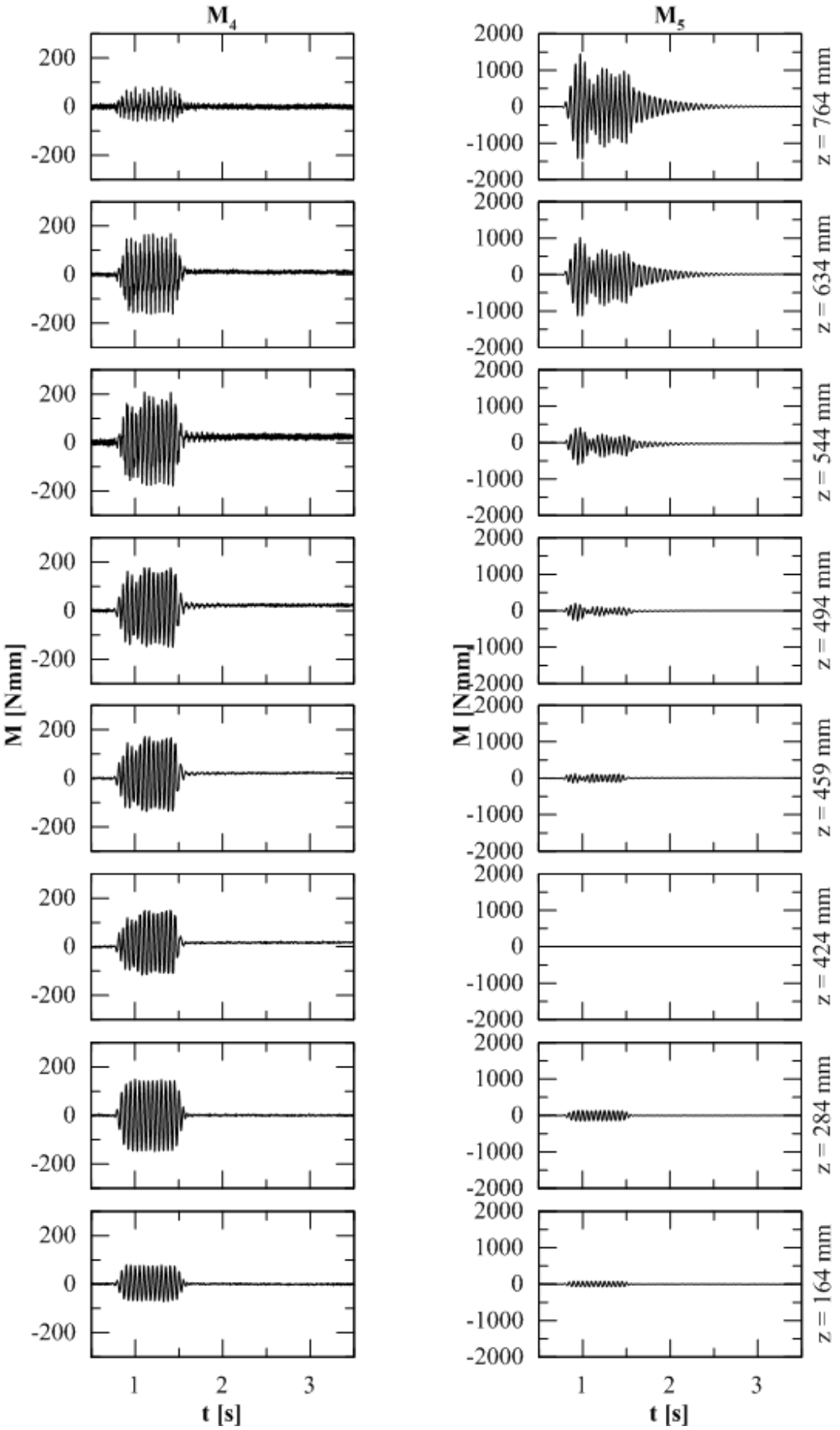

Figure 4.72. Time histories of bending moments at each depth for FHP+SDOF

4.3.3. Earthquake response

The earthquake tests are carried out in the second phase of the experimental campaign. The results presented hereafter refer to records scaled 12 times in frequency. The characteristics of the oscillators considered herein, already described in §3.4.2, are summarized in Table 4.7.

Table 4.7. Main properties of the oscillator used in the earthquake tests

Configuration	Column details	Total added mass [g]	Fixed base frequency (f_{fix}) [Hz]	Damping [%]
FHP+SDOF1 SC+SDOF1	Aluminium h=100mm	150	27.02	0.59
SC+SDOF2	Steel h=100mm	630	26.15	

The analyses of the earthquake responses confirm the behaviour observed in the harmonic tests considered above. Selected results for each scaled earthquake record (Table 4.8) are shown in terms of envelopes of absolute soil accelerations and bending moment along pile 5.

Table 4.8. Earthquake results presented

Earthquake record	Scaling Factor	PGA [g]	Configuration
Nocera Umbra Biscontini	12	0.57	FHP SC+SDOF1
Tolmezzo	12	0.1	FHP+SDOF1 SC+SDOF1
Sturno	12	0.15	SC+SDOF1 SC+SDOF2

For the Nocera Umbra Biscontini record, in Figure 4.73 the results of short-cap connection with oscillator on pile 5 and free-head pile configurations are compared. The pile response is typical in both the configurations. The redistribution of the bending moments in the SC+SDOF configuration due to combined effect of the connection and

the oscillator produces a reduction of about 30% in the kinematic bending moment at the soil layer interface.

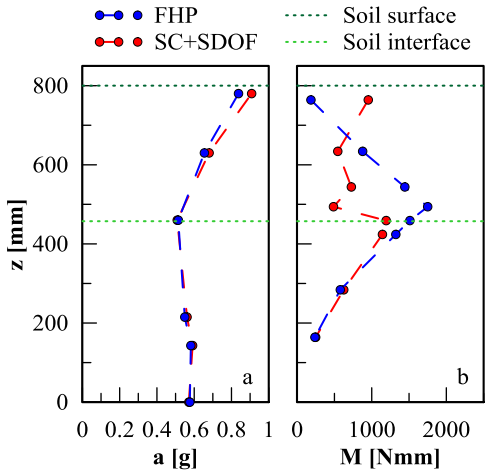

Figure 4.73. Soil (a) and pile (b) responses for FHP (blue) and SC+SDOF (red) configurations (input: Nocera Umbra SF12, PGA 0.57g)

For the Tolmezzo record, in Figure 4.74 the results of short-cap connection and free head pile both with the aluminium oscillator on pile 5 are compared. The pile response in the two configurations is again similar to the one observed in the harmonic tests. As previous, the short-cap connection induces a reduction on the interface bending moment of about 30%.

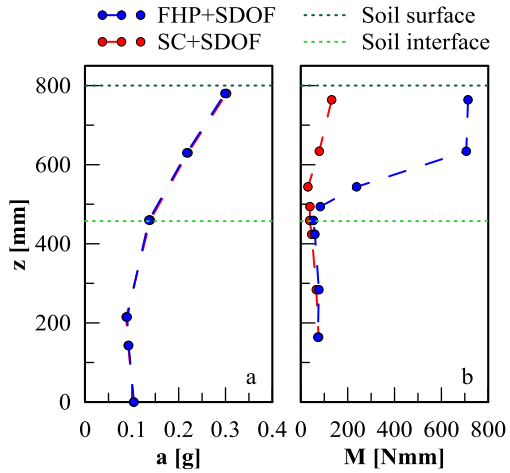

Figure 4.74. Soil (a) and pile (b) responses for the FHP+SDOF (blue) and SC+SDOF (red) configurations (input: Tolmezzo SF12, PGA 0.1g)

For the Sturno record, in Figure 4.75 the results of two short-cap connection configurations with both aluminium and steel oscillators on pile 5 are compared. In these tests the free-field response does not correspond and, in turn, it is not possible to distinguish in an accurate manner the contribute of the oscillator with the one of the soil acceleration. Nevertheless the bending moment at pile head is comparable and the inertial effect on pile response disappears after the soil layer interface.

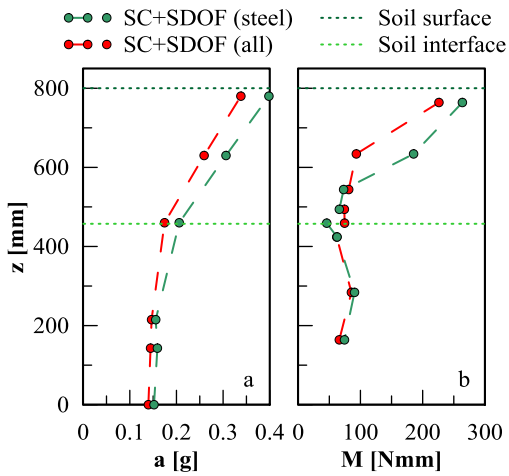

Figure 4.75. Soil (a) and pile (b) responses for the SC+SDOF configurations with steel (green) and aluminium (red) oscillators (input: Sturno SF12, PGA 0.15g)

5. NUMERICAL SIMULATIONS

The main results of the numerical simulation of the physical model tested in the experimental campaign are reported in this chapter. The comparison between the experimental and numerical results is shown in terms of time-histories and envelopes for soil, piles and oscillator responses. Numerical analyses are carried out using the difference element code FLAC 2D (Itasca, 2005). This code is an explicit finite difference program for geotechnical engineering mechanics computation capable to model the soil-structure interaction under seismic condition.

Particular attention is paid on the mechanical properties of the soil deposit. More specifically, an inhomogeneous shear wave velocity profile for the by-layer deposit is adopted. The close-form analytical formulation used for the evaluation of the initial shear wave profiles was developed in this work.

For the soil deposit the non-linear hysteretic Ramberg-Osgood model is used. This model was implemented in FLAC using the program's option for the User Define Models (UDM). Pile foundations are modelled taking into account shear and normal springs for the pile interface. The oscillator is modelled using beam elements.

The first part of this chapter is dedicated to the description of the numerical model. The comparison with the experimental results in both dynamic and seismic condition is reported in the second part of the chapter.

5.1. IMPLEMENTATION OF THE NUMERICAL MODEL

FLAC 2D (Two-Dimensional Fast Lagrangian Analysis of Continua; Itasca, 2005) is an explicit finite difference commercial software suitable for geotechnical engineering applications. The analyzed materials are discretized into a grid formed by elements, or

zones. This grid can be adjusted to fit the shape of the modeled object. The software can be used with a user graphical interface (GUI) or an internal command line language called FISH, providing powerful pre and post-processing tools. The elements behave according to linear or non-linear stress/strain constitutive laws, applied forces and boundary conditions. FLAC solves the dynamic equations of motion even in static conditions. This formulation ensures stability to the solution. The general calculation sequence used by FLAC, is illustrated in Figure 5.1. For each calculation step, velocities and displacements are calculated from the stress field and the forces applied to the nodes of the grid, then, strain rates are evaluated from the velocities, finally, using the constitutive equations, the updated stress field is calculated. One time-step is taken for every full cycle around the loop.

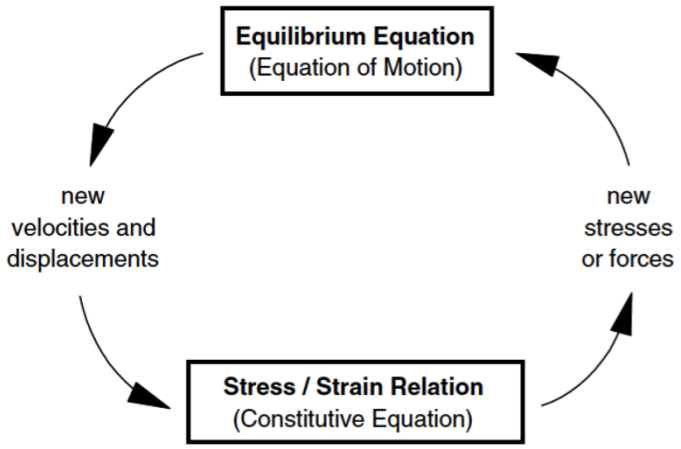

Figure 5.1. Calculation cycle used in the explicit formulation by FLAC 2D (from Itasca, 2005)

The basic assumption of the explicit formulation is that for each phase in the box of Figure 5.1, the grid variables are evaluated from known values of the others that remain fixed while control is within the box. Focus the attention, for example, on the lower box of the cycle, here, the velocities are already known, for each zone, the new stresses are calculated using the constitutive equations. The stress calculated in this manner, do not affect the velocities (that are assumed to be frozen for this calculation). This assumption could seem physically unreasonable, but, if the time-step corresponding to the cycle, is taken small enough, the assumption of frozen velocities is acceptable, because the information cannot be propagated from a zone to another in that interval. After a certain number of cycles, of course, the information propagates across the zones as they would do it physically. The explicit formulation of the finite difference method is convenient especially because do not need iterative processes, even using non-linear formulations. The main disadvantage of this approach is that the time-step could be very small and so

the calculation times can take longer than explicit formulations. Overall the explicit methods perform better than the implicit formulation for non-linear behaviors that involve large strains.

The finite difference mesh used by FLAC is composed by quadrilateral elements that are internally subdivided into two overlaid sets of constant-strain triangular elements (Figure 5.2a). This procedure prevents mesh-locking problems.

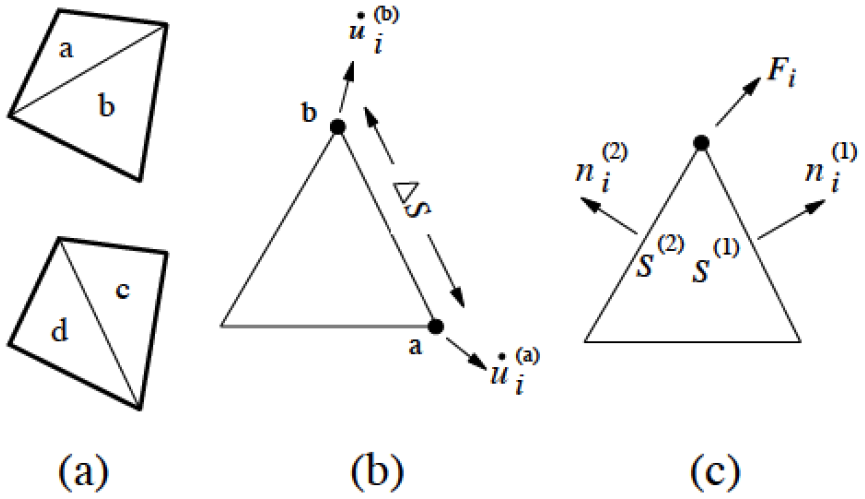

Figure 5.2. (a) Overlaid quadrilateral elements used in FLAC; (b) Typical triangular element with velocity vectors; (c) Nodal force vector (from Itasca, 2005)

In its simplest formulation, the dynamic equation of motion relates the acceleration of a mass to the applied forces (which can vary with time or be constant). The Newton's law of motion for a continuous solid body can be expressed in its general form as:

$$\rho \frac{\partial \dot{u}_i}{\partial t} = \frac{\partial \sigma_{ij}}{\partial x_j} + \rho g_i \tag{5.1}$$

where ρ is the mass density, t is the time, x_i is the ith coordinate vector, g_i the ith component of gravitational acceleration and σ_{ij} the stress tensor components.

The mechanical constitutive laws of the materials are of the form:

$$\sigma_{ij} := M\left(\sigma_{ij}, \dot{\varepsilon}_{ij}, k\right) \tag{5.2}$$

where M represents the functional form, k is a parameter that takes into account the loading history and $\dot{\varepsilon}_{ij}$ is the generic strain-rate component, expressed by:

$$\dot{\varepsilon}_{ij} = \frac{1}{2}\left(\frac{\partial \dot{u}_i}{\partial x_j} + \frac{\partial \dot{u}_j}{\partial x_i}\right) \tag{5.3}$$

For each triangle of the mesh, the finite difference equations, are derived from the generalized form of the Gauss' divergence theorem:

$$\int_S f \cdot n \, ds = \int_A \nabla \cdot f \, dA \tag{5.4}$$

where n is the normal to the surface S, f is a generic scalar or vector, x_i is the ith position vector, A is the surface of triangular domain. Defining f as the average value of the velocity along the sides of each triangle, Equation 5.4 can be re-written as:

$$\frac{\partial \dot{u}_i}{\partial x_j} \cong \frac{1}{2A} \sum_S \left(\dot{u}_i^a + \dot{u}_i^b\right) n_j \, \Delta S \tag{5.5}$$

Where the summation is over the sides of the triangular subzone, and a and b are two consecutive nodes on a side. ΔS is the side length (Figure 5.2b).

By using Equation 5.3 and 5.5, it is possible to calculate the strain rate tensor and using the constitutive equations the components of the stress tensor. Then it is straightforward to derive the equivalent forces applied to each nodal point. The stresses in each triangular subzone act as tractions on the sides of the triangle. Each traction is taken to be equivalent to two equal forces acting at the ends of the corresponding side. On each triangle two force contribute, one from each adjoining side:

$$F_i \cong \frac{1}{2} \sigma_{ij} \left(n_j^{(1)} S^{(1)} + n_j^{(2)} S^{(2)}\right) \tag{5.6}$$

In the quadrilateral zones (composed by subsets of triangles) the forces from triangles meeting at each node are summed. The forces from both sets are then averaged, to give the nodal force contribution of the quadrilateral. At each node, the forces from the surrounding quadrilaterals are summed to give the net nodal force vector ($F_1 + F_2 + \ldots + F_{i-1} + F_i$). This vector should include contribution from gravity forces, body forces and applied loads. For null zones, steady-state flow or body in equilibrium, the nodal forces are equal to zero. Otherwise, the acceleration at the nodes are derived by applying the finite difference form of Newton's second law of motion that is given as:

$$\dot{u}_i^{\left(t+\frac{\Delta t}{2}\right)} = \dot{u}_i^{\left(t-\frac{\Delta t}{2}\right)} + \sum F_i^{(t)} \frac{\Delta t}{m} \tag{5.7}$$

where the superscripts denote the time at which the corresponding variable is evaluated. For large strain problems, Equation 5.7 is integrated to determine the new coordinate of the gridpoints. Equation 5.7 and its integration are centered in time, this means that for central difference equations the first-order term of the error is equal to zero.

FLAC offers several opportunity for modeling the structural components (i.e. beam, liner, cable, pile, rockbolt, strip elements and support members). The commands necessary to define the structures invoke a very powerful and flexible structural logic. This structural logic is developed with the same finite-difference logic as the rest of the code (as opposed to a matrix-solution approach), allowing the structure to accommodate large displacements and to be applied for dynamic as well as static analysis.

5.2. MODEL GEOMETRY, MESH DISCRETIZATION AND BOUNDARY CONDITIONS

The model geometry reflects the physical model tested in the experimental campaign. A critical issue in the numerical analyses is the choice of the dimension of the mesh zones. For this choice, critical factors are: the needs of modelling the geometric details and the numerical accuracy of the wave transmission. Kuhlemeyer and Lysmer (1973), show that for an accurate representation of wave transmission through a numerical model, the element size, Δl, must be smaller than approximately one-tenth of the wavelength associated with the highest frequency component of the input wave, λ (Equation 5.8).

$$\lambda < \frac{V_s}{f_{max}} \tag{5.8}$$

where V_S is the average shear wave velocity of the model and f_{max} the highest frequency component of the input wave. The maximum tolerable zone size Δl_{max},according to this approach, is given as:

$$\Delta l_{max} < \frac{V_s}{10 f_{max}} \tag{5.9}$$

In this work, the lowest shear wave velocity (V_S = 30 m/s) and the highest frequency of the sinedwell tests simulated (f_{max} = 30 Hz), the maximum zone size (Δl_{max}) is equal to 0.1 m. Nevertheless, this value is too big to accomplish the modelling of the geometrical details. For this reason, the maximum dimension of the mesh zone is chosen equal to 0.035 m in the horizontal direction. In order to minimize the potential numerical instability, the aspect ratio (defined as the ratio between the dimension of a zone in the horizontal and vertical direction) is minimized, accordingly, the height of each zone is chosen equal to 0.038 m.

The structural elements can be divided in equal length elements (n). FLAC suggests to used always n > 1 to improve accuracy, especially with the structural elements that interact with the host medium (i.e. cable, pile, rockbolt and strip elements). In this case, the distribution of shear forces along the element is a function of the number of nodal points. The main rule to follow for the determination of the segment in piles elements is to provide approximately one element-nodal point in each FLAC zone, because the zones are constant-stress elements, and in this case, it is not necessary to have more than one interaction point within a zone. In order to verify the accuracy of the results, parametric analyses were carried out varying the number of the segments dividing the pile elements. Taking into account the results of the parametric analysis, in the final model 1 pile element for each model zone is adopted.

FLAC 2D differentiates the boundary conditions in static and dynamic analyses. In the static condition the model is restrained in the horizontal and vertical directions at the bottom, and only in the horizontal one at the model sides. In the dynamic analyses the horizontal displacements are restrained reproducing rigid base conditions (shaking table). In order to take into account the effect of the soil container tied-node conditions are considered for the lateral boundaries. This conditions force the lateral boundaries to have the same horizontal displacement. This kind of boundary condition is widely adopted for the modelling of the soil container in both centrifuge and shaking table test simulations (e.g. Ghosh and Madabhushi, 2003; Elgamal et al., 2005; Liu and Song, 2005; Popescu et al., 2006; Karamitros, 2010; Conti, 2010).

The numerical model adopted for the dynamic simulations is shown in Figure 5.3.

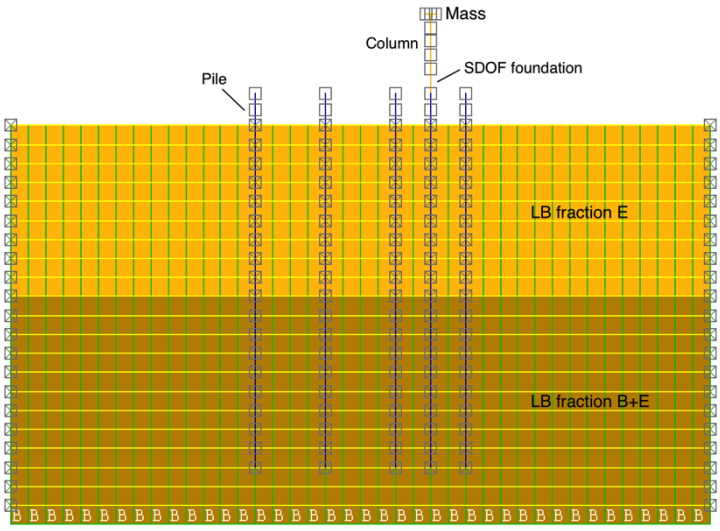

Figure 5.3. FLAC 2D model

5.3. FREE-FIELD MODEL

For the correct modelling of the free-field response the knowledge of the shear wave velocity at low strain is fundamental. To this aim, simplified closed-form solutions are developed, for typical bi-layer deposits with different combinations of inhomogeneity coefficients. The fundamental frequency is expressed as a function of the ratio of the thicknesses of the two layers, their densities and their shear wave velocities at the bottom of the deposit, as well as the shear wave velocity of the top layer. Given that these parameters are easy to establish experimentally, the developed formulations are used to estimate the shear wave velocity profiles.

Another important issue in the soil modeling is the choice of the constitutive model. In this work the hysteretic Ramberg-Osgood model is adopted using User Define Models option.

5.3.1 Material mechanical properties

The shear wave velocity of a single layer soil deposit in physical devices (e.g. a shaking table or a centrifuge) is generally estimated by correlating it to the fundamental natural frequency of the layer, to obtain a mean value corresponding to equivalent homogeneous conditions. The assumption of a pertinent equivalent shear wave velocity for the whole deposit, in the case of moderately or strongly inhomogeneous soil, can be effectively used. Approximate methods for estimating the fundamental natural period of a layered soil profile were also proposed (i.e. Madera, 1970; Dobry et al., 1971; Sarma, 1994). Towhata (1996) demonstrated that taking into account the actual variation of shear modulus (and therefore shear wave velocity) with depth for single-layer deposits could allow an improved fitting of the experimental data. The dynamic response of an inhomogeneous soil with a variation in shear wave velocity of the form $V_s = cz^n$, i.e. a parabolic function with zero value at ground surface, n being a positive inhomogeneity coefficient was investigated by several authors (ie.g. Ambraseys, 1959; Seed and Idriss, 1969; Madera, 1970, Dobry et al., 1971; Toki and Cherri, 1972; Schreyer, 1977; Gazetas, 1982). The heterogeneous soils with shear wave velocity starting from a non-zero value at ground surface, are also investigated in the literature (i.e. Rovithis et al., 2011; Mylonakis et al., 2013; Vrettos, 2013).

Using the Rayleigh quotient procedure, a generalized closed-form solution for the prediction of the fundamental natural frequency of both single and two-layer inhomogeneous deposits, taking into account a different inhomogeneity coefficient for each layer (Figure 5.4) has been developed, under the hypothesis of zero shear modulus at the ground surface.

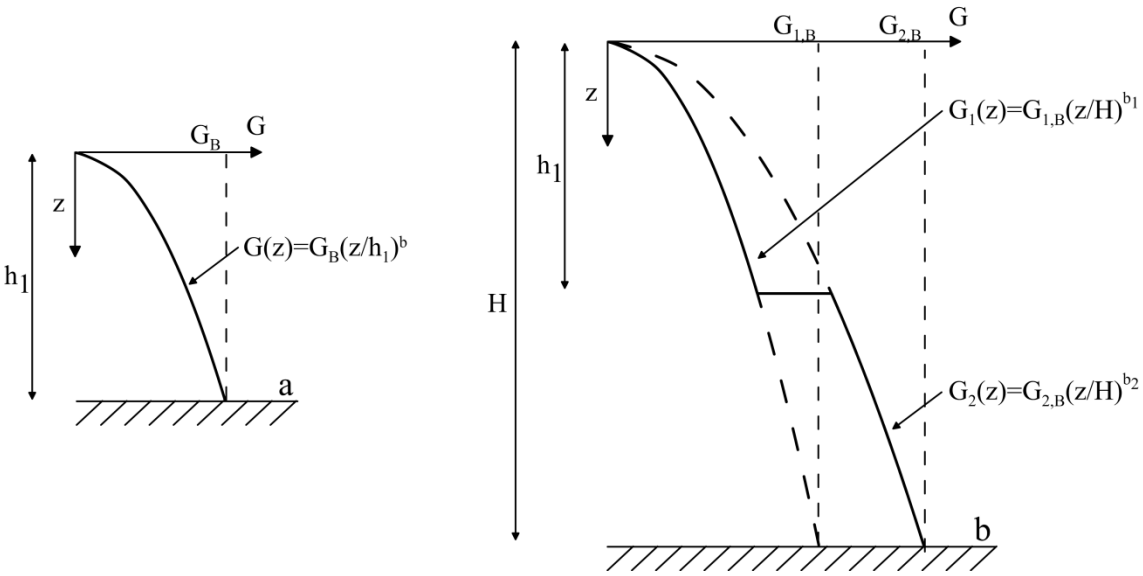

Figure 5.4. (a) Single inhomogeneous layer and (b) inhomogeneous two-layer deposit over a rigid base

The analytical investigation developed focuses upon two different cases: a single inhomogeneous layer (Figure 5.4a) and an inhomogeneous two-layer deposit (Figure 5.4b), over a rigid base. In both cases, mass density (ρ) is considered constant for each layer, while the shear modulus increases with depth according to the expression:

$$G(z)=G_B\left(\frac{z}{H}\right)^b \tag{5.10}$$

where G_B is the shear modulus at the bottom of the deposit, b is a dimensionless coefficient related to soil inhomogeneity and z is depth measured from ground surface.

The equations governing one-dimensional shear wave propagation under harmonic oscillations in an inhomogeneous soil column can be written as:

$$\frac{d}{dz}\left[G(z)\frac{du}{dz}\right]+\rho\omega^2 u=0 \tag{5.11}$$

As demonstrated by Mylonakis et al. (2013), the natural frequencies of the system may be derived from the familiar Rayleigh quotient:

$$\omega^2=\frac{\int_0^H G(z)\left(\frac{du(z)}{dz}\right)^2 dz}{\int_0^H \rho[u(z)]^2 dz} \tag{5.12}$$

Substituting $u(z)=u_0\psi(z)$, the above equation can be written as:

$$\omega^2 = \frac{\int_0^H G(z)\left(\frac{d\psi(z)}{dz}\right)^2 dz}{\int_0^H \rho[\psi(z)]^2 dz} \tag{5.13}$$

where $\psi(z)$ is a dimensionless shape function representing, approximately, the mode shape corresponding to the fundamental natural frequency of the inhomogeneous soil deposit. The shape function is obtained using a simple procedure (Clough and Penzien, 1993) as depicted in Figure 5.5. More specifically, the mode of deformation is determined as the lateral movement of the soil column, modelled as a shear beam, under a distributed horizontal load, equal to its self-weight, considering the origin of displacement axis at the top of the soil column. This allows taking into account the variations of both unit weight and shear modulus with depth.

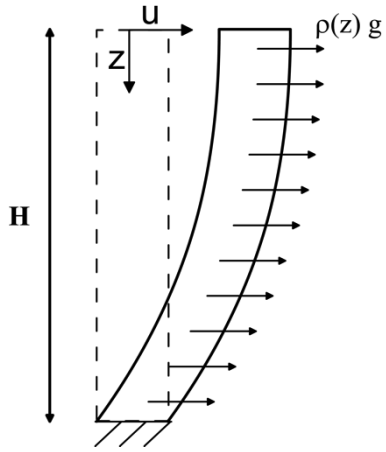

Figure 5.5. Soil model according to Clough and Penzien (1993)

In this context:

$$u(z) = \int_0^z \gamma(z)dz = \int_0^z \frac{\rho(z)gz}{G(z)} dz \tag{5.14}$$

where $\gamma(z)$ is the engineering shear strain.

The shape function employed in the Rayleigh quotient is unitary at ground surface and zero at the base, to satisfy the essential boundary conditions of the problem. Therefore,

$$\psi(z) = 1 - \frac{\int_0^z \frac{\rho(z)gz}{G(z)} dz}{\int_0^H \frac{\rho(z)gz}{G(z)} dz} \tag{5.15}$$

Specific forms of the above shape function can be written by considering the cases shown in Figures 5.4a and 5.4b, using Equation 5.10.

For instance, for a single layer having constant density, it becomes:

$$\psi(\bar{z})=1-\bar{z}^{2-b} \tag{5.16}$$

where $\bar{z} = z/H$ is the dimensionless depth.

Figure 5.6 compares the proposed shape function for a homogeneous single layer (obtained by setting *b=0* in Equation 5.16) against the theoretical shape function which is sinusoidal. It may be observed that this simplified procedure approximates the exact analytical solution with reasonable accuracy and may therefore be readily employed to handle the more complicated cases examined herein.

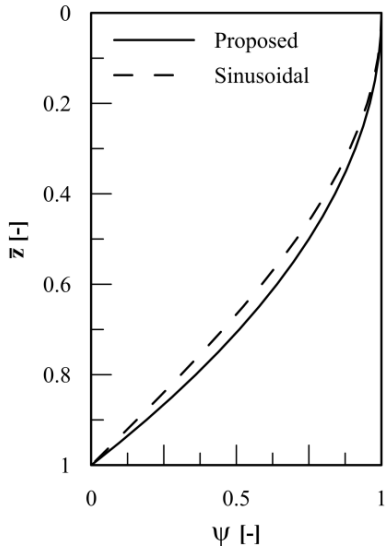

Figure 5.6. Shape functions for an homogeneous single layer

For the two-layer inhomogeneous deposit in Figure 5.4b, the shape function is obtained as follows:

$$\psi(z)=\frac{1}{D}\begin{cases}\left[\dfrac{\bar{h}_1^{\,2-b_1}-\bar{z}^{2-b_1}}{2-b_1}+\alpha\dfrac{1-\bar{h}_1^{2-b_2}}{2-b_2}\right] & 0\le\bar{z}\le\bar{h}_1\\ \left[\dfrac{\alpha}{2-b_2}\left(1-\bar{z}^{2-b_2}\right)\right] & \bar{h}_1\le\bar{z}\le 1\end{cases} \tag{5.17}$$

where $\overline{h_1} = h_1/H$ is the dimensionless thickness of the upper layer, and:

$$D=\frac{\bar{h}_1^{2-b_1}}{2-b_1}+\alpha\frac{1-\bar{h}_1^{2-b_2}}{2-b_2} \tag{5.18}$$

$$\alpha=\left(\frac{V_{s1,B}}{V_{s2,B}}\right)^2 \tag{5.19}$$

$$V_{s1,B}=\sqrt{\frac{G_{1,B}}{\rho_1}} \qquad V_{s2,B}=\sqrt{\frac{G_{2,B}}{\rho_2}} \tag{5.20a, b}$$

Figure 5.7 compares the sinusoidal shape function against the proposed one (the latter obtained assuming *b_1=b_2=0.5* in Equation 5.17) for an inhomogeneous two-layer

deposit with $\overline{h_1} = 0.5$ and $a = 0.5$. Evidently, the shape function for multilayered deposits cannot be well approximated by a sinusoidal function. This indicates that employing the procedure at hand is important in calculating the natural frequency of the system.

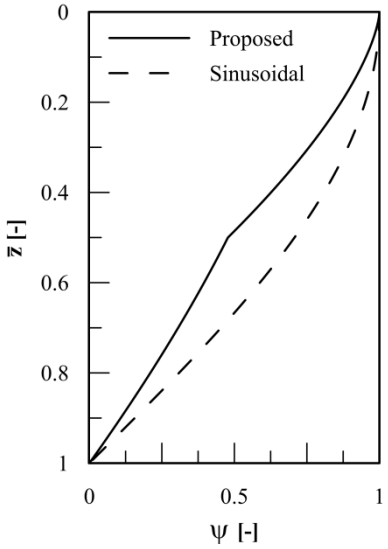

Figure 5.7. Shape functions for an inhomogeneous two-layer deposit

Referring to the single inhomogeneous soil layer in Figure 5.4a, equation 5.13 becomes:

$$\omega^2 = \frac{G_B \int_0^H \left(\frac{z}{H}\right)^b \left(\frac{d\psi(z)}{dz}\right)^2 dz}{\rho \int_0^H [\psi(z)]^2 dz} \tag{5.21}$$

Substituting the shape function in Equation 5.21, one obtains:

$$\omega^2 = \frac{(2-b)^2(5-2b)}{2\left(b^2-4b+4\right)} \frac{V_{s,B}{}^2}{H^2} \tag{5.22}$$

Three simple cases can be obtained from this solution by considering typical values of *b*:

- *b≈0*, corresponding to a homogeneous layer, typical of over-consolidated clay:

$$\omega^2{}_{b=0} = \frac{5}{2}\frac{V_{s,B}{}^2}{H^2} \cong 2.5 \frac{V_{s,B}{}^2}{H^2} \tag{5.23}$$

In this case, the corresponding shear wave velocity at the bottom of the layer is given by:

$$V_{s,B} \cong 3.97 f H \tag{5.24}$$

where *f* is the natural frequency (in units of 1/Time) of the layer.

Note that above the solution is very close to the exact one (V_s=4fH), the difference being due to the slight deviation of the generalized parabolic function in Equation 5.16 from a perfect sinusoid.

- *b≈0.5*, typical of a sand deposit:

$$\omega^2_{b=0.5} \cong 2\frac{V_{s,B}{}^2}{H^2} \tag{5.25}$$

In this case, the corresponding shear wave velocity at the bottom of the layer is given by:

$$V_{s,B} \cong 4.44fH \tag{5.26}$$

This solution can be compared against the results of Towhata (1996). Under the same assumptions, the shear wave velocity at the bottom of the layer is evaluated as:

$$V_{s,B,\,T} = 4.49fH \tag{5.27}$$

which is in meaningful agreement with Equation 5.26.

- *b≈1*, typical of a normally-consolidated clay deposit:

$$\omega^2_{b=1} \cong \frac{3}{2}\frac{V_{s,B}{}^2}{H^2} \cong 1.5\frac{V_{s,B}{}^2}{H^2} \tag{5.28}$$

In this case, the corresponding shear wave velocity at the bottom of the layer is given by:

$$V_{s,B} \cong 5.13fH \tag{5.29}$$

According to Towhata (1996), the shear wave velocity at the bottom of the layer is evaluated as:

$$V_{s,B,\,T} = 5.22fH \tag{5.30}$$

which is again in meaningful agreement with the proposed solution.

Referring to Figure 5.5b and the shape function in Equation 5.17, the solution to Equation 5.13 becomes:

$$\omega^2 = \frac{G_{1,B}\int_0^{h_1}\left(\frac{z}{H}\right)^{b_1}\left(\frac{d\psi(z)}{dz}\right)^2 dz + G_{2,B}\int_{h_1}^{H}\left(\frac{z}{H}\right)^{b_2}\left(\frac{d\psi(z)}{dz}\right)^2 dz}{\rho_1\int_0^{h_1}[\psi(z)]^2 dz + \rho_2\int_{h_1}^{H}[\psi(z)]^2 dz} \tag{5.31}$$

Evaluating the integrals, Equation 5.31 can be written as:

$$\omega^2 = \frac{A_1 + \alpha\,\alpha_1 A_2}{A_3 + \alpha^2\alpha_1 A_4}\frac{V_{s1,B}^2}{H^2} \tag{5.32}$$

where $\alpha_1 = \rho_2/\rho_1$ and

$$A_1 = \frac{\bar{h}_1^{3-b_1}}{3-b_1} \tag{5.33}$$

$$A_2=\frac{1-\bar{h}_1^{3-b_2}}{3-b_2} \tag{5.34}$$

$$A_3=\frac{\bar{h}_1^{5-2b_1}}{(2-b_1)^2(5-2b_1)}+C^2\bar{h}_1-2\frac{C\bar{h}_1^{3-b_1}}{(2-b_1)(3-b_1)} \tag{5.35}$$

$$A_4=\frac{1}{(2-b_2)^2}\left(1-\bar{h}_1+\frac{1-\bar{h}_1^{5-2b_2}}{5-2b_2}-2\frac{1-\bar{h}_1^{3-b_2}}{3-b_2}\right) \tag{5.36}$$

$$C=\frac{\bar{h}_1^{2-b_1}}{2-b_1}+\alpha\frac{1-\bar{h}_1^{2-b_2}}{2-b_2} \tag{5.37}$$

Although the above solution is simple to implement, a graphical form of the results is also provided for routine use (Figure 5.8), without the need for a spreadsheet or a pocket calculator. The format utilized for the graphical representation is the same as the one adopted by Madera (1970), where the ratio of the deposit eigenvalue T over the top layer eigenvalue T_1 is provided as a function of the layer thickness ratio h_1/h_2 and the stiffness ratio $(V_{s1}h_2)/(V_{s2}h_1)$. Nine cases are examined for various combinations of over-consolidated clay (b=0), sand (b=0.5) and normally-consolidated clay (b=1) layers. Note that the first graph of Figure 5.8 corresponds to the same case examined by Madera and that a very good agreement is observed. The corresponding analytical expressions for each case are as follows:

- Case 1: over-consolidated clay over over-consolidated clay *($b_1=b_2=0$)*, $\alpha_1 = 1$

$$\omega^2=\frac{5\bar{h}_1^3+5\alpha\left(1-\bar{h}_1^3\right)}{\bar{h}_1^5(3\alpha^2-5\alpha+2)+5\alpha\bar{h}_1^3(1-\alpha)+2\alpha^2}\frac{V_{s1,B}^2}{H^2} \tag{5.38}$$

- Case 2: sand over sand *($b_1=b_2=0.5$)*, $\alpha_1 = 1$

$$\omega^2=\frac{9\bar{h}_1^{2.5}+9\alpha\left(1-\bar{h}_1^{2.5}\right)}{\bar{h}_1^4(7.5\alpha^2-12\alpha+4.5)+12\alpha\bar{h}_1^{2.5}(1-\alpha)+4.5\alpha^2}\frac{V_{s1,B}^2}{H^2} \tag{5.39}$$

- Case 3: normally-consolidated clay over normally-consolidated clay *($b_1=b_2=1$)*, $\alpha_1 = 1$

$$\omega^2=\frac{1.5\bar{h}_1^2+1.5\alpha\left(1-\bar{h}_1^2\right)}{\bar{h}_1^3(2\alpha^2-3\alpha+1)-3\alpha\bar{h}_1^2(\alpha-1)+\alpha^2}\frac{V_{s1,B}^2}{H^2} \tag{5.40}$$

- Case 4: over-consolidated clay over sand *($b_1=0$ $b_2=0.5$)*, $\alpha_1 = 1$

$$\omega^2=\frac{7.5\bar{h}_1^3+9\alpha\left(1-\bar{h}_1^{2.5}\right)}{3\bar{h}_1^5-10\alpha\bar{h}_1^{4.5}+7.5\alpha^2\bar{h}_1^4+10\alpha\bar{h}_1^3-12\alpha^2\bar{h}_1^{2.5}+4.5\alpha^2}\frac{V_{s1,B}^2}{H^2} \quad (5.41)$$

- Case 5: over-consolidated clay over normally-consolidated clay *(b_1=0 b_2=1)*, $\alpha_1 = 1$

$$\omega^2=\frac{2\bar{h}_1^3+3\alpha\left(1-\bar{h}_1^2\right)}{0.8\bar{h}_1^5-4\alpha\bar{h}_1^4+4\alpha\bar{h}_1^3(\alpha+1)-6\alpha^2\bar{h}_1^2+2\alpha^2}\frac{V_{s1,B}^2}{H^2} \quad (5.42)$$

- Case 6: sand over over-consolidated clay *(b_1=0.5 b_2=0)*, $\alpha_1 = 1$

$$\omega^2=\frac{3\bar{h}_1^{2.5}+2.5\alpha\left(1-\bar{h}_1^3\right)}{1.5\alpha^2\bar{h}_1^5-3\alpha\bar{h}_1^{4.5}+1.5\bar{h}_1^4-2.5\alpha^2\bar{h}_1^3+3\alpha\bar{h}_1^{2.5}+\alpha^2}\frac{V_{s1,B}^2}{H^2} \quad (5.43)$$

- Case 7: sand over normally-consolidated clay *(b_1=0.5 b_2=1)*, $\alpha_1 = 1$

$$\omega^2=\frac{1.2\bar{h}_1^{2.5}+1.5\alpha\left(1-\bar{h}_1^2\right)}{0.6\bar{h}_1^4-2.4\alpha\bar{h}_1^{3.5}+2\alpha^2\bar{h}_1^3+2.4\alpha\bar{h}_1^{2.5}-3\alpha^2\bar{h}_1^2+\alpha^2}\frac{V_{s1,B}^2}{H^2} \quad (5.44)$$

- Case 8: normally-consolidated clay over over-consolidated clay *(b_1=1 b_2=0)*, $\alpha_1 = 1$

$$\omega^2=\frac{3\bar{h}_1^2+2\alpha\left(1-\bar{h}_1^3\right)}{1.2\alpha^2\bar{h}_1^5-3\alpha\bar{h}_1^4-2\bar{h}_1^3(\alpha^2-1)+3\alpha\bar{h}_1^2+0.8\alpha^2}\frac{V_{s1,B}^2}{H^2} \quad (5.45)$$

- Case 9: normally-consolidated clay over sand *(b_1=1 b_2=0.5)*, $\alpha_1 = 1$

$$\omega^2=\frac{3.75\bar{h}_1^2+3\alpha\left(1-\bar{h}_1^{2.5}\right)}{2.5\alpha^2\bar{h}_1^4-5\alpha\bar{h}_1^{3.5}+2.5\bar{h}_1^3-4\alpha^2\bar{h}_1^{2.5}+5\alpha\bar{h}_1^2+1.5\alpha^2}\frac{V_{s1,B}^2}{H^2} \quad (5.46)$$

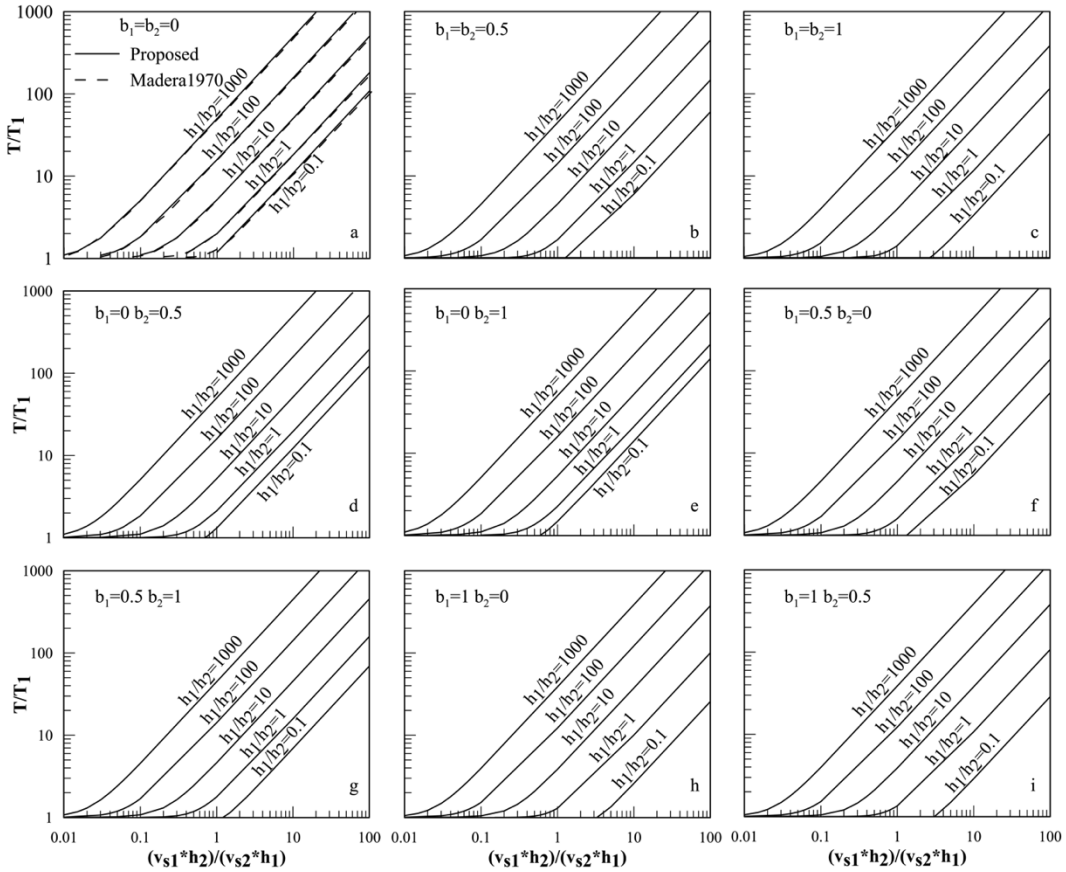

Figure 5.8. Graphical solutions for proposed method for over-consolidated clay over over-consolidated clay (a), sand over sand (b), normally-consolidated clay over normally-consolidated clay (c), over-consolidated clay over sand (d), over-consolidated clay over normally-consolidated clay (e), sand over over-consolidated clay (f), sand over normally-consolidated clay (g), normally-consolidated clay over over-consolidated clay (h) and normally-consolidated clay over sand (i)

In order to estimate the shear wave velocity profile using this methodology, the fundamental frequencies obtained from the lower white-noise available are used (§4.1.1). The computed frequencies, namely $f_1=38.9Hz$ and $f_{tot}=26.9Hz$, allow the evaluation of the shear wave velocity profile of the model, by means of the developed method, with $b_1=b_2=0.5$, first using Equation 5.26 for the evaluation of shear wave velocity $V_{s1,B}$ for the top layer, and then Equation 5.32 for the evaluation of $V_{s2,B}$ for the underlying one. The values obtained using this procedure are $V_{s1,B}=72.8m/s$ and $V_{s2,B}=93.9m/s$, while the corresponding shear wave velocity profile is shown in Figure 5.9a. Nevertheless, it was found that the corresponding shear moduli are not actually the initial ones. This is because, in spite of the low excitation amplitude employed in the white-noise test, the shear strains induced in the soil deposit were not negligible. In fact, if the aforementioned shear wave velocity profiles were considered in a ground response analyses with EERA (Bardet et al., 2000), shear strains between $2\cdot10^{-5}$ and $4\cdot10^{-5}$ would be predicted for the white-noise test, corresponding to a stiffness

degradation of 10-20%. The resulting degraded shear wave velocities are compared with the initially predicted ones in Figure 5.9a.

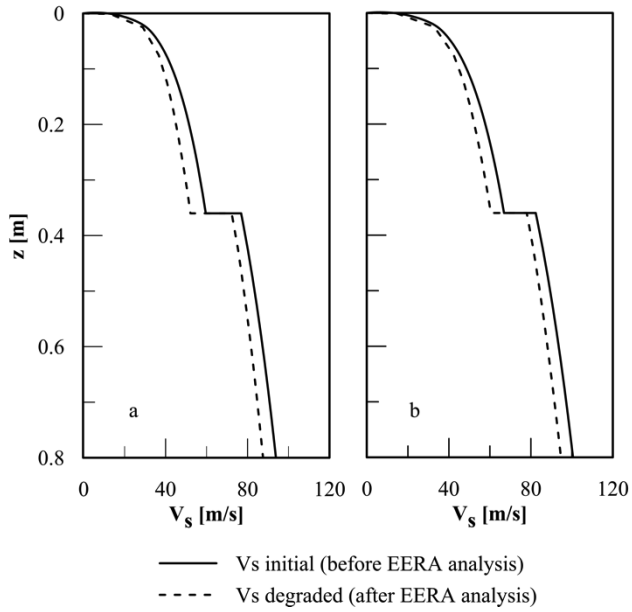

Figure 5.9. Initial and degraded shear wave velocity vs depth for the analytically computed profile (a) and the corrected one (b)

In order to account for this effect, the analytically computed shear wave velocities were increased by 12% for the top layer and 7% for the bottom one, to $V_{s1,B}$*=81.7m/s* and $V_{s2,B}$*=100.6m/s*, with the resulting shear wave velocity profile being shown in Figure 5.9b. Repeating the ground response analyses for the white-noise test with the updated shear wave profile, the degraded shear wave velocity profile may be similarly obtained. As it may be observed in Figure 5.9b, these degraded shear wave velocities are in good agreement with the ones initially obtained with the analytical methodology. Furthermore, the numerically obtained transfer functions for both the whole system and the top layer are plotted in Figure 5.10, indicating a meaningful agreement with the experimentally computed ones. In fact, Table 5.1 highlights that in terms of resonance frequency, the difference between numerical analyses and experimental results is not larger than 2.3%.

Table 5.1. Fundamental frequency of the system (f_{tot}) and the top layer (f_1) for white noise input (a_{max}=*0.019g*): experimental and numerical results

	Experimental	Numerical (frequency domain analysis)	Variation [%]
f_{tot} [Hz]	26.9	26.3	2.23
f_1 [Hz]	38.9	38.4	1.29

5.3.2 Constitutive model

The constitutive model used for the soil elements is the hysteretic non-linear model proposed by Ramberg-Osgood (1943). This model is defined in incremental form and it is combined with a step-by-step integration of the differential equation of motion, using the tangential values of the constitutive soil properties. The Ramberg-Osgood model is able to simulate in a realistic manner the degradation of the shear modulus (G) and the consequent increasing of the hysteretic damping (D) with shear strain values (γ). The constitutive model has been implemented in FLAC 2D as a User Defined Model (i.e. Bouckovalas et al., 2002; Andrianopoulos 2006).

The Ramberg-Osgood constitutive model allows simulation of the hyperbolic shape of the backbone shear stress (τ) –shear strain (γ) response, and the strain hardening exhibited beyond the yield limit by many soils. The analytical relationship between shear stress and strain for an unloading-reloading symmetric stress cycle is expressed as:

$$\gamma - \gamma_c = \frac{\tau - \tau_c}{G_0}\left[1 + \left(\frac{1}{a_y} - 1\right)\left(\frac{|\tau - \tau_c|}{2\tau_1}\right)^{w-1}\right] \tag{5.47}$$

where:

τ_c, γ_c are the shear stress and strain amplitude during the cycle respectively;

a_y, w, τ_1 are material dependent model constants. More specifically, a_y is the value of G/G_0 ratio for $\tau=\tau_1$, while w controls the rate of the shear modulus G degradation with increasing shear stress.

According to this formulation, the tangent shear modulus is computed as follows:

$$G_t = \frac{G_0}{T} \tag{5.48}$$

where:

$$T=\begin{cases} 1+2\left(\frac{1}{\alpha_1}-1\right)\frac{|X|}{\eta_1} & \text{for initial shearing} \\ 1+2\left(\frac{1}{\alpha_1}-1\right)\frac{|X^{LR}|}{2\eta_1} & \text{after the first load reversal} \end{cases} \quad (5.49)$$

with:

X scalar measure of the deviatoric stress ratio (X^{LR} is the value at last load reversal), evaluated as:

$$X=\sqrt{\frac{1}{2}\left(r_{ij}-r_{ij}^{LR}\right)\left(r_{ij}-r_{ij}^{LR}\right)} \quad (5.50)$$

r_{ij} deviatoric stress ratio (r_{ij}^{LR} is the value at last load reversal), defined as the ratio of the deviatoric stress tensor $s_{ij}=\sigma'_{ij}-\sigma'_m\cdot\delta_{ij}$ over the mean effective stress $\sigma'_m=\sigma'_{kk}/3$;

η_1 model parameter defined as:

$$\eta_1=\alpha_1\left(\frac{G_{max}^{LR}}{\sigma^{LR}}\right)\gamma_1 \quad (5.51)$$

G^{LR}_{max} the maximum shear modulus at last load reversal;

σ^{LR} the isotropic stress at last load reversal;

α_1 and γ_1 model parameters.

The model parameter α_1 quantifies the non-linearity for small strain amplitudes (Figure 5.10). A decrease of this parameter leads to increased non-linearity, while for α_1=1 the behaviour is linear.

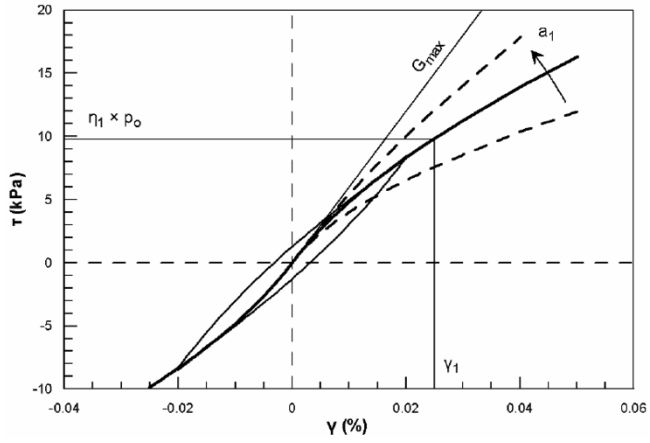

Figure 5.10. Exemplary pure shear stress-strain relation according to the Ramberg-Osgood formulation: shear reversal and effect of α_1 (from Karamitros, 2010)

The model parameter γ_1 may be interpreted as a threshold shear strain beyond which any further degradation to the overall stiffness is due to the development of plastic strain (Figure 5.11).

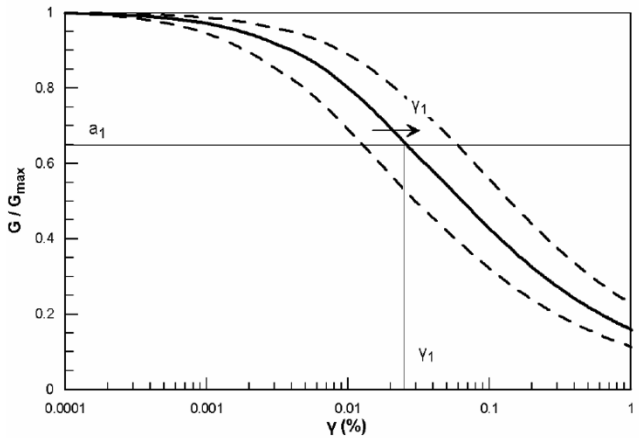

Figure 5.11. Exemplary shear modulus degradation with increasing shear strain, according to the Ramberg-Osgood formulation: effect of γ_1 (from Karamitros, 2010)

The calibration of the two model parameters of the Ramberg-Osgood model for the prediction of the soil behaviour was made by using the experimental *G(γ)* and *D(γ)* curves of Vucetic and Dobry (1991) for zero plasticity index (Figure 5.12). The obtained parameters are $\alpha_1=0.064$ and $\gamma_1=0.00016$.

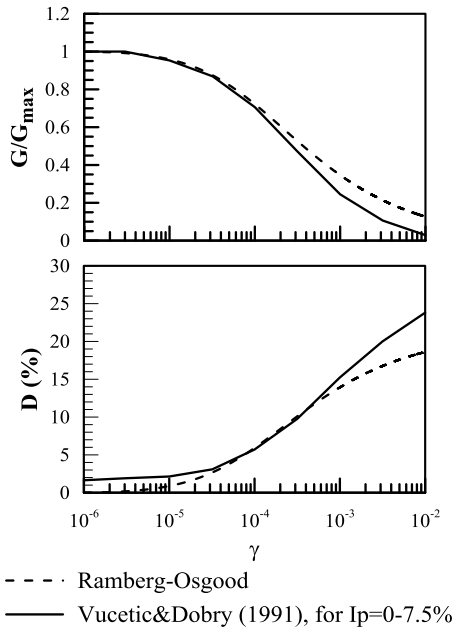

Figure 5.12. Shear modulus reduction and damping ratio curves adopted

The hysteretic damping ratio predicted by the Ramberg-Osgood constitutive model goes to zero for very small shear strain values (Figure 5.12). In order to compensate this low damping response an additional Rayleigh damping of 5% is added.

The Rayleigh damping equations are expressed in matrix form. The damping matrix (C) is used, with components proportional to the mass (M) and stiffness (K) matrices:

$$C = \alpha M + \beta K \tag{5.52}$$

Where α and β are the mass and stiffness proportional damping constant respectively.

The variation of the normalized critical damping ratio with angular frequency (ω_i) is shown in Figure 5.13. Three curves, corresponding to the mass and stiffness components only and the sums of both, are reported in the Figure 5.13. It is clear that the mass proportional damping is dominant at lower angular-frequency ranges, while for higher values the stiffness proportional damping is dominant. The minimum of these component is reached at:

$$\xi_{min} = (\alpha\beta)^{1/2} \quad ; \quad \omega_{min} = (\alpha/\beta)^{1/2} \tag{5.53}$$

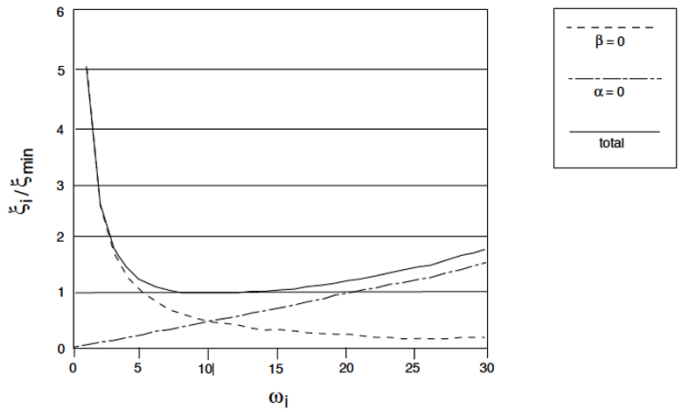

Figure 5.13. Variation of normalized critical damping ratio with angular frequency (from Itasca, 2005)

The Rayleigh damping is specified in FLAC with the parameters f_{min} ($\omega_{min}/2\pi$) and ξ_{min}.

The friction angles of the two layers were obtained based on the well known Bolton (1986) and Cavallaro et al. (2001) formulations, due to the absence of ad-hoc laboratory tests. Friction angles equal to 35° and 38° are adopted for the LB fraction E (upper layer) and fraction B+E (bottom layer), respectively.

5.4. PILE MODEL

The piled foundation is modelled using the structural "pile" element implemented in FLAC. This component is a two-dimensional element with three degrees of freedom (two displacements and one rotation) at each node. Piles interact with the FLAC grid via shear and normal coupling springs. These springs are non-linear connectors that transfer forces and motion between the pile elements and the grid at the pile nodes.

The shear behaviour of the pile/grid interface is represented as a spring-slider system at the pile nodal points. The maximum shear force that can be developed along the

interface is a function of the cohesive strength of the interface and the stress-dependent frictional resistance along the interface (Figure 5.14).

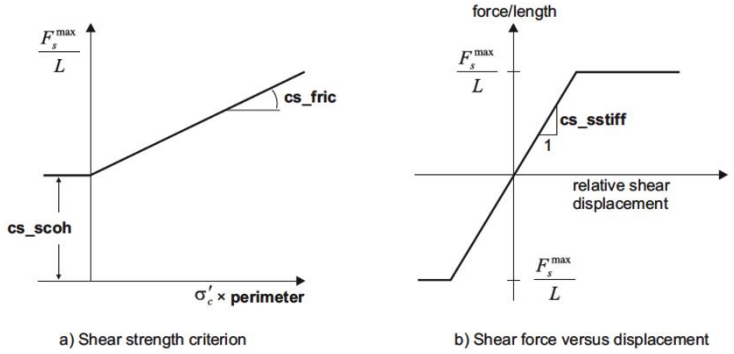

Figure 5.14. Material behaviour of shear coupling spring for pile elements (from Itasca, 2005)

The behaviour of the normal coupling springs includes the capability to model load reversal and the formation of a gap between the pile and the grid. The normal coupling springs are primarily intended to simulate the effect of the medium squeezing around the pile and it is dependent on the direction of movement of the pile node. The normal-force relation is shown in Figure 5.15.

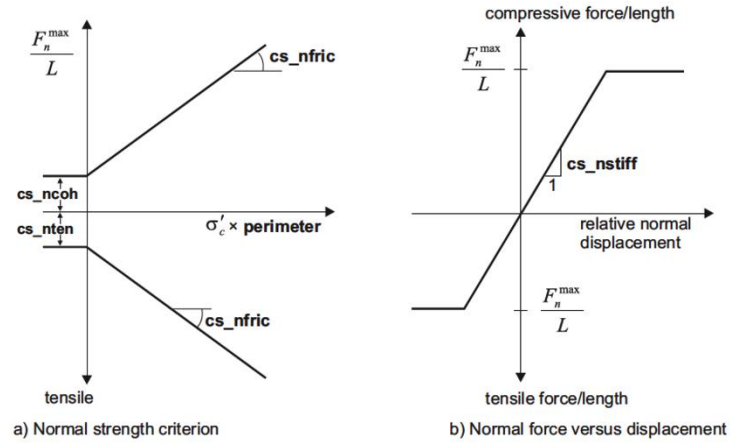

Figure 5.15. Material behaviour of normal coupling spring for pile elements (from Itasca, 2005)

The seismic behaviour of pile groups is a three dimensional problem and the pile formulation simulates a row of equally spaced piles in plane-strain symmetry. Nevertheless, it is possible to reduce it in regularly spaced piles to two-dimensional problem involving the averaging effect in 3D over the distance among the elements. According to Donovan et al. (1984) a linear scaling of material properties is applied.

In this work the shear spring properties are estimated from the soil properties, assuming that the failure associated with the pile/soil response occurs in the soil. For this reason the frictional resistance of the shear coupling spring is assumed equal to 2/3 of the internal friction of the soil. The stiffness of the shear coupling spring (k_s) is

assumed equal to ten times the equivalent stiffness of the stiffest neighboring zone, evaluated with the follows:

$$k_s = 10\left[\frac{\left(K + \frac{4}{3}G\right)}{\Delta z_{min}}\right] \tag{5.54}$$

where K and G are the bulk and shear moduli, respectively; Δz_{min} is the smallest width of an adjoining zone in the normal direction.

The variation with depth of the shear stiffness adopted in the numerical model is reported in Figure 5.16.

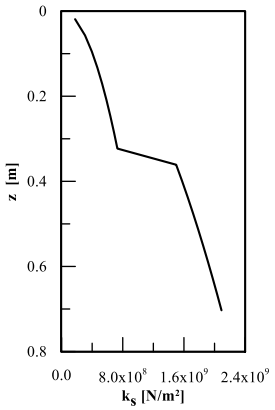

Figure 5.16. Variation with depth of the soil-pile coupling shear stiffness

For the evaluation of the normal coupling spring properties the pile response is evaluated in terms of force per unit length – relative displacement (p-y) using the analytical method by Georgiadis et al. (1992) for piles in cohesionless soils (Figure 5.17). The curve is defined by means of an initial subgrade modulus (k_{ini}) and an ultimate value for soil resistance (p_{ult}), according to the following hyperbolic relationship:

$$p = \frac{y}{\frac{1}{k_{ini}} + \frac{y}{p_{ult}}} \tag{5.55}$$

According to Reese et al. (1974), the ultimate value for the soil resistance depends on the unit weight of the soil, the friction angle of sand, the at rest earth pressure and the active earth pressure coefficients and the pile diameter. According to Terzaghi (1955), values of n_h equal to 1500 and 2000 kN/m^3 for the top and bottom layers respectively are employed (Table 5.2).

Table 5.2. Coefficient of initial subgrade modulus, n_h (from Terzaghi, 1955)

Relative Density	Loose	Medium	Dense
n_h [kN/m^3]	1100 - 3300	3300 - 11000	11000 - 23400

In order to implement the computed p-y curve in FLAC, an equivalent elasto-plastic curve is fitted (Figure 5.17), using an equivalent subgrade modulus (k_{eq}), This parameter is defined as the stiffness of the hyperbolic curve at the displacement that corresponds to the 50% of the ultimate resistance (y_{50}), defined as:

$$k_{eq} = \frac{0.5 p_{ult}}{y_{50}} \tag{5.56}$$

Taking into account the formulation of the hyperbolic curve, it can be considered:

$$k_{eq} = \frac{k_{ini}}{2} \tag{5.57}$$

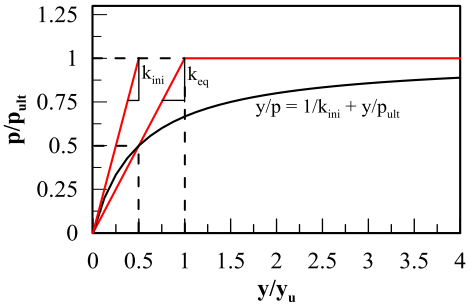

Figure 5.17. Hyperbolic p-y curve proposed by Georgiadis et al. (1992) and equivalent elasto-plastic fitting

The variation with depth of the normal coupling stiffness and the corresponding ultimate resistance adopted in the numerical model are reported in Figure 5.18a and 5.18b respectively.

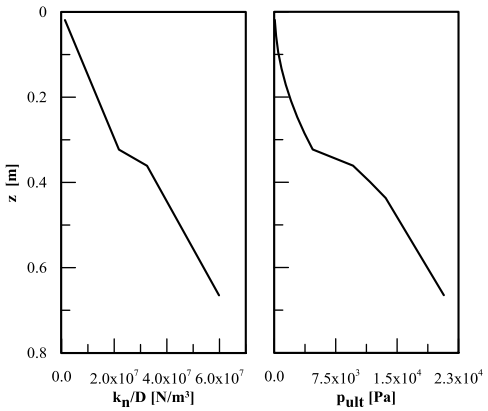

Figure 5.18. Variation with depth of the soil-pile coupling normal stiffness (a) and ultimate soil resistance (b)

The accuracy of the soil-pile interface of the numerical model can be evaluated simulating the pullover test results (§3.2.1) with FLAC. The system configuration is shown in Figure 5.19.

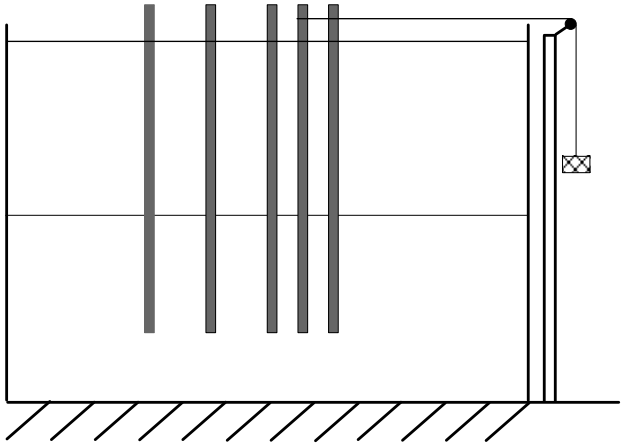

Figure 5.19. System configuration in pullover test

The test consists in the application of small increments of lateral load at the pile head (Figure 5.20a) monitoring the lateral displacement induced by these loads (Figure 5.20b). The comparison between the experimental data and the numerical results (Figure 5.21) shows that model is able to reproduce in an accurate manner the pile response.

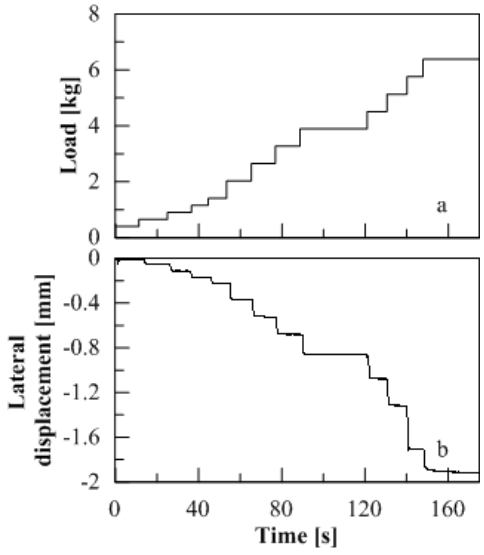

Figure 5.20. Time histories of applied loads (a) and lateral displacement (b) in the pullover test

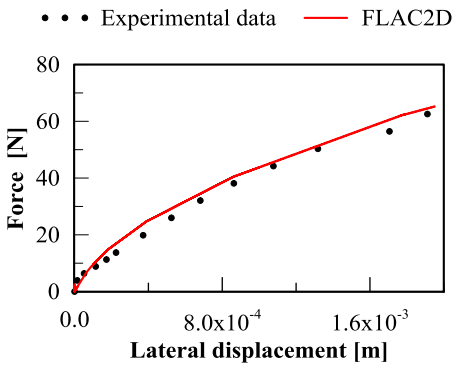

Figure 5.21. Experimental and numerical results of pullover test

5.5. FIXED BASE OSCILLATOR

A crucial aspect in the modelling of the soil-pile-structure interaction is related to the correct simulation of the fixed base oscillator. In this context, in this paragraph, the fixed base oscillator simulated with FLAC is validated using the finite element code SAP2000 (CSI, 2013). Modal analyses are carried out with SAP2000 and compared with the experimental results. After the validation of the SAP2000 model, the results were used to validate the fixed base model performed with FLAC, comparing the time histories responses at the top of the oscillator excited with an harmonic input.

5.5.1 Modal analysis

The finite element code SAP2000 (CSI, 2013) is used for a linear elastic modal analysis of the fixed base oscillator. The vibration modes of the structure has been obtained using the eigenvector analysis that involves the solution of the follow generalized eigenvalue problem:

$$[K - \Omega^2 M]\Phi = 0 \tag{5.58}$$

where K is the stiffness matrix, M is the diagonal mass matrix, Ω^2 is the diagonal matrix of eigenvalues and Φ is the matrix of corresponding eigenvectors.

Figure 5.22 and Table 5.3 show that the natural frequency obtained from the numerical analysis are always a higher than the experimental ones, as expected. This difference could be related to the difference between the perfectly restrained base oscillator modelled and the experimental one.

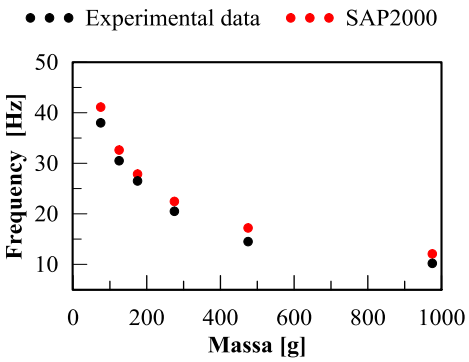

Figure 5.22. Experimental and numerical fixed base response

Table 5.3. Experimental and numerical fixed base response

Total added mass [g]	Experimental fixed base frequency [Hz]	Numerical fixed Base frequency [Hz]	Variation [%]
75	38.0	43.7	13.0
125	30.5	33.9	10.0
175	26.5	28.6	7.3
275	20.5	22.8	10.1
475	15.0	17.4	13.8
975	10.0	12.1	17.4

5.5.2 Response history analysis

The responses in terms of time-histories are carried out for the oscillators for evaluating the capability of the FLAC model to correctly simulate the structural response. The oscillator is modelled in FLAC using beam element. The beam element in FLAC is considered elastic and the mechanical characteristics assumed are the same of the experimental column. The mass at the top of the column is assigned by means of another beam rigidly connected at the top of column with an high mass density able to reproduce the inertial response of the mass.

The damping ratio for the oscillator in the harmonic tests is considered assuming the built-in combined damping (a variation on local damping available in FLAC). The combined damping is more efficient than the local damping, for significant uniform motion, like the sinusoidal waves adopted in these analyses. Local damping is a non-viscous damping, in which the damping force on a node is proportional to the magnitude of the unbalanced force. In the earthquake tests the local damping formulation was used. The values assumed for the damping ratio were obtained from the experimental data by applying the logarithmic decrement method.

Figure 5.23 shows the comparison between the FLAC and SAP2000 models assuming a 5% of damping ratio. The comparisons between the two codes are satisfactory for all the masses.

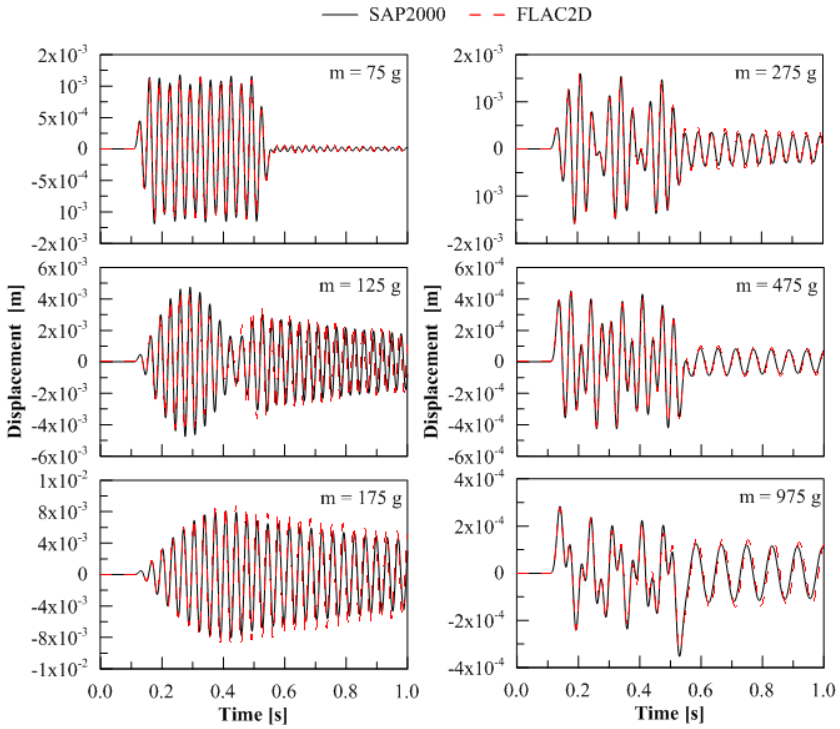

Figure 5.23. SAP2000 and FLAC2D time histories responses for fixed base oscillators

5.6. EXPERIMENTAL VERSUS NUMERICAL RESULTS

The numerical model has been validated taking into account both the dynamic and seismic inputs applied at to physical model. In both cases the results reported in the follows paragraphs refers to the complete system to evaluate the capability of the numerical model to reproduce the soil-pile-structure interaction. It should be underlined that the accelerations and displacements are measured directly in the physical model, whereas the bending moments are indirect measurements. For this reason the accuracy of the numerical model is considered evaluating the indirect measurements (bending moments) in a qualitative way and focusing the attention on the direct measurements (accelerations and displacements). It should be also highlighted that in the numerical model the instrumentation devices, that could give a contribution in the response of the physical model, was not modelled.

5.6.1 Harmonic tests

Numerical simulations of some of the data presented in the previous chapter (§4.3.2.2) are performed. The dataset includes six tests in the free-head pile with oscillator at the top of the central pile (Figure 5.24), excited by a 20 Hz harmonic input with maximum acceleration of 0.1g. Numerical simulations refer to the lower and upper bound responses of this dataset, namely the tests with oscillator masses equal to 175g and 975g.

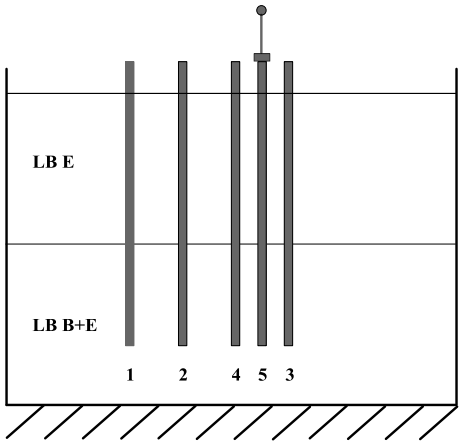

Figure 5.24. Free-head pile with oscillator configuration (FHP+SDOF)

Figure 5.25 shows the comparison between the numerical and the experimental data for the free-field (Figure 5.25a), pile 4 (Figure 5.25b) and pile 5 (Figure 5.25c) responses. Figure 5.25a ensures that soil is adequately simulated in the numerical analyses. The resonance effects are also reliably modeled for pile 5. Figure 5.25c shows that the numerical maximum bending moments at the pile head and at the interface provide close matches with outcomes of the experimental data. Conversely, Figure 5.25b shows that, for pile 4, the numerical model is able to simulate the maximum bending moment due to the kinematic interaction, nevertheless it cannot reproduce the resonance effect due to the oscillator on the other pile.

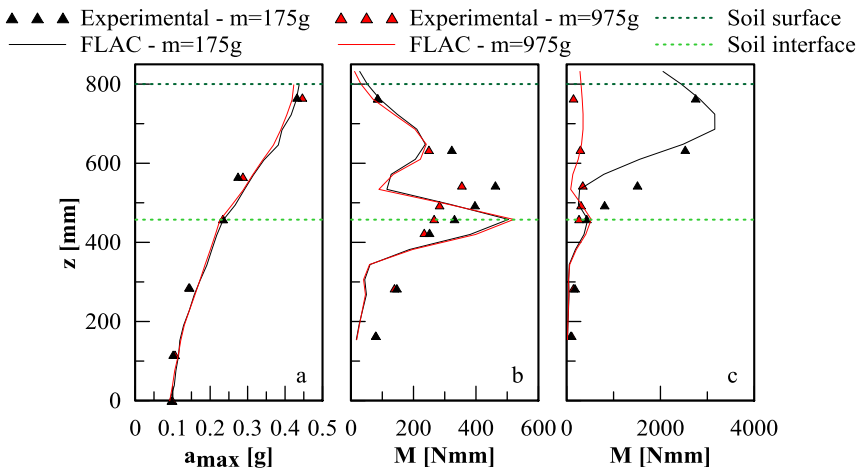

Figure 5.25. Experimental and numerical results: envelope of absolute soil acceleration (a) and bending moment for pile 4 (b) and pile 5(c) along depth

Figure 5.26 shows the comparison in terms of time histories for the test with the mass oscillator equal to 175g. On the left hand side, the comparison for the free-field vertical array at three different elevations (bottom, interface and surface) is provided. It is noticed that there is a full match between computed values and test results. It is worth mentioning that the input was applied to the sample model in terms of accelerations, simulated through an artificial sinusoidal wave (generated directly with a FLAC routine). On the right hand side of Figure 5.26, the responses close to the pile head (bending moment) and at the top of the oscillator (displacement) are reported. The results confirm that numerical model implemented in FLAC may simulate accurately the experimental data of the shaking table tests. It should be noted that the match between the experimental data and the numerical results is almost perfect in the comparison of the direct measurements. The pile response in terms of bending moments is consistent also if it is not coincident, probably due to the potential errors related to the indirect measurements and the simplification assumed in the numerical analyses (i.e. the modelling of the mounting points for test instrumentation).

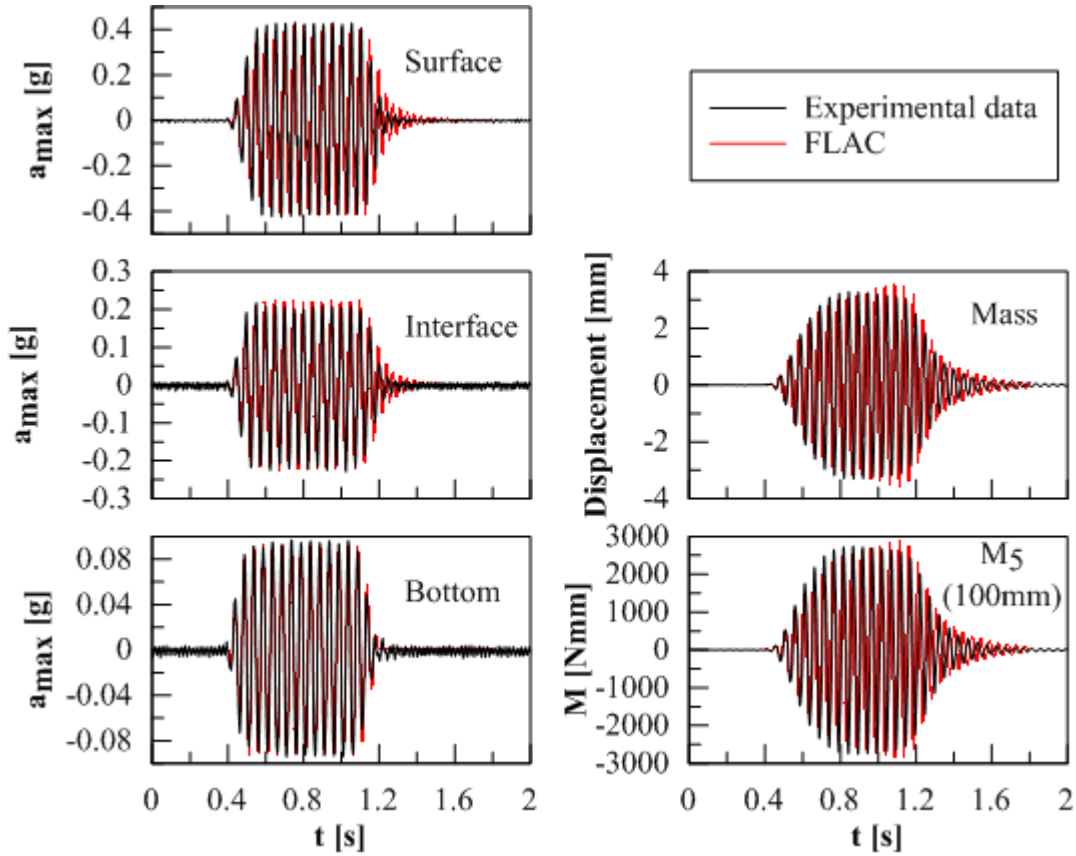

Figure 5.26. Time histories of the test with mass oscillator of 175g

It is found that the numerical model is able to reproduce in an accurate manner the period elongation. The experimental SSI in the SDOF with 175 g mass has been computed using the transfer function and a 42% of period elongation ($T_{SSI}/T_{fix} = 1.42$) was obtained ($f_{SSI} = 18.6\ Hz$). The numerical results are consistent with the measured elongation.

5.6.2 Seismic tests

The evaluation of the response of the numerical model to a seismic motion is reported herein. The simulation refers to two different pile configurations with the seismic input Nocera Umbra Biscontini (SF 12, PGA 0.57g). The configurations refer to the oscillator at the top of pile 5 with connection among pile heads (Figure 5.27a) and piles without oscillator and connection (Figure 5.27b). The experimental results have been already presented in §4.3.3.

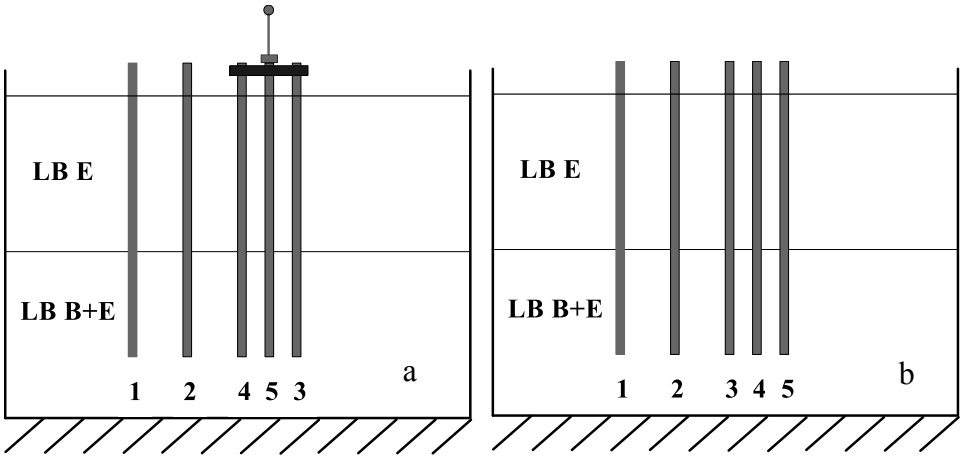

Figure 5.27. Short-cap with oscillator (a) and free-head pile (b) configurations

Figure 5.28 shows the comparison between the experimental data and numerical results for the free-field response (Figure 5.28a) and for envelope of the absolute bending moment along pile 5 (Figure 5.28b). Similar considerations to the previously discussed about the comparison can be done. The numerical model is able to reproduce in an reliable manner the system response, in both configurations.

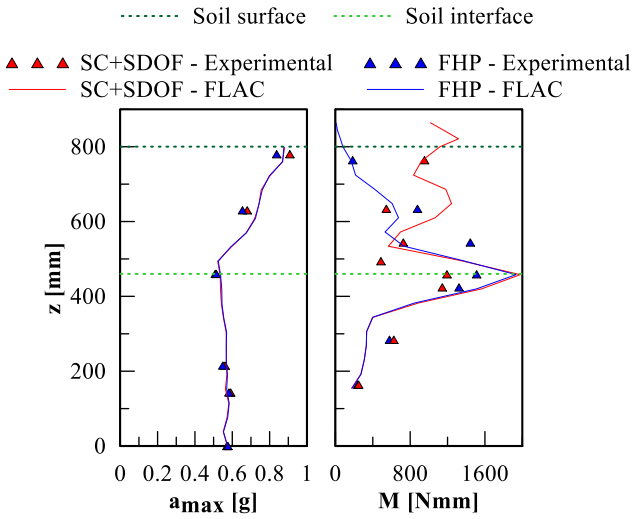

Figure 5.28. Experimental data and numerical results for SC+SDOF (red) and FHP+SDOF (blue) configurations (input: Nocera Umbra SF12, PGA 0.57g)

6. CONCLUSIONS AND FURTHER WORKS

The aim of this thesis was to examine the complex soil-pile-structure interaction using the results of a comprehensive laboratory tests performed on a 6-degree-of-freedom 1-g shaking table of the Bristol Laboratory for Advanced Dynamics Engineering (BLADE) of the University of Bristol (UK). The experimental program was carried out within the framework of the Seismic Engineering Research Infrastructures for European Synergies (SERIES).

The physical model comprises a group of five piles embedded in a bi-layer deposit with several pile-head configurations and equivalent cantilever systems (single-degree of freedom, SDOF). To investigate the seismic soil-pile-structure interaction, the model was subjected to both dynamic and seismic input motions. In order to monitor the system behaviour, the physical model was densely instrumented.

The free-field response showed the influence of the input acceleration on the natural frequency of the deposit, in particular the increasing of the acceleration induced a reduction of the natural frequency and an increasing of the damping ratio. The free-field response in terms of the envelope of absolute acceleration along depth showed the influence of the input frequency on the amplification.

The kinematic interaction was considered referring to both pile head and soil interface. The complete soil-structure interaction was also investigated, referring to several single-degree-of-freedom (SDOF). Results showed that one of the main phenomenon that influenced the dynamic behaviour is the resonance, that increases the interaction effects. The decreasing of the natural frequency and the increasing of the damping ratio of the structure are the more significant effects generated by the interaction. Another aspect investigated using the experimental data was the effect of the pile configuration on the dynamic response of the system. The presence of a

connection among pile heads induced a restrain condition similar to the fixed base, generating negligible period elongation.

The analyses of the earthquakes responses showed results similar to the ones obtained from the harmonic tests.

The wide variation of the experimental data allowed to validate an accurate numerical model using the difference element code FLAC 2D.

The inhomogeneous shear wave velocity profile in the bi-layer deposit was taken into account by menas of an analytical close-form solution devoleped and validated using the experimental data. The numerical model accounted for a Ramberg-Osgood constitutive model. The comparisons between the experimental and numerical results were satisfactory for the case studies, i.e. considering different input motions (static, dynamic and seismic) and for a variety of input accelerations.

The comprehensive study presented in this thesis contains several substantial outcomes obtained by using together shaking table test data, advanced numerical analyses and analytical solutions ad-hoc derived. An appendix of this study is an on-going research on the dynamic characteristics of the Leighton Buzzard sands for very low relative density values (like the values employed in the presented experimental campaign), by means of several laboratory tests. These further information will allow to implement more advanced constitutive models to use for an extension to a prototype (full scale model) and/or to case studies. The aim of these studies are to improve the knowledge about the complex SSI phenomena and, hopefully, provide better accuracy in the context of the seismic response forecasting.

REFERENCES

Ambraseys NN. A note on the response of an elastic overburden of varying rigidity to an arbitrary ground motion. *Bull Seism Soc Am*. 1959; 49(3):211-220;

Andrianopoulos K. Numerical Simulation of Static and Dynamic Loading of Elasto-plastic Soils. PhD Thesis, *National Technical University of Athens*. 2006;

Bardet JP, Ichii K, Lin CH. EERA a Computer Program for Equivalent-linear Earthquake site Response Analyses of Layered Soil Deposits. *Univ of Southern California, Dep of Civil Eng*. 2000;

Beskos DE. Applications of the boundary element method in dynamic soil–structure interaction. *In Development in Dynamic Soil–Structure Interaction. Dordrecht: Kluwer Academic*. 1993, 61–90;

Bhattacharya S, Lombardi D, Dihoru L, Dietz M, Crewe AJ and Taylor CA. Chapter 8: "Container Design for Soil-Structure Interaction Studies" in the book: *Role of Seismic Testing Facilities in Performance-Based Earthquake Engineering (Fardis, Michael N.; Rakicevic, Zoran T. Eds.), Springer*. 2011;

Bielak J. Dynamic behaviour of structures with embedded foundations. *Earthquake Engineering and Structural Dynamics*. 1975, 3(3), 259-274;

Blaney GW, Kausel E, Roesset JM. Dynamic stiffness of piles. *Proceedings of the 2nd International Conference on Numerical Methods in Geomechanics*. 1976, 2:1001-1012;

Bolton M. The strength and dilatancy of sands. *Géotechnique*. 1986, 36(1), 65–78;

Bouckovalas G, Andrianopoulos K, et al. Numerical Simulation of Soils and Foundations under static and Dynamic loading. *Research Report, Geotechnical Division, NTUA*. 2002;

Brennan AJ, Madabhushi SPG, Houghton NE. Comparing laminar and equivalent shear beam (ESB) containers for dynamic centrifuge modelling. *Proc. 6th Int. Conf. on Physical Modelling in Geotechnics*. 2006, 171–176;

Bui M. Influence of some particle characteristics on the small strain response of granular materials. PhD Thesis, *University of Southampton*. 2009;

Cai Y. An experimental study of non-coaxial soil behavior using hollow cylinder testing. PhD Thesis, *University of Nottingham*. 2010;

Cairo R, Conte E, Cosimo VA, Dente G. Analisi dell'interazione cinematica palo-terreno. *Proc of XIII ANIDIS, L'Ingegneria Sismica in Italia, Bologna*. 2009, paper 179 (in Italian);

Cairo R, Conte E, Dente G. Analysis of pile groups under vertical harmonic vibration. *Computers and Geotechnics*. 2005, 32(7), 545-554;

Cairo R, Dente G. Un metodo per l'analisi dell'interazione cinematica palo-terreno nei depositi orizzontalmente stratificati. *Proc. of XII ANIDIS, L'Ingegneria Sismica* in Italia, Pisa. 2007, paper 378 (in Italian);

Cavallaro A, Maugeri M, Mazzarella R. Static and dynamic properties of Leighton Buzzard sand from laboratory tests. *Proc of 4th International Conference on Recent Advances in Geotechnical Earthquake Engineering and Soil Dynamics, San Diego*. 2001, paper 1.13;

Chau KT, Shen CY and Guo X. Non linear seismic soil-pile-structure interactions: shaking table tests and FEM analyses. *Soil Dynamics and Earthquake Engineering*. 2009, 29 , 300-310;

Chidichimo A, Cairo R, Dente G, Taylor C, Mylonakis G. 1-g experimental investigation of bi-layer soil response and kinematic pile bending, *Soil Dynamics and Earthquake Engineering*. 2014, 67, 219 – 232;

Chidichimo A. Experimental and analytical investigation on soil-pile-structure interaction PhD Thesis, *Università "Mediterranea" Reggio Calabria*. 2014;

Chopra AK, Gutierrez JA. Earthquake response analysis of multistory buildings including foundation interaction. *Earthquake Engineering Structure Dynamics*. 1974, 3, 65–77;

Ciampoli M and Pinto PE. Effects of soils-structure interaction on inelastic seismic response of bridge piers. Journal of Structural Engineering, ASCE. 1995, 121(5), 806-814.

Clough RW, Penzien J. Dynamics of Structures. New York: McGraw-Hill. 2nd Edition. 1993;

Conti R. Modellazione fisica e numerica del comportamento di opera di sostegno flessibili in condizioni sismiche. PhD Thesis, *Universita' degli Studi di Roma "Tor Vergata", Roma*. 2010 (in Italian);

Crewe AJ, Lings,ML, Taylor CA, Yeung AK and Andrighetto R. Development of a large flexible shear stack for testing dry sand and simple direct foundations on a shaking table. *European seismic design practice, Elnashai (ed) , Balkema, Rotterdam*. 1995;

CSI Analysis Reference Manual for SAP2000, ETABS and SAFE. *Computers and Structures, Inc., Berkeley, CA, USA*. 2013;

de Sanctis L, Maiorano RMS, Aversa S. A method for assessing kinematic bending moments at the pile head. *Earthquake Engineering and Structural Dynamics*. 2010, 39:375–397;

Dezi F, Carbonari S, Leoni G. Kinematic bending moments in pile foundations. *Soil Dynamics and Earthquake Engineering*. 2009, 30(3):119–132;

Di Laora R, Mandolini A, Mylonakis G. Insight on kinematic bending of flexible piles in layered soil. *Soil Dynamics and Earthquake Engineering*. 2012, 43, 309–322;

Di Laora R, Mylonakis G, Mandolini A. Pile-head kinematic bending in layered soil. *Earthquake Engineering and Structural Dynamics*. 2013, 42, 319–337

Dietz M, Muir Wood D. Shaking table evaluation of dynamic soil properties. *Proc. of the 4th International Conference on Earthquake Geotechnical Engineering, Thessalonikki, Greece*. 2007;

Dobry R, O'Rourke MJ. Discussion on 'Seismic response of end-bearing piles' by Flores-Berrones R., Whitman R.V. *J. Geotech. Engng Div., ASCE*. 1983, 109, pp. 778-781;

Dobry R, Oweis I, Urzua A. Simplified procedures for estimating the fundamental period of a soil profile. *Bull Seism Soc Am*. 1976; 66(4): 1293-1321;

Dobry R, Whitman R and Roesset JM. Soil properties and the one dimensional theory of earthquake amplification. , *M.I.T. Research Report*. 1971, R71-18;

Donovan K, Pariseau WG and Cepak M. Finite element approach to cable bolting in steeply dipping VCR slopes. *Geomechanics Applications in Underground Hardrock Mining (ed.W. G. Pariseau) AIME: New York*. 1984, 65–90;

Durante MG, Di Sarno L, Sica S, Mylonakis G, Taylor C, Simonelli AL. Seismic Pile-Soil Interaction: Experimental results vs. numerical simulations. *Proc. of the 4th Intern. Conf. on Computational Methods in Structural Dynamics and Earthquake Engineering. M. Papadrakakis, V. Papadopoulos, V. Plevris (eds.), Kos Island, Greece*. 2013;

Durante MG, Di Sarno L, Sica S, Mylonakis G, Taylor CA, Simonelli AL. Experimental measurements of geotechnical system in 1-g tests. *Proc. of 20th IMEKO TC4 Symposium on Measurements of Electrical Quantities: Research on Electrical and Electronic Measurement for the Economic Upturn, Benevento – Special Session: Advanced Measurements in Geotechnics*. 2014;

Durante MG, Di Sarno L, Sica S, Simonelli AL, Chidichimo A, Cairo R, Dente G. Sperimentazione su pali mediante tavola vibrante. *Incontro Annuale dei Ricercatori di Geotecnica – IARG, Padova*. 2012 (in Italian);

Durante MG, Di Sarno L, Sica S, Simonelli AL. Interazione terreno-palo-struttura in condizioni dinamiche: evidenze sperimentali. *Incontro Annuale dei Ricercatori di Geotecnica – IARG, Perugia*. 2013 (in Italian);

Durante MG, Di Sarno L, Sica S, Simonelli AL. Interazione terreno-palo-struttura: analisi numeriche di prove sperimentali. *Incontro Annuale dei Ricercatori di Geotecnica – IARG, Chieti*. 2014 (in Italian);

Durante MG, Di Sarno L, Taylor CA, Mylonakis G, Simonelli AL. Soil-pile-structure-interaction: experimental results and numerical simulations. *Proc. of COMPDYN 2015, 5th ECCOMAS Thematic Conference on Computational Methods in Structural Dynamics and Earthquake Engineering. Crete Island, Greece*. 2015;

Durante MG, Karamitros D, Di Sarno L, Sica S, Taylor CA, Mylonakis G, Simonelli AL. Characterisation of shear wave velocity profiles of non-uniform bi-layer soil deposits: analytical evaluation and experimental validation. *Soil Dynamics and Earthquake Engineering*. 2015;

Elgamal A, Lu J, Yang Z. Liquefaction-induced settlement of shallow foundations and remediation: 3D numerical simulation. *Journal of Earthquake Engineering (Spec Iss)*. 2005, 9, pp. 17-45;

Fan K, Gazetas G, Kaynia A, Kausel E, Ahmad S. Kinematic seismic response of single pile and pile groups. *Journ Geotech Engng, Div, ASCE*. 1991, 117(12), 1860-1879;

Flores-Berrones R, Whitman RV. Seismic response of end-bearing piles. *Journ Geotech Engng, Div, ASCE*. 1982, 108(4), 554-569;

Foinquinos R, Roësset JM. Elastic layered half-space subjected to dynamic surface loads. *Wave motion in earthquake engineering, E. Kausel & G. Manolis (eds), Southampton: WIT Press*. 2000, 141-191;

Gazetas G and Mylonakis G. Seismic soil-structure interaction: new evidence and emerging issues. *Geotechnical Earthquake Engineering and Soil Dynamics III, ASCE, Dakoulas, P., Yegian, M.K. and Holtz, R.D. Editors*. 1998, Vol. II, 1119-1174.

Gazetas G. Vibrational characteristics of soil deposits with variable wave velocity. *International J Num Anal Meth Geomech*. 1982; 6:1-20;

Georgiadis M, Anagnostopoulos C, Saflekou S. Centrifugal Testing of laterally loaded piles in sand. *Canadian Geotechnical Journal*. 1992, 29, 208-216;

Ghalibafian H. Evaluation of the effects of nonlinear soil-structure interaction on the inelastic seismic response of pile-supported bridge piers. PhD Thesis, *University of British Columbia, Vancouver, BC*. 2006;

Ghosh B, Madabhushi SPG. A numerical investigation into effects of single and multiple frequency earthquake input motion. *Soil Dyn. Earthquake Eng*. 2003, 23(8), 691–704;

Hokmabadin AS, Fatahi B, Samali B. Seismic response of mid-rise buildings on shallow and end-bearing pile foundations in soft soil. *Soils and Foundations*. 2014, 54(3), 345–363;

Hushmand B, Scott RF and Crouse CB. Centrifuge liquefaction tests in a laminar box. *Géotechnique*. 1988, 38(2), 253–262;

Itasca. FLAC – Fast Lagrangian Analysis of Continua – User's Guide, Version 5.0. *Itasca Consulting Group, Inc., Minneapolis, USA*. 2005;

Jennings PC and Bielak J. Dynamics of building-soil interaction. *Bull Seism Soc Am*. 1973, 63(1), 9-48;

Karamitros D. Development of a numerical algorithm for the dynamic elastoplastic analysis of geotechnical structures in two (2) and three (3) dimensions. PhD Thesis, *National Technical University of Athens, Athens*. 2010;

Kausel E. Early history of soil–structure interaction. *Soil Dynamics and Earthquake Engineering, Special Issue in honour of Prof. Anestis Veletsos*. 2010, 30(9), 822-832;

Kavvadas M, Gazetas G. Kinematic seismic response and bending of free-head piles in layered soil. *Géotechnique*. 1993, 43(2), 207-222;

Kaynia AM, Kausel E. Dynamic stiffness and seismic response of pile groups. *Rep. R82-03, MIT, Cambridge*. 1982;

Knappett JA. Piled foundations in liquefiable soils: accounting for axial loads. PhD Thesis, *Cambridge University, England*. 2006;

Kramer SL. Geotechnical Earthquake Engineering. *Prentice Hill, Upper Saddle River, NJ, USA*. 1996;

Kuhlemeyer RL, Lysmer J. Finite Element Method accuracy for wave propagation problems. *J Soil Mech Found,Div, ASCE*. 1973, 99(SM5): 421-427;

Kutter BL. Recent Advances in Centrifuge Modeling of Seismic Shaking. *Proc. 3rd Int. Conf. on Recent Advances in Geotechnical Earthquake Engrg. and Soil Dyn*. 1995, 2, 927–942;

Kwon SY, Kim MM, Kim SH, Choi JI. 3D Dynamic Numerical Modeling for Soil-Pile-Structure Interaction in Centrifuge Tests. *Proc of the 18th International Conference on Soil Mechanics and Geotechnical Engineering, Paris*. 2013;

Lings ML, Dietz MS. An improved direct shear apparatus for sand. *Géotechnique*. 2004, 54(4), 245–256;

Liu H and Song E. Seismic response of large underground structures in liquefiable soils subjected to horizontal and vertical earthquake excitations. *Computers and Geotechnics*. 2005, 32(4), 223 – 244;

Luco E. Linear soil-structure interaction: a review. *In 'Earthquake Ground Motions and Effects on Structures', ASME*. 1982, AMD(53), 41-57;

Luco JE, Contesse L. Dynamic structure–soil–structure interaction. *Bull Seism Soc Am*. 1973, 63(4), 1289–303;

Luco JE. Ground motion characterization required for soil-structure interaction analysis. *In Strong Ground Motion Simulation and Earthquake Engineering Applications. A Technical Assessment, Scholl, R.E. and King, J.L. Editors, Earthquake Engineering Research Institute, Rep.85-02*. 1985;

Lysmer J et al. Efficient finite element analysis of seismic soil structure interaction, *inReport:EERC-75-34.Earthquake Engineering Research Center, University of California, Berkeley, CA*, 1975;

Madera GA. Fundamental period and amplification of peak acceleration in layered systems. *Rep. R70-37, MIT, Cambridge*. 1970;

Maiorano RMS, de Sanctis L, Aversa S, Mandolini A. Kinematic response analysis of piled foundations under seismic excitation. *Canadian Geotechnical Journal*. 2009, 46, 571-584;

Mamoon SM, Banerjee PK. Response of piles and pile groups to travelling SH-waves. *Earthquake Engineering and Structural Dynamics*. 1990, 19(4), 597-610;

Margason E, Holloway DM. Pile design during earthquakes. *Proc. 6th Wld Conf. Earthq. Engng, New Delhi*. 1977, 237-243

Meymand PJ. Shaking table scale model tests of nonlinear soil-pile-superstructure interaction in soft clay. PhD Thesis, *University of California, Berkeley*. 1998;

Mineiro AJC. Simplified Procedure for Evaluating Earthquake Loading on Piles. *De Mello Volume, Lisbon*. 1990;

Mizuno H, Iiba M and Kitagawa Y. Shaking table testing of seismic building-pile-two layered–soil interaction. *Proc. of 8th World Conference on Earthquake Engineering, San Francisco*. 1984, 3, 649-656;

Mizuno H. Effects of structure–soil–structure interaction during various excitations. *Proc. of the seventh world conference on earthquake engineering. Istanbul,Turkey*. 1980, 149–156;

Moccia F. Seismic soil pile interaction: experimental evidence. PhD Thesis, *Universita' degli Studi di Napoli Federico II, Napoli*. 2009;

Muir Wood D, Crewe A and Taylor CA. Shaking Table Testing of Geotechnical Models. *UPMG- International Journal of Physical Modelling in Geotechnics.* 2002, 2, 01-13;

Muir Wood D. Geotechnical Modelling. *Spon Press, Oxfordshire*. 2004;

Mylonakis G and Gazetas G. Seismic soil-structure interaction: beneficial or detrimental? *Journal of Earthquake Engineering*. 2000, 4(3), 277-301.

Mylonakis G, Nikolaou A, Gazetas G. Soil-pile-bridge seismic interaction: kinematic and inertial effects. Part I: soft soil. *Earthquake engineering and structural dynamics*. 1997, 26, 337-359;

Mylonakis G. Contributions to static and seismic analysis of piles and pile-supported bridge piers. PhD Thesis. *State University of New York at Buffalo*. 1995;

Mylonakis G. Simplified model for seismic pile bending at soil layer interfaces. *Soils and Foundations*. 2001, 41(4), 47-58;

Mylonakis GE, Rovithis E, Parashakis H. 1D harmonic response of layered inhomogeneous soil: Exact and approximate analytical solutions. *Computational Methods in Earthquake Engineering; Computational methods in Applied Sciences*. 2013, 30, 1-32;

Nikolaou AS, Gazetas G. Seismic design procedure for kinematically loaded piles. *Proc. 14th Int. Conf. Soil Mech. Found. Engng, Hamburg, Special volume, ISSMFE TC4 Earthquake geotechnical engineering*. 1997, 253-260

Nikolaou S, Mylonakis G, Gazetas G, Tazoh T. Kinematic pile bending during earthquakes: analysis and field measurements. *Géotechnique*. 2001, 51(5), 425-440;

NIST. Soil-structure interaction for building structures. *National Institute of Standards and Technology, U.S. Department of Commerce, Washington D.C. Project Technical Committee: Stewart, JP (Chair), CB Crouse, T Hutchinson, B Lizundia, F Naeim, and F Ostadan*. 2012, Report No. NIST GCR 12-917-21;

Pitilakis D, Dietz M, Wood DM, Clouteau D, Modaressi A. Numerical simulation of dynamic soil–structure interaction in shaking table testing. *Soil Dynamics and Earthquake Engineering*. 2008, 28, 453–467;

Popescu R, Prevost JH, Deodatis G, Chakrabortty P. Dynamics of nonlinear porous media with applications to soil liquefaction. *Soil Dynamics and Earthquake Engineering*. 2006, 4 (1), 9-17;

Ramberg W, Osgood WR. Description of stress-strain curve by three parameters. *Technical Note 902, National Advisory Committee for Aeronautics, Washington D. C.* 1943;

Randolph MF. The response of flexible piles to lateral loading, *Géotechnique*. 1981, 31, 247-259;

Reiter L. Earthquake Hazard Analysis: Issues and Insights. *New York: Colombia University Press*. 1991. 254 pp;

RELUIS (Rete dei Laboratori Universitari di Ingegneria Sismica). Study funded by DPC (Italy), University of Bristol (United Kingdom), University of Sannio (Italy),) and University of Patras (Greece), 2008.

Roesset JM. A review of soil-structure interaction. *In 'Soil-structure interaction: The status of current analysis methods and research', Edited by Johnson, J.J., US Nuclear Regulatory Commission and Lawrence Livermore Laboratory, Report No.NUREG/CR-1780 and UCRL-53011*. 1980;

Rovithis E, Parashakis Ch, Mylonakis G. 1D harmonic response of layered inhomogeneous soil: analytical investigation. *Soil Dynamics and Earthquake Engineering*.2011, 31(7), 879 – 890;

Samuelssonn A, Zienkiewicz OC. History of the stiffness method. *Int. J. Numer. Meth. Engng*. 2006, 67(2), 149-157;

Sarma SK. Analytical solution to the seismic response of visco-elastic soil layers. *Géotechnique*. 1994, 44 (2), 265-275.

Scasserra G, Lanzo G, Stewart JP, D'Elia B. SISMA (Site of Italian Strong-Motion Accelerograms): a web-database of ground motion recordings for engineering applications. *Seismic Engng. Conf. commemorating the 1908 Messina and Reggio Calabria Earthquake, Reggio Calabria, AIP, Melville, N.Y.* 2008, 2, 1649-1656; http://sisma.dsg.uniroma1.it;

Schreyer H. One-dimensional elastic waves in inhomogeneous media. *J Eng Mech Div ASCE*. 1977, 103(5), 979-990;

Seed HB, Idriss IM. Soil moduli and damping factors for dynamic response analyses. *Earthquake engineering research center*. 1970, report no. EERC 70-10;

Seed HB, Idriss IM. The influence of ground conditions on ground motions during earthquakes. *J Soil Mech Found*. 1969, 94, 93-137;

Seed HB, Lysmer J, and Hwang R. Soil–structure interaction analysis for seismic response. *Proc. ASCE*. 1975, 101(5), 439–457;

Sica S, Mylonakis G, Simonelli AL. Kinematic bending of piles: analysis vs. code provisions. *Proc. of the 4th International Conference on Earthquake Geotechnical Engineering, Thessaloniki, Greece*. 2007;

Sica S, Mylonakis G, Simonelli AL. Transient kinematic pile bending in two-layer soil. *Soil Dynamics and Earthquake Engineering*. 2011, 31, 891-905;

Simonelli AL, Di Sarno L, Durante MG, Sica S, Bhattacharya S, Dietz M, Dihoru L, Taylor CA, Cairo R, Chidichimo A, Dente G, Modaressi A, TodoBom LA, Kaynia AM, Anoyatis G, Mylonakis G. Chapter 27: Experimental Assessment of Seismic Pile-Soil Interaction. *Seismic Evaluation and Rehabilitation of Structures, Geotechnical, Geological and Earthquake Engineering*. 2014, 26, 455-475;

Simonelli AL, Di Sarno L, Durante MG, Sica S, Bhattacharya S, Dietz M, Dihoru L, Taylor CA, Cairo R, Chidichimo A, Dente G, Anoyatis G, Mylonakis G, Modaressi A, TodoBom LA and Kaynia AM. Performance of soil-pile-structure systems under seismic waves. *Proc. of the II Int. Conf. on Performance-Based Design in Earthquake Geotechnical Engineering, Taormina.* 2012;

Simonelli AL, Di Sarno L, Durante MG, Sica S, Bhattacharya S, Dietz M, Dihoru L, Taylor CA, Cairo R, Chidichimo A, Dente G, Anoyatis G, Mylonakis G, Modaressi A, TodoBom LA and Kaynia AM. Experimental investigation of soil-pile-structure seismic interaction. *Proc. of the 15th World Conference on Earthquake Engineering, Lisbon*. 2012

Simonelli AL, Di Sarno L, Durante MG, Sica S, Bhattacharya S, Dietz M, Dihoru L, Taylor CA, Cairo R, Chidichimo A, Dente G, Modaressi A, TodoBom LA, Kaynia AM, Anoyatis G, Mylonakis G. Chapter 27: Experimental Assessment of Seismic Pile-Soil Interaction. *Seismic Evaluation and Rehabilitation of Structures, Springer*. 2014;

Solari G, Stura D, Vardanega C. On the accuracy of numerical models in 3-D soil–structure interaction. *Proc. of the seventh world conference on earthquake engineering. Istanbul, Turkey*. 1980, 237–244;

Stewart JP and Fenves GL. System identification for evaluating soil-structure interaction effects in buildings from strong motion recordings. *Earthquake Engineering and Structural Dynamics*. 1998, 27 (8), 869-885;

Stewart JP, Fenves GL and Seed RB. Seismic soil-structure interaction in buildings. I: Analytical methods. *J Geotech & Geoenv Engrg, ASCE*. 1999-a, 125(1), 26-37;

Stewart JP, Seed RB and Fenves GL. Seismic soil-structure interaction in buildings. II: Empirical findings. *J Geotech & Geoenv Engrg, ASCE*. 1999-b, 125(1), 38-48;

Stroud M A. The behaviour of sand at low stress levels in the simple shear apparatus. PhD Thesis, *University of Cambridge, UK*. 1971;

Tan FSC. Centrifuge and theoretical modelling of conical footings on sand. PhD Thesis, *University of Cambridge, UK*. 1990;

Terzaghi KV. Evaluation of Coefficient of Subgrade Reaction. *Géotechnique*. 1955, 5(4): 297-326;

Toki K, Cherry S. Inference of subsurface accelerations and strain from accelerograms recorded at ground surface. *Proc. of the 4th European Symposium on Earthquake Engineering. London*. 1972;

Tokimatsu K, Suzuki H. Seismic soil-pile-structure interaction based on large shaking table tests.. *Performance-based design in earthquake geotechnical engineering, T. Kokusho, Y. Tsukamoto, and M. Yoshimine, eds., Taylor & Francis, Boca Raton, FL*. 2009;

Towhata I. Seismic wave propagation in elastic soil with continuous variation of shear modulus in the vertical direction. *Soils Found*. 1996, 36(1), 61-72;

Ueng TS, Wang MH, Chen MH, Chen CH, and Peng LH. A large biaxial shear box for shaking table tests on saturated sand. *Geotechnical Testing Journal*. 2006, 29(1), 1-8;

Veletsos AS and Meek JW. Dynamic Behavior of building-foundation systems. *Earthquake Engineering and Structural Dynamics*. 1974, 3(2), 121-138;

Visone C, Santucci de Magistris F. Mechanical behaviour of the Leighton Buzzard Sand 100/170 under monotonic, cyclic and dynamic loading conditions. *Proceeding of the XIII conference: L'ingegneria Sismica in Italia, ANIDIS, Bologna, Italy*. 2009;

Vrettos, C. Dynamic response of soil deposits to vertical SH waves for different rigidity depth-gradients. *Soil Dynamics and Earthquake Engineering*. 2013, 47, 41-50;

Vucetic M, Dobry R. Effect of soil plasticity on cyclic response. *Journal of Geotechnical Engineering, ASCE*. 1991, 117 (1), 89-107;

Wei X, Fan L and Wu X. Shaking table tests of seismic pile-soil-pier-structure interaction. *Proc. of 4th International Conference on Recent Advances in Geotechnical Earthquake Engineering and Soil Dynamics*. 2001, Paper 9.18;

Wolf JP, von Arx GA, de Barros FCP, Kakubo M. Seismic analysis of the pile foundation of the reactor building of the NPP Angra 2. *Nucl. Eng. Des*. 1981, 65, 329-341;

Wolf JP. Dynamic Soil–Structure Interaction. *NewYork: Prentice hall*. 1985;

Zeng X, Schofield AN. Design and performance of an equivalent-shear-beam container for earthquake centrifuge modelling. *Géotechnique*. 1996, 46(1), 83–102.